Volume 24, Issue 1 2014

ATOMIZATION AND SPRAYS

Journal of the International Institutes for Liquid Atomization and Spray Systems

begell
New York • Connecticut

AIMS AND SCOPE

The application and utilization of sprays is not new, and in modern society, it is extensive enough that almost every industry and household uses some form of sprays. What is new is an increasing scientific interest in atomization - the need to understand the physical structure of liquids under conditions of higher shear rates and interaction with gaseous flow. This need is being met with the publication of Atomization and Sprays, an authoritative, international journal presenting high quality research, applications, and review papers

Atomization and Sprays (ISSN 1044-5110) is published 12 times per year and owned by Begell House, Inc., 50 Cross Highway, Redding, Connecticut 06896. US subscription rate for 2013 is $1652.00. Add $10.00 per issue for foreign airmail shipping and handling fees for all orders shipped outside the United States or Canada. All subscriptions are payable in advance. Subscriptions are entered on an annual basis, i.e., January to December. For immediate service, charge card sales and subscriptions for online access, call (203) 938-1300 Monday through Friday 9AM-5 PM EST. Fax orders to (203-938-1304. Send written orders to Subscriptions Department, Begell House, Inc., 50 Cross Highway, Redding, Connecticut 06896. You can also visit our website at www.begellhouse.com or http://dl.begellhouse.com/.

Covered in: *Science Citation Index (SCI), Current Contents®/Engineering, Computing & Technology, Aerospace Database.* Abstracted in: *Chemical Abstracts Service*. Indexed in: *SciSearch* and *Research Alert.*

Printed January 18, 2014

ATOMIZATION AND SPRAYS

Journal of the International Institutes for Liquid Atomization and Spray Systems

ATOMIZATION AND SPRAYS

VOLUME 24, NUMBER 1 **2014**

CONTENTS

Atomization and Sprays, 24 (1): 1–22 (2014)

MACROSCOPIC SPRAY CHARACTERISTICS OF A POROUS INJECTOR

Dohun Kim,[1] Inchul Lee,[1] & Jaye Koo[2,*]

[1] *Department of Aerospace and Mechanical Engineering, Graduate School of Korea Aerospace University, Korea*

[2] *School of Aerospace and Mechanical Engineering, Korea Aerospace University, Goyang 412-491, Korea*

[*] Address all correspondence to Jaye Koo E-mail: jykoo@kau.ac.kr

Original Manuscript Submitted: 10/9/2012; Final Draft Received: 10/25/2013

The concept of coaxial porous injector design for gas-liquid mixing involves improved momentum transfer between the gas and liquid jets by changing the gas injecting direction of a conventional liquid-centered shear coaxial injector from parallel to perpendicular using porous material. Cold-flow tests of the coaxial porous injector and the shear coaxial injector in two-dimensional configurations were carried out to compare the macroscopic characteristics of sprays from each injector and to understand the effects of spraying conditions on the breakup length and the spray angle. The spray patterns were visualized using the shadowgraphy technique. The shadowgraph images recorded in high speed were post-processed to detect the breakup length and the spray angle. The post-processing code filters the dynamic pixels, and leaves the stationary pixels, which corresponds to the liquid core and the background. The most significant differences between the porous injector and the shear injector in the two-dimensional configurations were the spray angle and the uniformity of the disintegrated liquid jet. The liquid column from the shear injector was not split off entirely, and only the portion at the interface between the gas and liquid jet was atomized by the shear force. On the other hand, the liquid jet from the porous injector dispersed more widely, and was disintegrated into droplets more completely in most experimental cases of similar axial momentum flux ratio conditions at the injector tip, and it was thought that an optimal porous element length for the best mixing performance exists at certain injection conditions.

KEY WORDS: *porous injector, two-dimensional injector, breakup length, spray boundary detection, momentum flux ratio*

1. INTRODUCTION

Coaxial injectors have long seen widespread use for industrial purposes. For instance, most liquid rocket engines employ a coaxial swirl injector. Since a liquid rocket engine generates a large amount of thrust in a short amount of time and the flow rate of the propellant is very large, atomization and mixing performance is very important (Huzel and

Huang, 1971). The design of a coaxial swirl injector overcomes certain disadvantages inherent in a conventional impinging or a coaxial shear injector. These disadvantages include combustion instability and an imbalance in terms of the mixture ratio at the center of the spray (Rahman et al., 1995; Rahman, 1997). However, with respect to the coaxial swirl injector, shortcomings still exist with respect to the difficulty of design, the high manufacturing costs, the strict tolerance requirements, and the heavy weight. This paper introduces the novel concept of a coaxial porous injector. The porous material has many advantages in terms of thermodynamics and fluid mechanics, including uniform flow distribution, filtration, flow isolation, and transpiration cooling, so it has been widely used in surface burners, industrial filters, flame arresters, sound dampers, and flow straighteners.

Polyaev and his co-workers (2000) carried out droplet measurements for spray from a gas-liquid injector, which mixed the two-phase propellant in the porous material, and they suggested a semiempirical equation, which denoted the relationship between the spray conditions and the maximum droplet diameter. Researchers in Germany (Lux et al., 2008a,b; Deeken et al., 2010) investigated the combustion characteristics of the shower-head-type porous injector. Bazarov (1993) suggested many types of novel porous atomizer concepts, and these atomizers have shown an extremely fine breakup of liquid droplets.

In this study, a coaxial porous injector was conceived to improve the atomizing and mixing performance, and to reduce the manufacturing cost and tolerance limit by applying the porous material to the two-phase flow injector. The schematic of the coaxial porous injector suggested in this study is shown in Fig. 1. The outline of the design is similar to that of the conventional liquid-centered coaxial shear injector, except that a porous cylinder, which discharges gas, encloses the center liquid jet. The key feature of

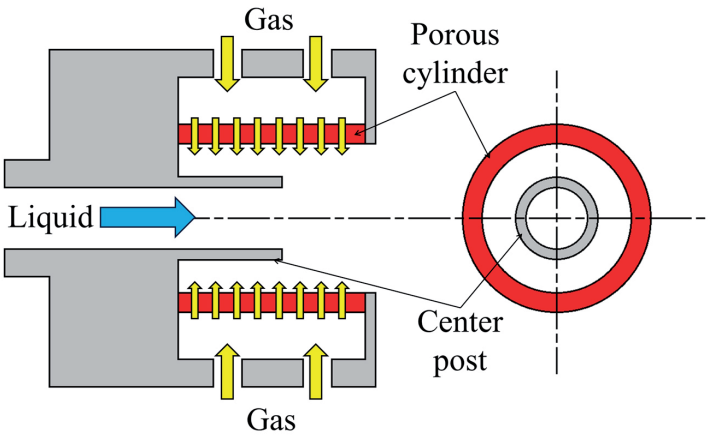

FIG. 1: Schematic of a coaxial porous injector

a coaxial porous injector is the radial injection of the gas jet from the internal surface of the porous cylinder. The radial gas jet develops in the axial direction at the recessed region, where the gas and liquid jet make contact with each other as shown in Fig. 2. During this process, the gas jet transfers the radial momentum to the center liquid jet, and this helps the liquid jet to disintegrate more effectively compared to the coaxial shear injector, which atomizes the liquid jet only with the axially injected gas. The effervescent injector has a geometry very similar to the coaxial porous injector, except that the liquid is injected through the porous cylinder, and the gas is discharged from the center post. The studies about droplet size prediction and the effect of injection condition on atomization were performed by Qian and his co-workers (2009).

To investigate the effect of the radial momentum gas jet on the spray characteristics, a comparative study between the proposed coaxial porous injector and a coaxial shear injector was carried out. Both injectors in the twodimensional (2D) configurations were manufactured to observe the interaction of the gas and liquid jet at the recessed region and the macroscopic characteristics of sprays at the near-injector field excluding the cumulative effect of the shadowgraph image taken from the side of the three-dimensional (3D) injector spray. For clarity, the simple expressions "shear injector" and "porous injector" were used instead of the quasi 2D configuration of "coaxial porous injector" and "coaxial shear injector". Also, the terms "radial gas jet", "annular gap" and "diameter" were replaced by "lateral gas jet", "gas injection gap" and "width" respectively.

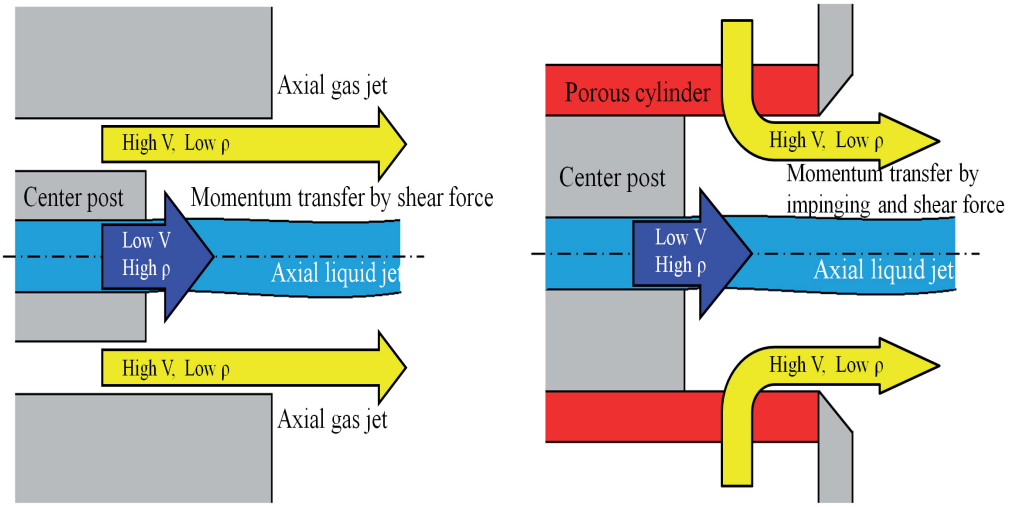

(a) (b)

FIG. 2: Comparison of the gas flow regimes between (a) a coaxial shear injector and (b) a coaxial porous injector

2. EXPERIMENTAL SETUP AND METHODS

2.1 Quasi-2D Injector

Figure 2 shows the side and front view of the injectors used in the cold-flow experiments. Although the sprays from the quasi-2D injectors are spread in a three-dimensional space, the interaction of the liquid and gas jet at the near-injector region could be visualized more clearly than with the 3D injector. The shear injector and the porous injector could be transformed by changing some components. The upper side of Fig. 3(a) describes the shear injector, and the lower side shows the configuration of the porous injector. The transverse width of the quasi-2D injector is 9 mm. The porous element was manufactured precisely to simulate the wall injection of the gas-phase propellant, and the dimensions are represented in Fig. 4. A total of 189 holes with a diameter of 0.5 mm, a longitudinal pitch of 0.75 mm, and a transversal pitch of 0.65 mm were drilled, and the blockage ratio is about 40.3%. The side panel of the quasi-2D injector was made with high purity acrylic plates. The numerical control-engineered PTFE gasket was inserted into the contacts of the acrylic side windows to prevent leakage and the abnormal mixing of propellant on the inside of the injector.

Four types of quasi-2D injectors were used in the cold-flow test, and the representative dimensions are described in Table 1. There are two experimental factors: (i) The type of quasi-2D injector (a shear injector or a porous injector), and (ii) the length of the porous element, L_{pr}. The length of the porous element is defined as the distance between the liquid center post tip and the injector tip and is equal to the recess depth in the shear injector.

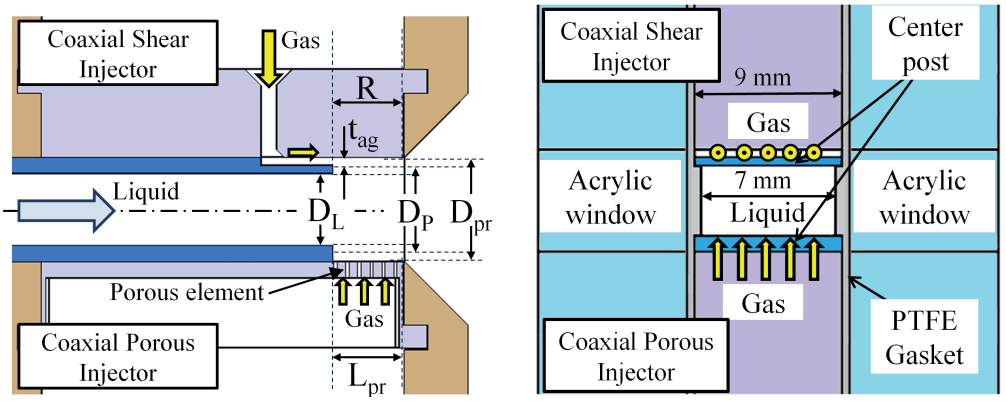

FIG. 3: Schematics of the shear injector and the porous injector: (a) side view, (b) front view

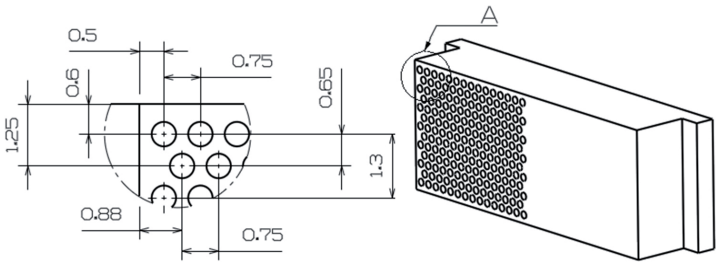

FIG. 4: Dimensions with a detailed view of the porous element, units: mm

TABLE 1: Geometrical dimensions of quasi-2D injectors, units: mm

Shear injector				
Injector no.	Inner width of center post, D_L	Outer width of center post, D_p	Gas injection gap, t_G	Recess depth, R
INJ-1-1	4.5	6.5	1.0	4.5
Porous injector				
Injector no.	Inner width of center post, D_L	Width of porous element, D_{pr}	Length of porous element, L_{pr}	Recess depth, R
INJ-2-1	4.5	8.5	1.5	1.5
INJ-2-2	4.5	8.5	3.0	3.0
INJ-2-3	4.5	8.5	4.5	4.5

2.2 Cold-Flow Test Facility

A cold-flow test facility was constructed to supply the high pressure inert propellants: water for liquid and gaseous nitrogen for gas. The piping diagram of the facility is shown in Fig. 5. The flow rates of the water and gaseous nitrogen were measured with a Macnaught M series positive displacement flowmeter and a differential pressure orifice flowmeter, respectively. The flow rates of the water and air were controlled by the regulators attached to the high pressure air tank outlet. Pressure transducers were set to measure pressure drops at the gas and liquid injectors. All of the physical properties were measured by a LabVIEW PCI-6221 data acquisition device with the sampling speed of 10 kHz. The bias errors of physical measurements, such as pressure transducer and thermocouple, were based on the manufacturer's specification sheets, and the standard errors were computed from the statistics of 10,000 samples at the steady state. The combined standard uncertainties of measurements were calculated by root sum square of the bias error and the standard error. The coverage factor was 2 for a 95% confidence level. The uncertainties of flow conditions, which were calculated from diverse parameters, were estimated with considering the propagation of uncertainty (Abernethy et al., 1985; Kline, 1985).

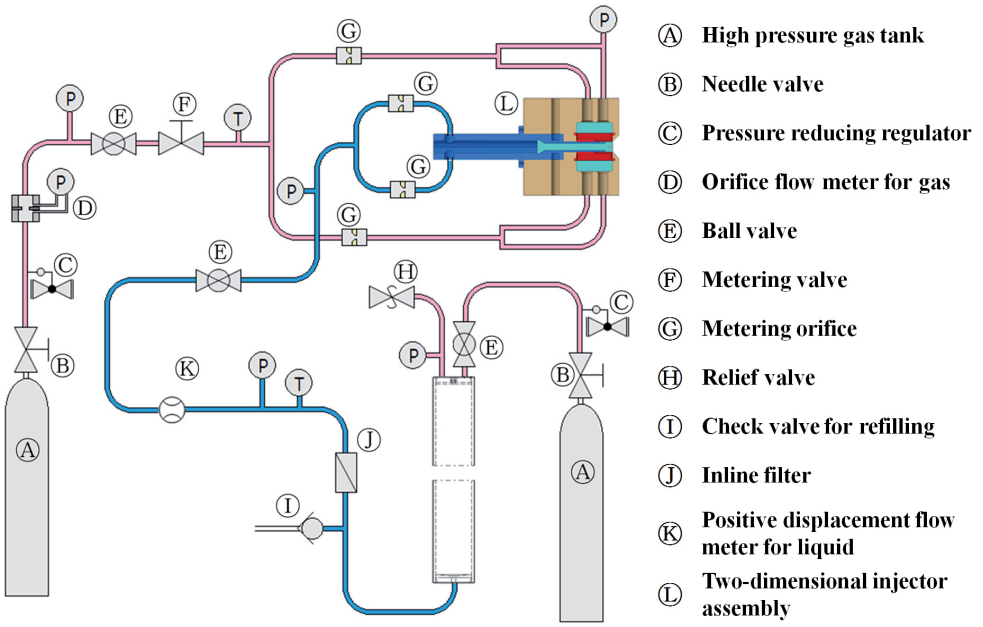

FIG. 5: Schematic of the cold-flow test system

The spray images were taken using backlit photography. Temporary spray jet images were captured by a SVSi GIGAVIEW high frame rate CCD camera, which acquired 1036 frames per second with an image resolution of 640×480 pixels. Given this fast recording speed and exposure time, a high-intensity light source at the visualized region was critical to ensure final image quality. An SST-90 LED was used as a light source, and it provided exposure times down to 2 μs.

2.3 Breakup Length and Spray Boundary Detecting Technique

The spray images, acquired at 1036 samples per second, were post-processed to get the averaged image and to estimate the breakup length and the spray angle with an in-house Matlab code. In the shadowgraph images, the liquid spray is presented in black color (shadow), and the background is in white (backlight). When part of the liquid spray passes the background, the pixel color frequently alternates between white and black. The pixels, which consist of the dark liquid core and the background, have solid color and appear stationary (black and white respectively) during the injection. Accordingly, the liquid core and the spraying path, which represents the spray angle, can be detected by dividing the pixels into the stationary pixels (liquid core and background) and the dynamic pixels (path of disintegrated spray) according to the degree of pixel changing rate.

The raw images are stored in an 8-bit grayscale format, and each pixel is a shade of gray, from 0 (black) to 255 (white). The pixelated digital images can be manipulated as a matrix, and each pixel represents the element of a matrix. Figure 6 shows the image processing procedure using Matlab to detect the breakup length and the spray angle. To classify the pixel as dynamic or stationary, a criterion named the "deviation factor" is established for this study. The averaged image can be obtained by calculating the arithmetic mean value of each pixel. The liquid core and the background are almost stationary during the discharging of spray, and the other pixels, which vary from white (background light) to black (shadow of ligament and droplet), can be considered as a region where the spray passes. The criterion to distinguish the pixels as either stationary or dynamic was determined by the deviation factor. As shown in Fig. 6, the deviation factor of each pixel was defined by the percentage of the excess of inverse normal cumulative distribution function. Assuming that the grayscale data of a pixel have a normal distribution, if the points of $\pm 1.645\sigma$ are inside the range of $\pm\beta\%$ from the average, the pixel is classified as a stationary pixel; otherwise it is classified as a dynamic pixel as shown in Fig. 7. The threshold of deviation factor, β, was determined by comparing the image process results with a number of the still images, because the true value of the breakup length was unknown, and was estimated by a statistical method.

The uncertainties of the image processing were determined by changing the deviation factor threshold from 4% to 14% which shows acceptable results. The breakup length of INJ 2-3 spray, for example, was varied from 23.8 mm to 25.3 mm as plotted in Fig. 8. As the threshold increased, the breakup length was changed step by step. The threshold of deviation factor was selected as 7% which represents the most accurate results for entire cases, and the uncertainty of the breakup estimation in the case of Fig. 8

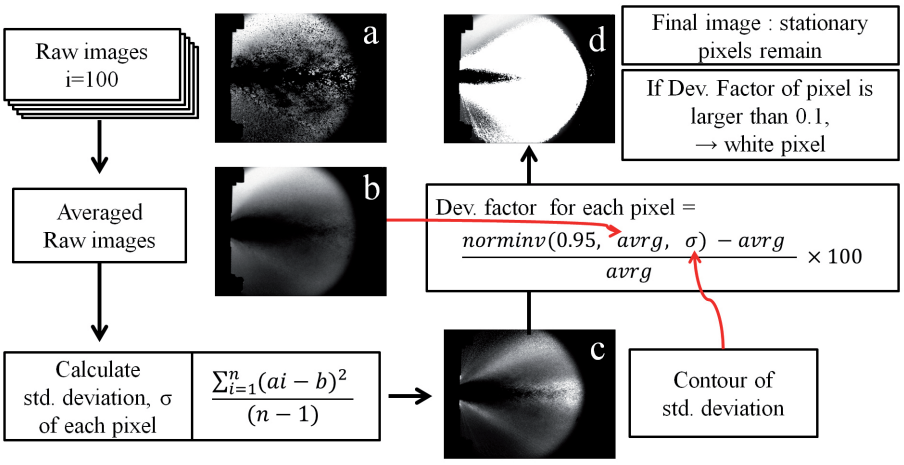

FIG. 6: The flow chart of image processing using Matlab

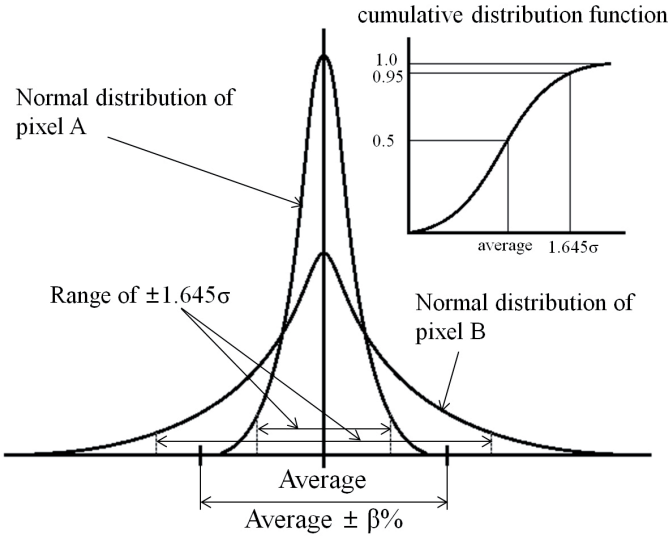

FIG. 7: Exclusion criterion for nonstationary pixels

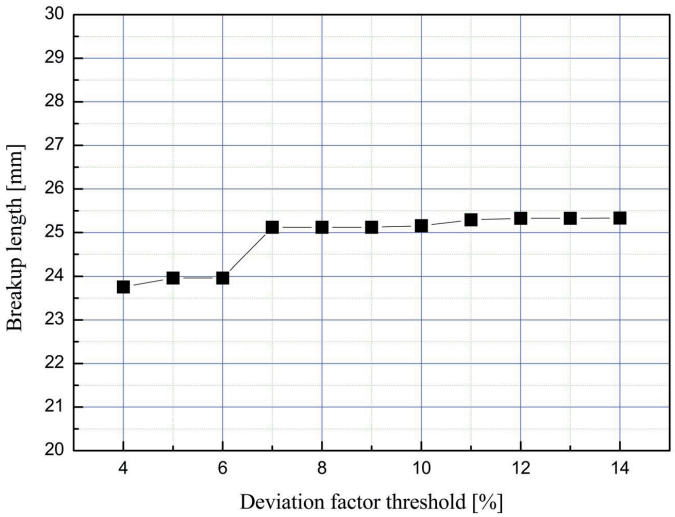

FIG. 8: Results of breakup length estimation with varying threshold

could be expressed in 25.1 + 0.2, –1.3 mm. The difference of upper and lower uncertainty was caused by the high sensitivity of the detecting algorithm at the low deviation factor threshold, and this tendency was represented in the whole case. Also, the uncertainties of the radial position of spray boundaries were calculated in the same manner.

2.4 Cold-Flow Test Conditions

The cold-flow experiment was carried out with the water-gaseous nitrogen simulant propellant, and the experimental conditions are summarized in Table 2. The mass flow rate of nitrogen was calculated by multiplying the volume flow rate and the density. The volume flow rate of gas was measured with the orifice flowmeter, and the density was estimated from the pressure and the temperature at the metering section. The mass flow rate range of gaseous nitrogen was between 20 and 40 g/s, and was controlled by adjusting the pressure regulator. The mass flow rate of water was constant at 217 g/s, and was validated by the bucket method. In this injection condition, the Reynolds number of the liquid jet was 28-166. In the cases of a porous injector configuration, the mass flow of water varied with the pressure at the recessed region, and it was compensated for by adjusting the pressure upstream of the liquid injector.

3. RESULTS AND ANALYSIS

3.1 Injection Parameters

In this study, the injection parameters J_{rcs} and J_{tip} define the degree of liquid-gas interaction at the recessed region and the injector tip respectively. The interaction between the gas and liquid jets from a porous injector can be classified into two types; (i) impinging of axial liquid jet and lateral gas jet at the recessed region, and (ii) shearing between axial liquid jet and axially developed gas jet downstream from the injector tip. So, the momentum flux ratio [Eq. (1)], which is usually employed as an index of the gas-liquid spray condition, could be divided into two types; the momentum flux ratio at the recessed region, J_{rcs}, and downstream of the injector tip, J_{tip}.

The static pressure at the recessed region of a porous injector was higher than the shear injector due to the stagnation of the lateral gas jet, and it consequently affected the density of the gas jet at the recess. The gas velocities at the recessed region, which were calculated from the continuity equation [Eq. (2)], varied depending on the gas density and the wall injection area (A_{prs}), which is determined by the length of the porous element. As a result, J_{rcs} could be different in the equal mass flow rate condition [Eq. (3)]. On the other hand, since the gas and liquid injection areas at the injector tips were the same for every injector used in this experiment, the magnitudes of J_{tip} were dependent on the mass flow rate ratio only [Eq. (4)].

Figure 9 shows the hydraulic parameters of a porous injector, which are divided into two calculating points: the recessed region and the injector tip. The Weber number

TABLE 2: Experimental conditions of the cold-flow tests

Liquid (water) mass flow rate, $\dot{m}_{\mathrm{liq}}$ (g/s)	217 g/s
Gas (gaseous nitrogen) mass flow rate, $\dot{m}_{\mathrm{gas}}$ (g/s)	20–40 g/s

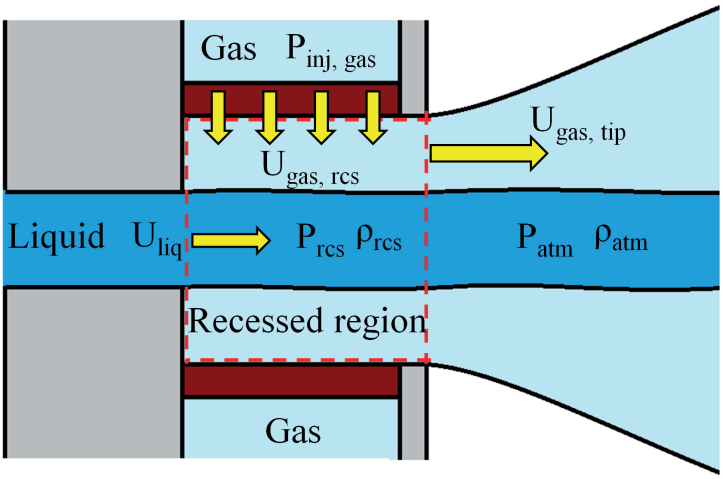

FIG. 9: Hydraulic parameters at the recessed region and injector tip

[Eq. (5)] represents the interaction between the gas and liquid jets, and is an index that demonstrates the relationship between the spray's inertia force and the surface tension of the liquid jet. In this study, the characteristic length is defined as the width of the two-dimensional injectors, and the surface tension of the liquid is based on the properties of water at room temperature and atmospheric pressure.

For each experiment, the mean values of spray conditions, momentum flux ratio, and Weber numbers were calculated, and listed in Table 3. Figure 10 shows the ratio of the radial gas momentum flux and the axial liquid momentum flux at the recessed region along with the axial momentum flux ratio at the injector tip. Since it is assumed that the gas jet at the recessed region of the shear injector has an axial vector only, the radial momentum flux ratio of the shear injector (INJ 1-1) is zero over the whole range. In the case of the porous injector (INJ 2-1–2-3), the radial momentum flux at the recessed region is proportional to the square of the mass flow rate of the gas, and inversely proportional to the square of the injection area, and to the pressure at the recessed region as described in Eq. (4). This is derived by substituting the density and velocity of gas in Eq. (2) by the ideal gas equation and Eq. (1), respectively. Since P_{rcs} increases along with the gas mass flow rate as shown in Fig. 11, J_{rcs} increases proportionally with the gas mass flow rate due to the effect of the increasing density of gas at the recess. At the same mass flow rate conditions, as defined by dashed boxes in Fig. 9, J_{rcs} of the porous injectors grows in a geometrical progression by proportionally increasing the injection area of the porous element.

The major difference in hydraulic characteristics between the shear injector and the porous injector is that the pressure at the recessed region of the porous injector is several times higher than the recess pressure of a shear injector. This causes the difference of

TABLE 3: Measured hydraulic parameters and calculated spray characterizing parameters

Inj. setup	**Expt. no.**	$\dot{m}_{\mathrm{gas}}$ (g/s) **Set/actual**	$P_{\mathrm{rcs,gas}}$ **(bar)**	$P_{\mathrm{diff,gas}}$ **(bar)**	$\boldsymbol{J}_{\mathrm{rcs}}$	$\boldsymbol{J}_{\mathrm{tip}}$	**We** ($\times 10^5$)
SHR INJ	1-1	20/20.74	0.087	1.03	21.155±0.91	22.28±0.81	0.998
1-1	1-2	25/24.77	0.055	1.46	31.090±1.11	31.78±0.99	1.423
Shear	1-3	30/29.67	0.040	2.00	45.246±1.67	45.60±1.21	2.041
injector	1-4	35/35.04	0.057	2.65	62.102±2.20	63.60±1.74	2.847
	1-5	40/39.8	0.094	3.26	77.396±2.94	82.05±2.14	3.673
PRS INJ	2-1	20/20.06	0.472	2.57	6.495±0.33	20.84±0.72	0.933
2-1	2-2	25/25.22	0.588	3.61	9.515±0.49	32.95±1.01	1.475
Porous	2-3	30/29.67	0.843	4.58	11.346±0.58	45.60±1.23	2.041
injector	2-4	35/35.01	0.934	5.73	15.047±0.75	63.49±1.71	2.842
L_{pr} = 1.5 mm	2-5	40/40.02	1.092	6.54	18.150±0.89	82.88±2.22	3.710
PRS INJ	3-1	20/20.0	0.381	1.20	1.72±0.09	20.72±0.77	0.927
2-2	3-2	25/24.97	0.522	1.44	2.435±0.12	32.30±1.10	1.446
Porous	3-3	30/29.77	0.757	1.97	2.999±0.15	45.91±1.30	2.055
injector	3-4	35/35.64	0.944	2.10	3.883±0.20	65.79±1.70	2.945
L_{pr} = 3.0 mm	3-5	40/39.72	1.204	3.22	4.254±0.22	81.72±2.39	3.658
PRS INJ	4-1	20/20.22	0.233	0.55	0.88±0.05	21.18±0.80	0.948
2-3	4-2	25/24.84	0.396	0.80	1.169±0.06	31.96±1.07	1.431
Porous	4-3	30/29.88	0.544	1.14	1.531±0.08	46.25±1.33	2.070
injector	4-4	35/34.73	0.699	1.51	1.878±0.10	62.48±1.62	2.797
L_{pr} = 4.5 mm	4-5	40/39.40	0.857	1.89	2.210±0.11	80.41±2.35	3.600

the momentum flux ratios at each case as explained above. The plot in Fig. 11 demonstrates the diminishing of P_{rcs} of INJ 2-1, which has the shortest porous element length, at the gas mass flow rate condition of 35 g/s. This occurs because the radial gas jet, which injects from the opposite side, is released outside of the injector before forming a stagnation region.

3.2 Macroscopic Spray Patterns

The instant images of a spray from each injector exhibit the differences in the macroscopic spray patterns quite well in Fig. 12. The three pictures in each row are sequential images with an elapsed time of 0.88 ms, and the mass flow rates of simulant propellant are the same in all cases as described in the caption. These pictures show the differences in the gas-liquid interaction at the outside of the injectors. In the case of the shear injector [Fig. 12(a)], the gas jet, which is injected parallel to the liquid core, contacts the unstable surface of the liquid jet. The arrows in Fig. 12 point to the location of the acting shear force, which induces the disintegration of the liquid jet. The axial positions of the

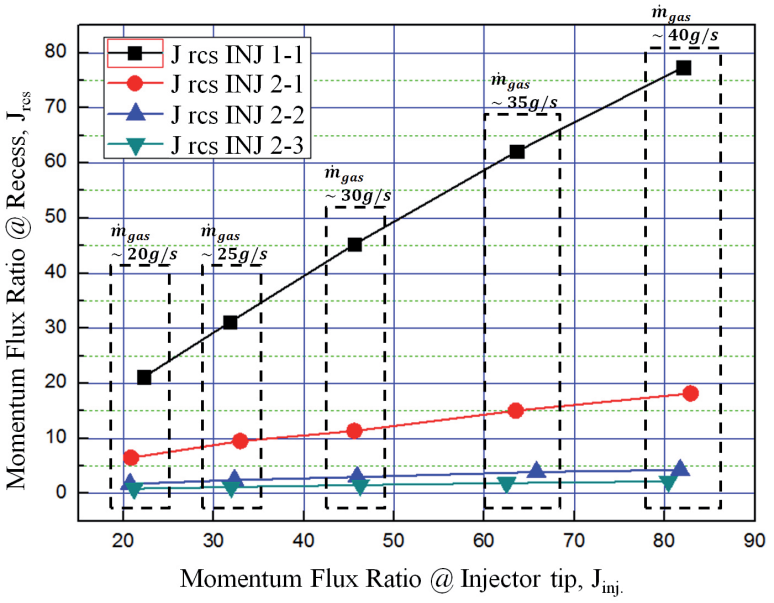

FIG. 10: Radial momentum flux ratio at the recessed region versus axial momentum flux ratio at the injector tip

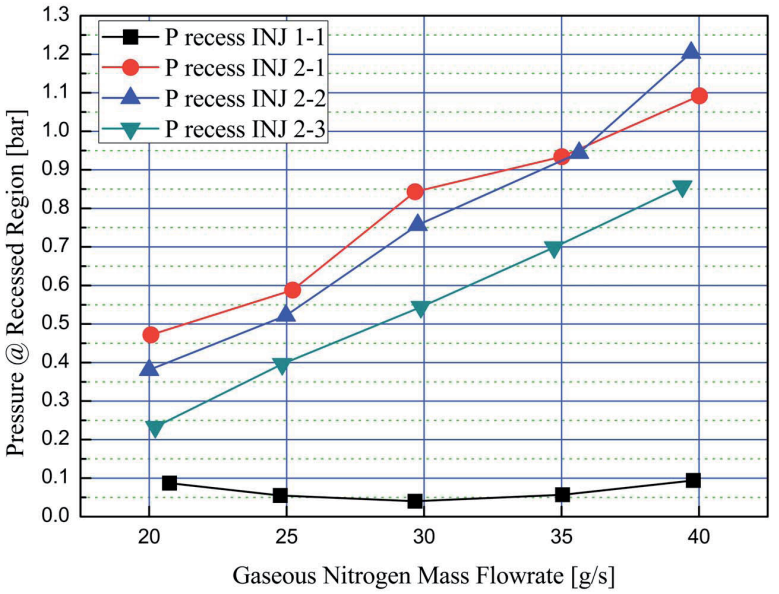

FIG. 11: Mean static pressures at the recessed region for varying mass flow rate of gaseous nitrogen

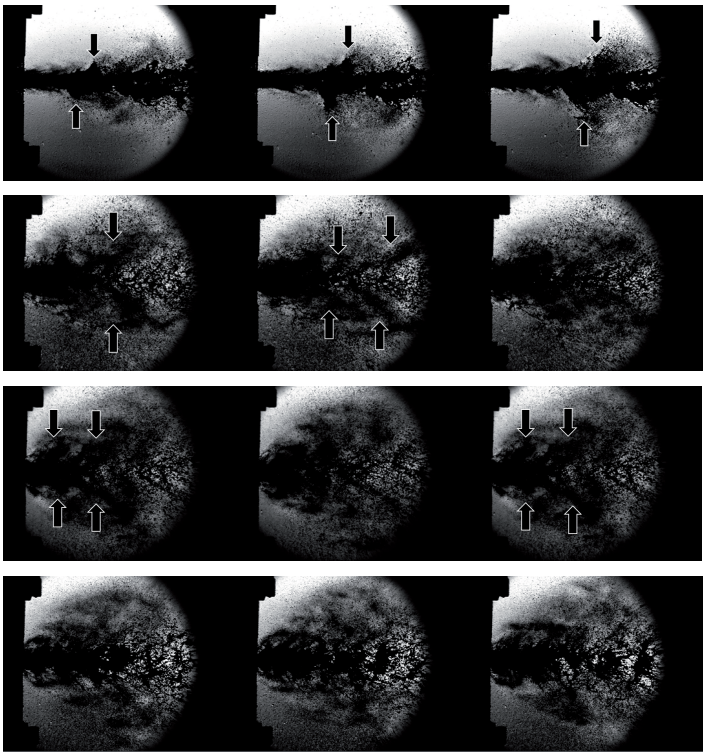

FIG. 12: Representative sequential images of gas-liquid spray from each configuration of injectors

shearing point at the upper and lower sides of the liquid core appear alternatively in the axial direction due to the sinusoidal shape of the liquid core. The spray images of the porous injector shown in Figs. 12(b)–12(d) demonstrate the rapid and uniform breakup of the liquid core. The differences between the injectors used in Figs. 12(b)–12(d) are the porous element lengths (L_{pr}): 1.5, 3.0 and 4.5 mm, respectively. The length of the porous element determines the magnitude of the radial momentum flux of the gas jet and the residence time of the liquid jet in the recessed region. Comparing the pictures, they show that the porous element length affects the uniformity of the spread of the liquid. The liquid jet from the injector was rarely disintegrated at the center line while using the longest porous element length (4.5 mm), as shown in Fig. 12(d). As L_{pr} increases, the atomization of the liquid jet is better, and the spray pattern shows a widely dispersing liquid jet in a V shape. On the other hand, the spray angle was observed to remain almost unchanged.

The major difference between the shear injector and the porous injector is the spray angle. The spray angle of the shear injector is narrower than that of the porous injector.

The liquid core of the shear injector is scattered further downstream from the injector face, and it is determined that the axial velocity component of the droplet is dominant. In contrast, the disintegration of the liquid core from the porous injector occurs at the recessed region (inside the injector), and the fine droplets dispersed into a wide area.

$$J = \frac{\rho_{\mathrm{gas}} U_{\mathrm{gas}}^2}{\rho_{\mathrm{liq}} U_{\mathrm{liq}}^2} \tag{1}$$

$$U_{\mathrm{gas}} = \frac{\dot{m}}{\rho_{\mathrm{gas}} A} \tag{2}$$

$$J_{\mathrm{rcs}} = \frac{\dot{m}_{\mathrm{gas}}^2 RT}{P_{\mathrm{rcs}} A_{\mathrm{prs}}^2 \rho_{\mathrm{liq}} U_{\mathrm{liq,axial}}^2} = J(\dot{m}_{\mathrm{gas}}^2, P_{\mathrm{rcs}}^{-1}, A_{\mathrm{prs}}^2) \tag{3}$$

$$J_{\mathrm{tip}} = \frac{\dot{m}_{\mathrm{gas}}^2 RT}{P_{\mathrm{atm}} A_{\mathrm{tip,gas}}^2 \rho_{\mathrm{liq}} U_{\mathrm{liq,axial}}^2} = J(\dot{m}_{\mathrm{gas}}^2, A_{\mathrm{tip,gas}}^{-2}) \tag{4}$$

$$\mathrm{We} = \frac{\rho_{\mathrm{gas,amb}} (U_{\mathrm{gas,tip}} - U_{\mathrm{liq}})^2 w}{\sigma} \tag{5}$$

3.3 Breakup Length Analysis

The spray angle and the breakup length were analyzed using the image processing technique described above. Figure 13 shows the results of the spray angle and the liquid core detecting process, and these pictures are arranged by gas flow rate and injector type. The post-processed images in each row were captured at similar mass flow rate ratio (J_{tip}) conditions, and the injector type and geometry were divided into separate columns. The J_{rcs} magnitudes of each case were represented on each image in Fig. 13. Though the mass flow rate ratios were similar, J_{rcs} were calculated differently according to the injector type. The first column from the left side shows the spray images of the shear injector. The spray images of the porous injectors, with cylinder lengths of 1.5, 3.0, and 4.5 mm, are on the second, third, and fourth columns respectively.

Both the breakup lengths and the degree of spray dispersions were definitely different depending on the type of injector, especially in the high J_{tip} conditions. Figures 14 and 15 show the effects of the injection conditions on the breakup length and the degree of dispersion quantitatively. The breakup lengths were measured from Fig. 13, and determined by the distance from the injector face plate to a discrete point in the center liquid core.

In the shear injector experiment, the liquid disintegration at the center region was not improved significantly though the gas injection flow rate increased, and the breakup length rather became longer as shown in Fig. 13. These results contradict previous findings about the behavior of general coaxial shear injectors (Davis and Chehroudi, 2005). It

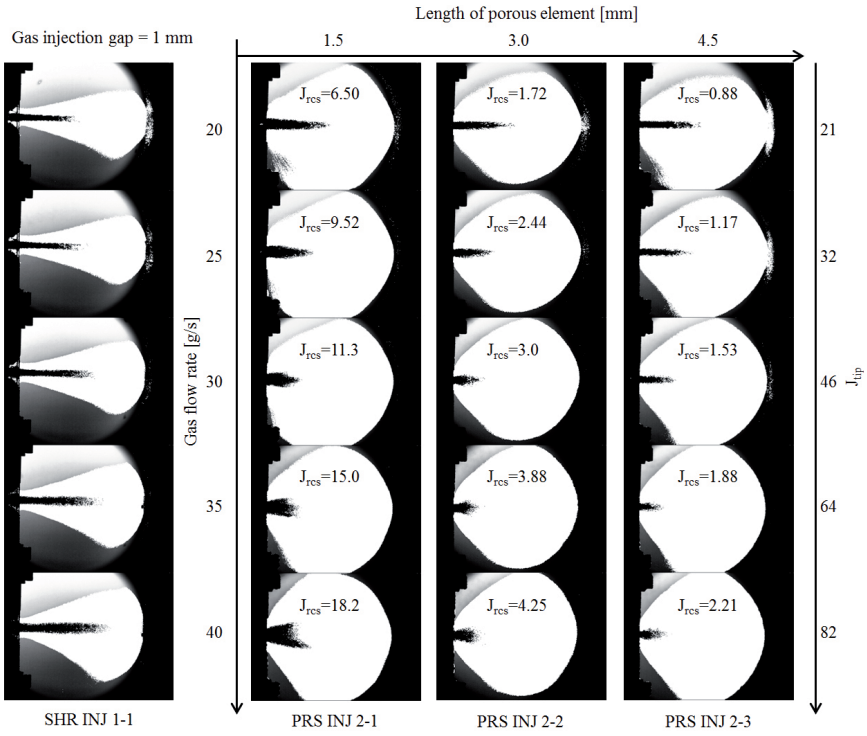

FIG. 13: Effects of J_{tip} and J_{rcs} on the breakup length and the dispersion angle of spray

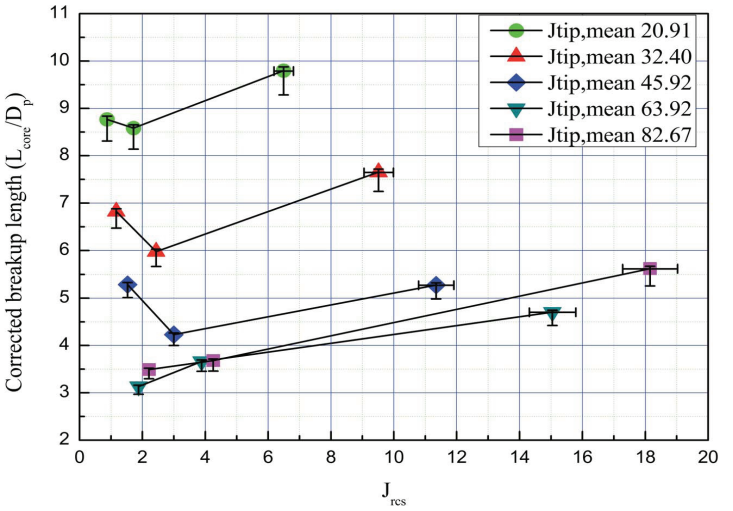

FIG. 14: The effect of J_{rcs} and J_{tip} on the corrected breakup length of the porous injectors

was thought that the breakup lengths at the low J_{tip} conditions were underestimated due to the wavy breakup patterns. At the low momentum flux ratio condition, the liquid jet disintegrated in the fiber-type breakup mode, which showed a nonsymmetric, sinusoidal, wavy liquid column downstream of the spray (Farago and Chigier, 1992). Therefore, the post-processing code predicted the breakup length to be shorter. In contrast, the breakup length of the porous injectors was shortened with the increasing gas flow rate (increasing J_{tip}).

In the cases of the short porous element length (1.5 mm) and high mass flow rate of the gas jet (higher than 35 g/s), the wide spread of the liquid core was observed at the nearinjector field, and the detected liquid core seemed like a flipper. Possible reasons for the change in the shape of the liquid core are that the radial gas jet did not develop to the axial flow completely at the short recessed region, and a larger radial momentum acted on the liquid jet at the outside of the injector tip.

In order to analyze the effect of the radial momentum of the gas jet on the liquid breakup, the breakup length variation according to the J_{rcs} and J_{tip} was plotted in Fig. 14. The symbols that are linked by a solid line indicate the equal mass flow rate ratio and J_{tip}. The increasing J_{tip} (increasing gas mass flow rate) reduced the breakup length of three porous injector configurations, and the breakup lengths of the porous injectors got much shorter than that of the shear injector.

As described in Eq. (4), J_{rcs} is a function of the gas mass flow rate, the recess pressure and the gas injection area of the porous element. The change of the J_{rcs} of each plot in Fig. 14 is due to the varying gas injection area. (i.e. the length of the porous element). Therefore, the effect of the length of the porous element (J_{rcs}) on the disintegration of the liquid jet could be observed. In the case of J_{tip} with values from 20.91 to 45.92, the breakup lengths showed a decreasing-increasing tendency according to the increasing J_{rcs}. It was thought that an optimal porous element length exists that would create the shortest breakup length. This optimal length is thought to be between the values of 1.5 and 4.5 mm. In the higher J_{tip} conditions, however, the increasing J_{rcs} induced a longer breakup length. The higher J_{rcs} and shorter recessed depth made the liquid core spread wider at the near-injector field, and much of the gas jet momentum was consumed in this process. In conclusion, it could be deduced that increasing the J_{rcs} by shortening the porous element is not a good way to improve the liquid disintegration, and there are optimal porous element lengths at each given J_{tip} magnitude.

3.4 Spray Dispersion Analysis

Figure 14 shows the radial distribution of the spray according to the axial position for each test condition, and the boundary positions were measured from Fig. 13. Figure 15(a) represents the spatial distribution of the shear injector spray at each gas flow rate (J_{tip}) condition. As the magnitude of J_{tip} increased, a wider spray angle was demonstrated. Figures 15(b)–15(f) show the change of the spray distribution according to the length of

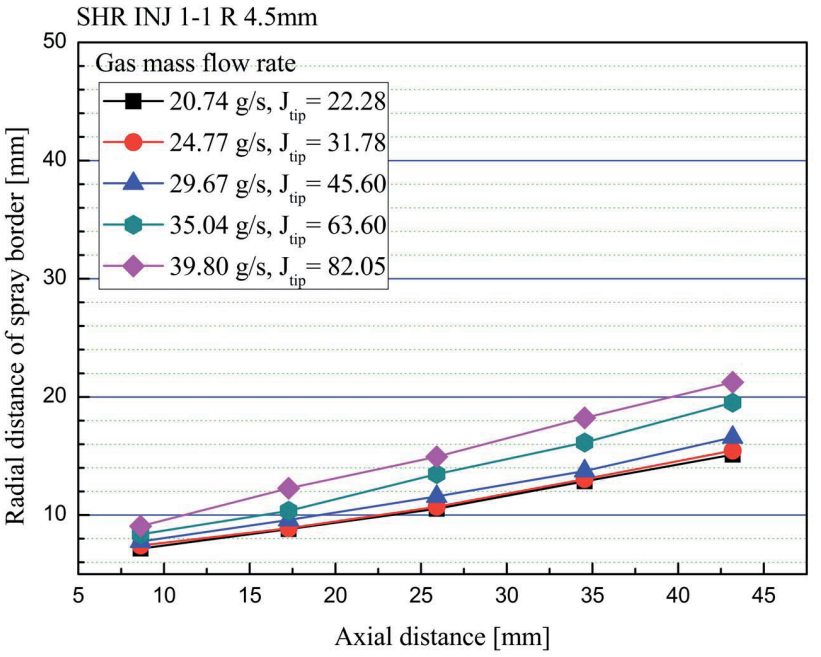
SHR INJ 1-1 R 4.5mm
Gas mass flow rate
20.74 g/s, J tip = 22.28
24.77 g/s, J tip = 31.78
29.67 g/s, J tip = 45.60
35.04 g/s, J tip = 63.60
39.80 g/s, J tip = 82.05
Radial distance of spray border [mm]
Axial distance [mm]

(a)

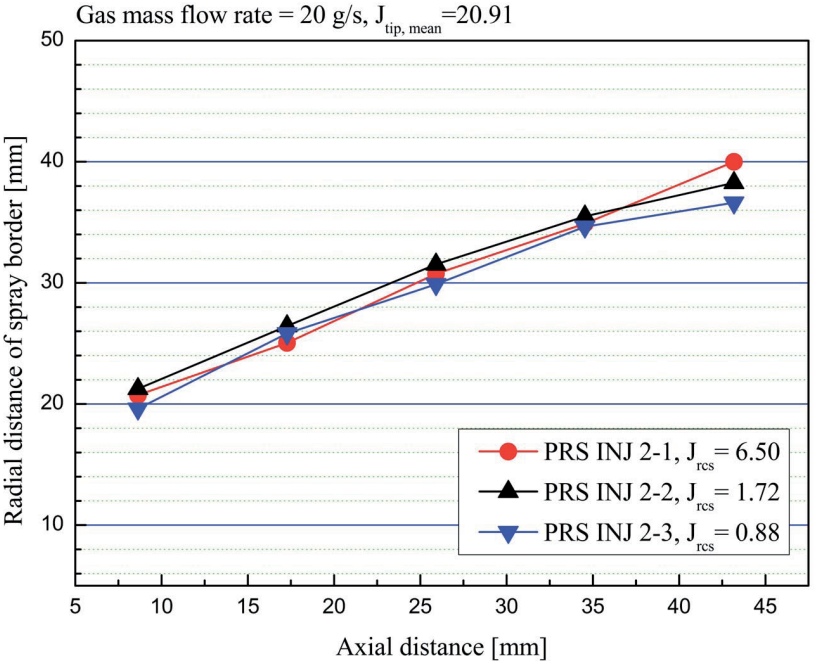
Gas mass flow rate = 20 g/s, J tip, mean =20.91
PRS INJ 2-1, J rcs = 6.50
PRS INJ 2-2, J rcs = 1.72
PRS INJ 2-3, J rcs = 0.88
Radial distance of spray border [mm]
Axial distance [mm]

(b)

FIG. 15

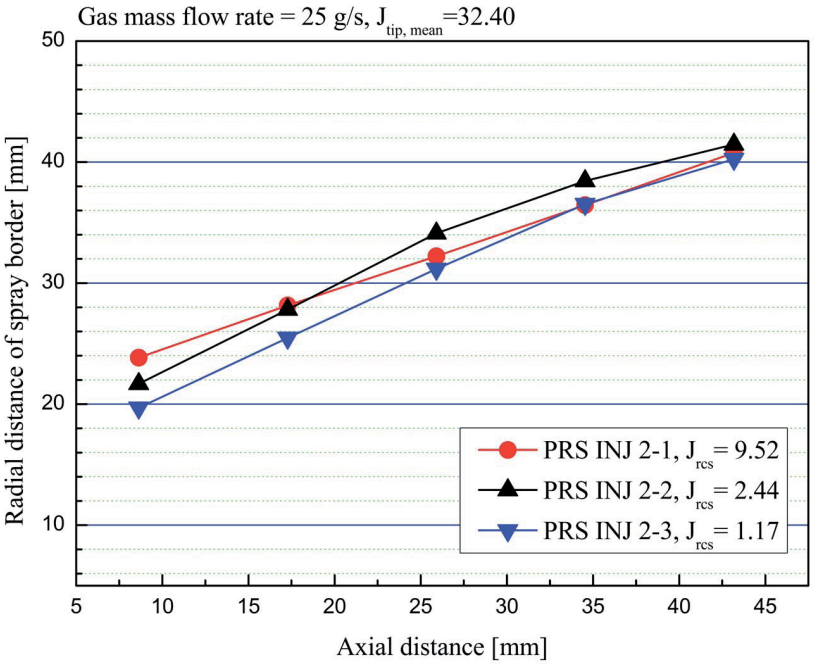
Gas mass flow rate = 25 g/s, J tip, mean =32.40
Radial distance of spray border [mm]
Axial distance [mm]
PRS INJ 2-1, J rcs = 9.52
PRS INJ 2-2, J rcs = 2.44
PRS INJ 2-3, J rcs = 1.17

(c)

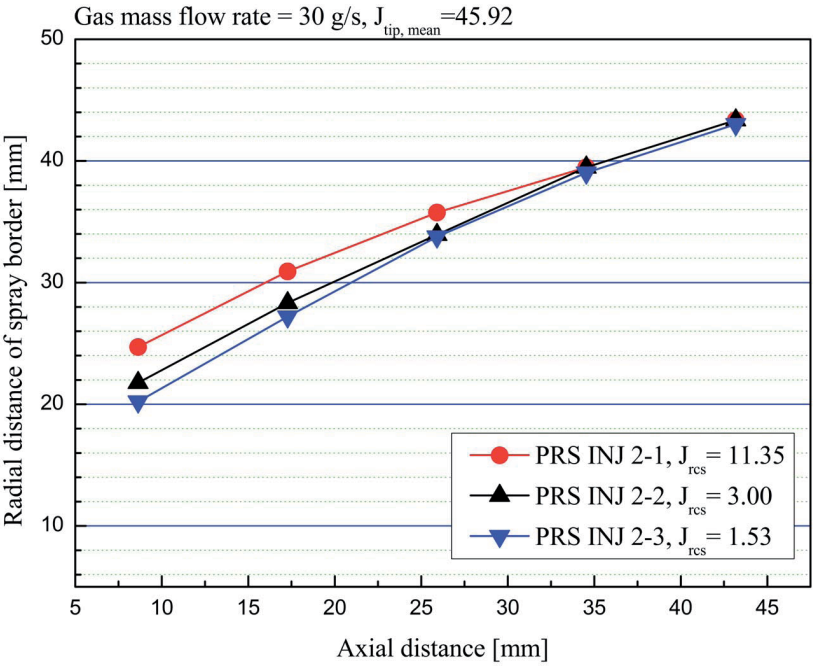
Gas mass flow rate = 30 g/s, J tip, mean =45.92
Radial distance of spray border [mm]
Axial distance [mm]
PRS INJ 2-1, J rcs = 11.35
PRS INJ 2-2, J rcs = 3.00
PRS INJ 2-3, J rcs = 1.53

(d)

FIG. 15

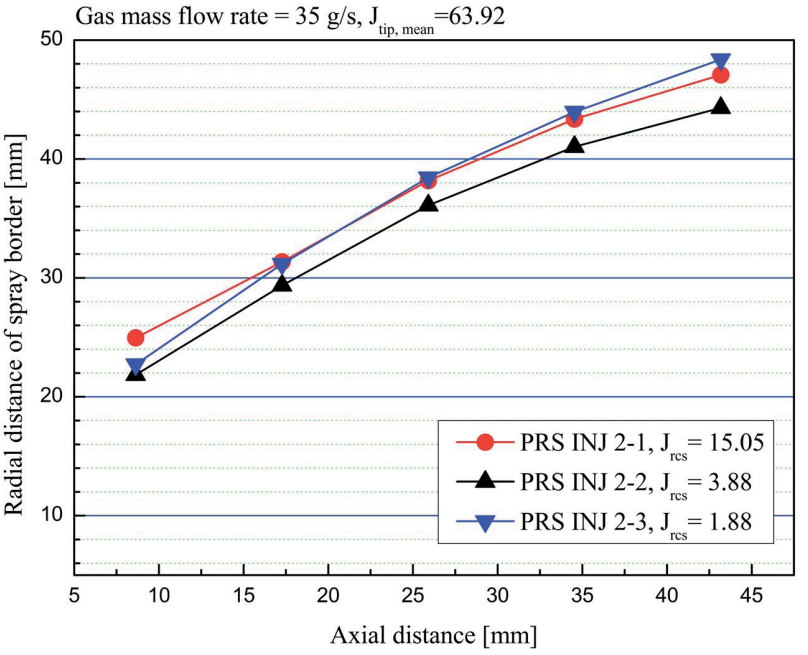

(e)

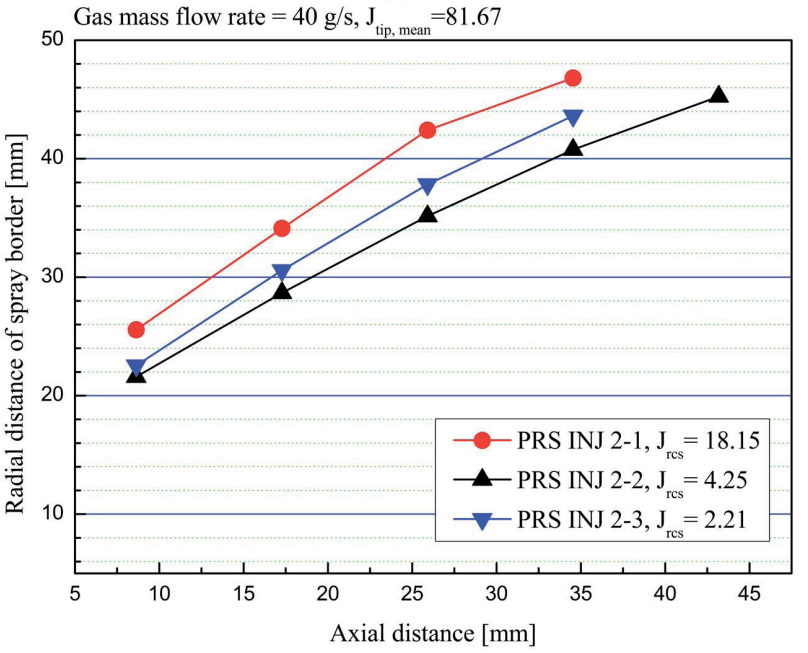

(f)

FIG. 15: Radial distribution of the spray border line at each experimental case

the porous element in each J_{tip} condition. In the same manner as the breakup length, the spray distribution was varied by J_{rcs} more significantly in the higher J_{tip} conditions.

For the injector with the shortest length of the porous element (PRS INJ 2-1), the spray at the injector face plate was spread wider proportional to J_{tip} for the same reason mentioned in Section 3.1 [Fig. 15(d)]. As the J_{tip} magnitude further increased to 63.92 [Fig. 15(e)], the spray of PRS INJ 2-3, which had the longest porous element, spread as widely as the spray of PRS INJ 2-1, except at the nearinjector field. However, the spray of PRS INJ 2-2 had little change between Figs. 15(d) and 15(e) in the lateral distribution at the entire axial position. At the highest J_{tip} condition [Fig. 15(f)], the spray of PRS INJ 2-1 was dispersed dramatically wider than the other injector configurations, and it could be deduced that the cause of this phenomenon was correlated with the lateral scattering of the liquid core as shown in Fig. 13. The notable point was that the dispersion degree of the PRS INJ 2-2, which had a medium porous element length among the experimental group, was rarely varied despite the increased J_{tip} magnitude.

4. CONCLUSION

The macroscopic pattern, the breakup length and the spatial distribution of spray from the porous injector were studied using an atmospheric pressure cold-flow test using water and gaseous nitrogen as simulants for liquid and gaseous propellants, respectively. The spray visualization results of quasi-2D injectors clearly represented the effects of lateral gas injection on the spray dispersion in a lateral direction and the disintegration of the center liquid jet. Also, the results were compared with those of the shear injector configuration. The following conclusions were elicited:

(i) The lateral gas injection of the porous injector induces a pressure buildup at the recessed region. In the condition of a short porous element length and high mass flow rate of the gas jet, the diminishing of the recess pressure occurred due to the lack of the space to stagnate, and the gas jet discharged to the outside of the injector with relatively higher radial momentum. As a result, the liquid core spread widely at the exit plane of the injector.

(ii) The spray from the porous injector shows higher breakup performance, wider spray angle, and a more uniform distribution of the two-phase spray than the shear injector. The differences were caused by the lateral momentum of the gas jet.

(iii) The breakup length of a porous injector is shortened with the increasing J_{tip}. In the cases of the equal J_{tip} magnitude, the shortest breakup lengths were observed in the middle range of J_{rcs}, which was varied by changing the length of the porous element. At the high J_{tip} condition, the breakup lengths were lengthened with increasing J_{rcs}.

(iv) J_{rcs} affected the spray dispersion of a porous injector less in the low J_{tip} conditions. The lateral gas jet momentum intensifies the spreading of spray at the near-injector field. Further increases in J_{tip} and J_{rcs} by increasing gas flow rate induced the lateral spread of the entire spray (both of the near-injector field and downstream of the spray).

(v) From the breakup length and dispersion degree analysis results, it was thought that an optimal porous element length for the best mixing performance exists at certain injection conditions. These optimal lengths can be defined through further studies of the correlation between the lateral momentum transfer and the behavior of the liquid core at the near-injector field.

(vi) The future study will involve a quantitative comparison of the droplet size and the mass distribution between the porous and the shear injector. The results from the quantitative measurements are expected to verify the improved atomization and mixing of the porous injector.

ACKNOWLEDGMENTS

This work was supported by the National Research Foundation of Korea (NRF) grant funded by the Korean Government (MEST) (NRF-2011-0015435 and NRF-2012M 1A3A3A02033 146).

REFERENCES

Abernethy, R. B., Benedict, R. P., and Dowdell, R. B., ASME measurement uncertainty, *J. Fluids Eng*., vol. 107, pp. 161–163, 1985.

Bazarov, V. G., A New class of porous injectors for combustion chambers and gas generators, In *Proc. of AIAA/SAE/ASME/ASEE 29th Joint Propulsion Conference and Exhibit*, 1993.

Davis, D. W. and Chehroudi, B., Shear-coaxial jets from a rocket-like injector in a transverse acoustic field at high pressures, In *Proc. of 44th AIAA Aerospace Sciences Meeting and Exhibit*, 2005.

Deeken, J., Suslov, D., Haidn, O., and Schlechtriem, O., Design and testing of a porous injector head for transpiration cooled combustion chambers, In *Proc. of 48th AIAA Aerospace Sciences Meeting Including the New Horizons Forum and Aerospace Exposition*, 2010.

Farago, Z. and Chigier, N., Morphological classification of disintegration of round liquid jets in a coaxial air stream, *J. Atomization Sprays*, vol. 2, pp. 137–153, 1992.

Huzel, D. K. and Huang, D. H., *The Design of Liquid Propellant Rockets*, 2nd ed., Washington DC: National Aeronautics and Space Administration, 1971.

Kline, S. J., The purposes of uncertainty analysis, *J. Fluids Eng*., vol. 107, pp. 153–160, 1985.

Lux, J., Suslov, D., and Haidn, O., Experimental Investigation of porous injectors for liquid propellant rocket engines, In *Proc. of 44th AIAA/ASME/SAE/ASEE Joint Propulsion Conference and Exhibit*, 2008a.

Lux, J., Suslov, D., and Haidn, O., Porous injectors in cryogenic liquid propellant rocket engines at sub- and supercritical pressures, In *Proc. of 46th AIAA Aerospace Sciences Meeting and Exhibit*, 2008b.

Polyaev, V. M., Zhdanov, V. M., and Kichatov, B. V., Study of the operation of a gasliquid atomizer with a porous mixing element, *J. Eng. Phys. Thermophys*., vol. 73, no. 3, pp. 465–469, 2000.

Qian, L., Lin, J., and Xiong, H., A Fitting formula for predicting droplet mean diameter for various liquid in effervescent atomization spray, *J. Thermal Spray Technol*., vol. 19, no. 3, pp. 586–607, 2009.

Qian, L., Lin, J., and Xiong, H., Effects of operating conditions on droplet deposition onto surface of atomization impinging spray, *J. Surface Coating Technol*., vol. 203, pp. 1733–1740, 2009.

Rahman, S. A., *Primary Atomization Study of a Swirl Coaxial Liquid Propellant Rocket Injector*, Ph.D. Thesis, The Pennsylvania State University, 1997.

Rahman, S. A., Pal, S., and Santoro, R. J., Swirl coaxial atomization—Cold-flow and hot-fire experiments, In *Proc. of 33rd Aerospace Sciences Meeting and Exhibit*, 1995.

Atomization and Sprays, 24 (1): 23–40 (2014)

THEORETICAL ANALYSIS OF SURFACE WAVES ON A ROUND LIQUID JET IN A GASEOUS CROSSFLOW

S. L. Wang, Y. Huang,* & Z. L. Liu

National Key Laboratory on Aero-Engines, School of Energy and Power Engineering, Beihang University, Beijing, 100191, China

*Address all correspondence to Y. Huang E-mail: yhuang@buaa.edu.cn

Original Manuscript Submitted: 7/12/2013; Final Draft Received: 9/30/2013

A theoretical investigation is described to study the surface waves on a round liquid jet in a gaseous crossflow, especially Rayleigh-Taylor waves. The linear stability analysis was used to derive the dispersion relation. The acceleration on the liquid jet due to the transverse aerodynamic force was considered in the relation. Results indicate that the hydrodynamic instability is dominated by three terms which are caused by jet velocity, surface tension, and aerodynamic force, respectively. The surface tension contributes to the instability when the wave number is less than unity. Both gas and jet velocities can affect the optimum wavelength and the surface wave growth rate. The critical momentum ratio, at which the contribution of the liquid jet Weber number to the maximum growth rate is as large as that of the cross air Weber number to the maximum growth rate, decreases with the gas Weber number exponentially. If the momentum ratio is less than the critical value, the axial optimum wavelength can be expressed as a power function of gas Weber number. Otherwise, free jet instability theory can be used to study the surface waves on the liquid jet in cross air flow.

KEY WORDS: *linear stability analysis, round liquid jet, crossflow, Rayleigh-Taylor waves, momentum ratio*

1. INTRODUCTION

Liquid fuel sprays in crossflows have a wide application in a number of aerospace systems, such as afterburners (Lovett et al., 2004), gas turbine combustors, liquid rocket engines, ramjet engines, and scramjet engines (Ali and Islam, 2006; Pandey et al., 2010). The atomization is achieved through two stages: primary breakup and secondary breakup. The present study is to investigate the characteristics of the primary breakup of a liquid jet in a gaseous crossflow.

Numbers of earlier studies revealed the characteristics of the primary breakup of a liquid jet in supersonic crossflow. Kolpin and Horn (1968), Reichenbach and Horn (1971), and Nejad et al. (1980) investigated the jet penetration and mean droplet diameter by experiments in supersonic air streams. Heister et al. (1988) presented a model

1044–5110/14/$35.00

of a single liquid jet in compressible supersonic crossflow. Kush and Schetz (1972) experimentally studied a liquid jet in a supersonic flow. High frequency, large amplitude, aerodynamically induced, axially propagating waves were observed in their experiments. Such waves were considered to be intrinsic for liquid jet breakup behavior and to be the dominant mechanism of jet decomposition. Similarly, Schetz et al. (1980) conducted the experiments of liquid jets in supersonic gas streams to investigate the characteristics of surface waves and their influence on the jet breakup process. Their results pointed out that the transverse liquid jet breakup was caused by the acceleration waves rather than surface tension waves or Kelvin-Helmholtz (K-H) waves.

Since the 1990s, much attention was paid to transverse jets in subsonic gaseous crossflows due to the development of low emission combustors, such as LPP (lean premixed prevaporized) (Becker and Hassa, 2002). Zhu et al. (2010), Inamura (1999), and Wu et al. (1997) investigated the trajectory of liquid jets in cross airstreams. Stenzler et al. (2006), Wang et al. (2011), and Mashayek et al. (2008) studied the jet penetration in crossflows. Aalburg et al. (2004) experimentally investigated the ligament and drop properties along the liquid surface in crossflow. Wu et al. (1997, 1998) experimentally studied the breakup process of liquid jets in subsonic crossflow, and presented the column trajectories, column fracture locations, spray structure, and column surface wave characteristics. Their results showed that (a) the liquid column breakup processes in a crossflow are similar to those of aerodynamic secondary breakup of a spherical droplet; (b) surface waves which generated the ligaments and droplets initiate from the column periphery and extend to the leeward side. They also found that the wavelength of surface waves and the size of ligaments and droplets decreased with the increase of the gas velocity. Fuller et al. (1997) investigated the effect of injection angle on the breakup process of liquid jets in subsonic crossflows by experiments. They divided the column breakup into aerodynamic and nonaerodynamic regimes. For aerodynamic breakup, the aerodynamic forces associated with gas crossflow accelerated the column in jet stream direction and induced surface waves which ultimately led to column fracture. While for nonaerodynamic breakup, liquid turbulence and inertial forces generated instability within the liquid itself and caused large scale column deformations which ultimately led to column fracture. Mazallon et al. (1999) carried out numerous experiments to observe the jet deformation and breakup. Their observations also suggested qualitative similarities between breakup of nonturbulent liquid jets in crossflows and the secondary breakup of droplets. The jet breakup in subsonic crossflow is typically classified into four primary regimes: column breakup, bag breakup, multimode breakup, and shear breakup. Their results also indicated that the wavelengths of surface waves and column waves decreased with the increase of gas Weber number. Sallam et al. (2004) pointed out that the ratio of wavelength to jet diameter is greater than unity for column breakup, approximately equal to unity for bag breakup, and less than unity for shear breakup mode. Meanwhile they proved the similarities by experiments and concluded that the transitions to bag, multimode, and shear breakup occurred at We_g = 4, 30, and 110, respectively. But Zheng and

Marshall (2011) found that breakup mode transition from column to bag breakup was at We_g = 8. Sedarsky et al. (2010) conducted numerous experiments and found classical Rayleigh-Taylor (R-T) wave structures which grow and pinch off the liquid jet. Wang et al. (2012) and Ng et al. (2008) studied the properties of bag breakup of liquid jet in crossflow and analyzed waves induced by R-T instability. Their results suggested that the wavelength directly decreased with the increase of gas Weber number.

The objective of the present investigation was to study the instability of a round liquid jet in gaseous crossflow using linear stability theory. This method was adopted by Sterling and Sleicher (1975), Reitz and Bracco (1982), Lin and Lian (1988), Yang et al. (2012), and Boronin et al. (2013) to describe the instability of a round liquid jet injecting into quiescent air. Panchagnula et al. (1996) studied the instability of a swirling annular liquid jet into coaxial gas streams with unequal gas velocities by this theory. The column surface waves, especially induced by R-T instability, on the liquid jet in crossflow will be studied, and the effects of dominating parameters will be discussed.

2. INSTABILITY ANALYSIS

Considering a round liquid jet with radius *a*, constant density ρ_l penetrates at speed U_l into the gaseous crossflow. The transverse gas velocity is U_g. The gas and the liquid flows are assumed to be incompressible and inviscid.

The governing equations consist of continuity equations and momentum equations in *r*, θ and *z* directions. The coordinate origin is fixed at the center of nozzle exit and *z* axis coincides with the axis of the column of jet as shown in the Fig. 1(a). Figure 1(b) shows the jet cross section around which the gas flow passes.

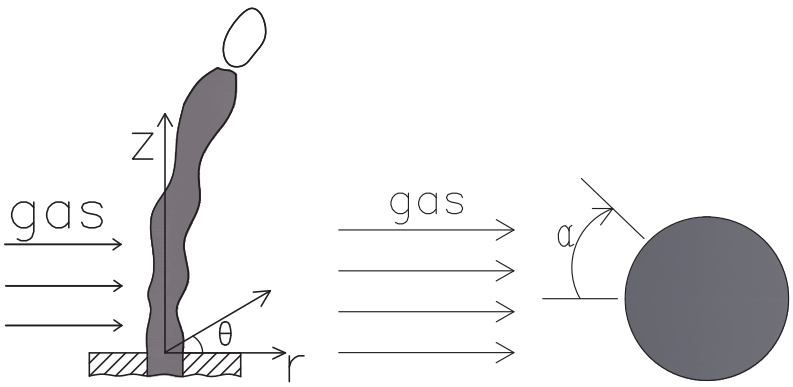

FIG. 1: Model of a round liquid jet in crossflow: (a) longitudinal-section, (b) cross-section

Here, the initial section at the nozzle exit where the surface waves have been formed is the most concerned, because the disturbance convects along the liquid jet and the surface wavelength does not change significantly (Karagozian, 2010; Sedarsky et al., 2010). Thus, the deflection of the liquid column in the streamwise direction of the gaseous crossflow and the cross-section deformation of the liquid jet in the initial section are neglected.

$$\nabla \cdot V_j = 0, \quad \frac{\partial}{\partial t} V_j + (V_j \cdot \nabla) V_j = -\frac{1}{\rho_j} \nabla p_j, \quad j = l, g \tag{1}$$

where the subscript $j = l$ denotes the liquid and $j = g$ denotes the gas, ∇ is the gradient operator. Initial velocities of the fluids in cylindrical coordinate are $V_l = (0, 0, U_l)$, $V_g = (v_g, w_g, 0)$. Therefore in the initial section of the jet, the crossflow passing a liquid jet can be analogized as a gas stream passing a cylinder. The velocity components v_g and w_g can be expressed as

$$v_g = U_g \left(1 - \frac{a^2}{r^2}\right) \cos \alpha \tag{2}$$

$$w_g = -U_g \left(1 + \frac{a^2}{r^2}\right) \sin \alpha \tag{3}$$

where α is the circumferential angle as shown in Fig. 1(b).

The flows are perturbed by an infinitesimal perturbation written as a normal mode form, and the interface of the liquid jet has the shape (Shen and Li, 1996)

$$r = a + \eta(\theta, z, t) = a + \eta_0 e^{i(kz + m\theta) + \omega t} \tag{4}$$

where η is the displacement of interface and η_0 is initial displacement of the interface. t is time. k and n are the wave number of the perturbation in z and θ directions, respectively. ω is a complex frequency, $\omega = \omega_R + i\omega_I$, where the real part ω_R denotes the growth rate, and the imaginary part ω_I denotes the disturbance wave frequency. As there is no vorticity initially in the flow, the flow is expected to be irrotational, i.e.,

$$\nabla^2 \Phi_j = 0, \qquad j = l, g \tag{5}$$

Then the velocity potentials can be written as

$$\Phi_l = U_l z + \Phi_l' \tag{6}$$

$$\Phi_g = U_g \left(r + \frac{a^2}{r}\right) \cos \alpha + \Phi_g' \tag{7}$$

and

$$u_j' = \nabla \Phi_j', \qquad j = l, g \tag{8}$$

$$\nabla^2 \Phi'_j = 0, \qquad j = l, g \tag{9}$$

where the superscript $'$ represents the disturbance quantities which are written as

$$\Phi'_l = \phi_l(r) e^{i(kz+m\theta)+\omega t} \tag{10}$$

$$\Phi'_g = \phi_g(r) e^{i(kz+m\theta)+\omega t} \tag{11}$$

The solutions $\phi_j(r)$ $(j = l, g)$ must satisfy the Ordinary Differential Equation boundary conditions, $\phi_l(r) \to 0$, as $r \to 0$, $\phi_g(r) \to 0$, as $r \to \infty$. Then Eqs. (10) and (11) are equal to

$$\Phi'_l = AI_m(kr) e^{i(kz+m\theta)+\omega t} \tag{12}$$

$$\Phi'_g = BK_m(kr) e^{i(kz+m\theta)+\omega t} \tag{13}$$

where $I_m(kr)$ and $K_m(kr)$ are mth-order modified Bessel function of the first kind and second kind, respectively. A and B are constants depending on the boundary conditions. On the interface between the liquid column and the gas, Φ'_l and Φ'_g must satisfy the kinematic and dynamic boundary conditions.

The kinematic boundary condition is that there is no net flux of mass across the liquid column surface, i.e.,

$$\frac{\partial \Phi'_l}{\partial r} = \frac{\partial \eta}{\partial t} + U_l \frac{\partial \eta}{\partial z}, \quad \text{at} \quad r \approx a \tag{14}$$

$$\frac{\partial \Phi'_g}{\partial r} = \frac{\partial \eta}{\partial t} - \frac{U_g}{r}\left(1 + \frac{a^2}{r^2}\right) \sin\alpha \frac{\partial \eta}{\partial \theta}, \quad \text{at} \quad r \approx a \tag{15}$$

For the dynamic boundary condition, the gas static pressure p_g on the interface between the liquid column and the gas is expressed as (Young et al., 2001)

$$p_g = p_\infty + \frac{1}{2}\rho_g U_g^2 (1 - 4\sin^2\alpha) \tag{16}$$

where p_∞ is the gas static pressure far away from the liquid jet without disturbances. The dynamic boundary condition requires that the stress tensor must be continuous across the interface,

$$p_l - p_g = \Delta p \tag{17}$$

where Δp is the pressure jump due to the surface tension of the liquid jet. Thus the dynamic boundary condition can be written by combining Eqs. (16) and (17) as

$$p_l - p_\infty = \Delta p - \frac{1}{2}\rho_g U_g^2 (1 - 4\sin^2\alpha) \tag{18}$$

Here the cross section of liquid column is assumed to be not deformed in the initial section of the liquid jet flow, because the aerodynamic force just initially acts on

the column and needs time to deform the column against the viscous force and surface tension. Actually in the experiments (Wu et al., 1997, 1998), it can also be seen that the cross section did not deform obviously at the near field of the nozzle exit. The resultant force of the pressure difference and surface tension generates the acceleration on the column. Mazallon et al. (1999) pointed out that the surface waves which associated with R-T instability involved a local phenomenon that was not affected by the dimensions of the liquid column itself. So we defined an effective thickness, h, which is the response thickness for the aerodynamic acceleration and could be less than the jet radius, i.e.,

$$\frac{1}{2}\rho_g U_g^2(1-4\sin^2\alpha) = \rho_l g(\alpha) h \tag{19}$$

where $g(\alpha)$ is the acceleration induced by the aerodynamic force, and should be a function of circumferential angle. The same phenomenon happens when wind blows vertically on an open air swimming pool and then an acceleration and surface wave will present. This acceleration is affected by a certain depth rather than the whole pool water. It is also similar to when a helicopter is flying above the lake or ocean. If the aerodynamic force induced by the propeller acts on the whole depth, there is nearly no acceleration and no surface waves, which is not consistent with the reality. So the assumption that aerodynamic acceleration acts on a certain thickness for the initial part of the jet is reasonable.

By substituting the instantaneous quantities into the dynamic boundary condition, one obtains the boundary condition of the disturbance in the form

$$(p_l' - p_g') - \Delta p' = \rho_l g(\alpha)\eta \tag{20}$$

Instantaneous surface tension induced by the disturbance on the interface $r = a + \eta(\theta, z, t)$ is expressed as (Yang, 1992)

$$\triangle p' = -\sigma\left\{\frac{1}{a^2}\left[1 - m^2 - (ka)^2\right]\eta\right\} \tag{21}$$

where σ is the liquid surface tension. Through the boundary conditions (14), (15), (20) and the time-dependent Bernoulli condition, the constants η_0, A, and B can be eliminated and the dispersion equation is obtained,

$$\begin{aligned}&\frac{k\rho_g U_g^2(1-4\sin^2\alpha)}{2h} - \sigma k\left\{\frac{1}{a^2}\left[1-m^2-(ka)^2\right]\right\} - \left[\rho_l(U_l k)^2\frac{I_m(ka)}{I_m'(ka)}\right.\\ &\left. - \rho_g\left(\frac{4mU_g}{a}\sin\alpha\right)^2\frac{K_m(ka)}{K_m'(ka)}\right] + 2i\left[\rho_l U_l k\frac{I_m(ka)}{I_m'(ka)} + \rho_g\frac{2mU_g}{a}\sin\alpha\frac{K_m(ka)}{K_m'(ka)}\right]\omega\\ &+\left[\rho_l\frac{I_m(ka)}{I_m'(ka)} - \rho_g\frac{K_m(ka)}{K_m'(ka)}\right]\omega^2 = 0\end{aligned} \tag{22}$$

where $I'_m(ka)$ and $K'_m(ka)$ are the derivative of $I_m(ka)$ and $K_m(ka)$, respectively.

Letting $U_g = 0$, the dispersion equation can be reduced to the form derived by Yang (1992). If gas density ρ_g and velocity U_g are set to zero, it reduces to the equation of Rayleigh (1878). By ensuring that Eq. (22) can be reduced to the typical dispersion equations of a round liquid jet into a quiescent gas, the current dispersion equation is verified.

3. RESULTS AND DISCUSSION

The dispersion Eq. (22) has a pair of conjugate roots for the complex frequency ω. A special interest is taken in the real part ω_R which represents the growth rate of disturbances.

$$\omega_R^2 = \underbrace{\frac{\left[(kU_l)^2 I_m + \frac{\rho_g}{\rho_l}\left(\frac{4mU_g}{a}\sin\alpha\right)^2 K_m\right]}{\left[I_m - \frac{\rho_g}{\rho_l}K_m\right]} - \frac{\left[kU_l I_m + \frac{2m\rho_g U_g}{\rho_l}\sin\alpha K_m\right]^2}{\left[I_m - \frac{\rho_g}{\rho_l}K_m\right]^2}}_{A1} \tag{23}$$

$$+ \underbrace{\frac{\frac{\sigma k}{\rho_l a^2}\left[1 - m^2 - (ka)^2\right]}{\left[I_m - \frac{\rho_g}{\rho_l}K_m\right]}}_{A2} + \underbrace{\frac{k\frac{\rho_g U_g^2}{\rho_l}\frac{|1 - 4\sin^2\alpha|}{2h}}{\left[I_m - \frac{\rho_g}{\rho_l}K_m\right]}}_{A3}$$

where $I_m = I_m(ka)/I'_m(ka)$, $K_m(ka)/K'_m(ka)$.

It can be seen from Eq. (23) that the disturbance growth rate is influenced by the parameters involved, wave number ka, gas velocity U_g, liquid jet velocity U_l, effective thickness h, and circumferential angle α, circumferential wave number m. As marked in the equation, the growth rate consists of three terms, $A1$, $A2$, and $A3$, which are induced by jet velocities, liquid surface tension, and aerodynamic acceleration respectively. Especially, $A3$ is the growth rate of the R-T wave on the liquid column. The aerodynamic acceleration is an absolute value, because the term $(1 - 4\sin^2\alpha)$ is negative when R-T instability is induced by a heavy fluid penetrating through a light fluid. Equation (23) can be written in terms of dimensionless variables as

$$\frac{\omega_R^2}{U_l^2/a^2} = \underbrace{\frac{[(ka)^2 I_m + Q(4m\Gamma\sin\alpha)^2 K_m]}{[I_m - QK_m]} - \frac{kaI_m + 2Qm\Gamma\sin\alpha K_m}{[I_m - QK_m]^2}}_{A1} + \underbrace{\frac{\frac{ka}{\mathrm{We}_l}[1 - m^2 - (ka)^2]}{[I_m - QK_m]}}_{A2} + \underbrace{\frac{\frac{\mathrm{We}_g}{\mathrm{We}_l}\frac{ka|1 - 4\sin^2\alpha|}{2h/a}}{[I_m - QK_m]}}_{A3} \tag{24}$$

where the dimensionless parameters are defined as $Q = \rho_g/\rho_l$, $\Gamma = U_g/U_l$, $\mathrm{We}_g = \rho_g U_g^2 a/\sigma$, $\mathrm{We}_l = \rho_l U_l^2 a/\sigma$.

When $\mathrm{We}_g = 0$, Eq. (24) is the same as the solution of dispersion equation derived by Yang (1992). The upwind axial surface waves ($\alpha = 0, m = 0$) are most evident in the experiments by Wu et al. (1997, 1998).

Equation (24) is a monotonic increasing function of We_g when $\alpha = 0$ and $m = 0$. If the contribution of jet velocity to ω_R^2 is neglected, the disturbance growth rate is only related to the gas Weber number. Equation (24) reduces to

$$\omega_R^2 = \frac{\frac{k\sigma}{\rho_l a^2}[1 - (ka)^2] + \frac{\rho_g U_g^2}{\rho_l}\frac{k}{2h}}{[I_0 - QK_0]} \tag{25}$$

Actually, due to the properties of the Bessel function, when $ka \to \infty$, $I_m \to 1$, and $A1$ will equal zero. In general, for a liquid jet in gaseous crossflow, $\rho_l \gg \rho_g$. Then,

$$\omega_R^2 = \frac{\rho_g U_g^2}{\rho_l}\frac{k}{2h} - \frac{k^3\sigma}{\rho_l} \tag{26}$$

This equation is a little different from the result of Ng et al. (2008), because of different analysis of aerodynamic acceleration. The optimum wavelength, corresponding to the maximum growth rate, is calculated through Eq. (26) as

$$\frac{\lambda_{opt}}{a} = 2\sqrt{6}\pi\left(\frac{h}{a}\right)^{0.5}\mathrm{We}_g^{-0.5} \tag{27}$$

It should be noted that the characteristic length in Weber number is the jet radius instead of diameter. This optimum wavelength for $h = a/8$ is plotted in Fig. 2 with several available correlations which are experimentally studied by Mazallon et al. (1999) and Sallam et al. (2004). It can be seen that the present prediction with $h = a/8$ is well consistent with Sallam's correlation. All those correlations refer to the upwind surface waves, corresponding to the circumferential angle $\alpha = 0$. The aerodynamic force is considered to be converted into aerodynamic acceleration completely. However, actually, the viscous force of the liquid and the gas compression would dissipate a part of

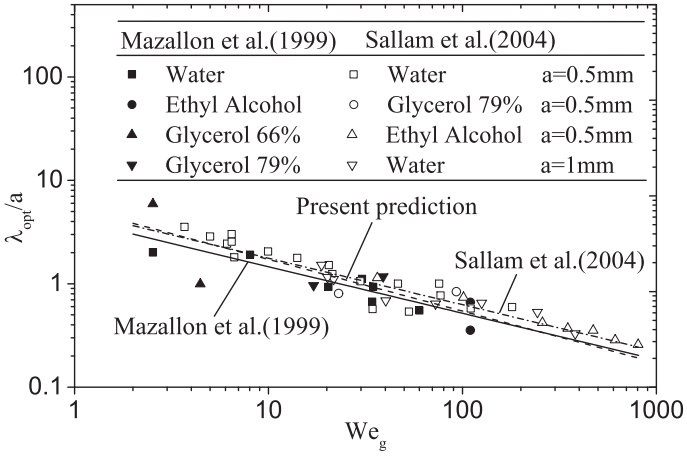

FIG. 2: Comparison of the optimum wave length among predictions of the present model and some available experimental results

aerodynamic force. Thus the effective thickness should be smaller than $a/8$. This will contribute to generate and propagate waves with smaller wavelength along the jet, and then enhance the performance of the jet breakup.

In the next section, effects of gas Weber number, and liquid Weber number on the upwind side will be discussed, respectively. Here, the liquid and gas are taken as water and air. The relevant parameters are listed in Table 1.

3.1 The Effect of We_g

Equation (24) shows that gas Weber number has influence only on term $A3$, and for the surface wave, the effective thickness h is set to be $a/8$ as mentioned above. Plotted in Fig. 3 is the dimensionless growth rate versus wave number at different gas Weber numbers. The triangle symbols represent the maximum growth rate. It can be seen that for We_g = 0, the most unstable wave number is approximately 0.76, which is larger than the Rayleigh analysis, 0.697. That is because the gas phase is taken into consideration

TABLE 1: Summary of relevant parameters

Gas density (air) (kg · m^{-3})	1.18
Liquid density (water) (kg · m^{-3})	995
Jet diameter (mm)	0.5
Surface tension (water) (N · m^{-1})	0.0708
Jet velocity (m · s^{-1})	5

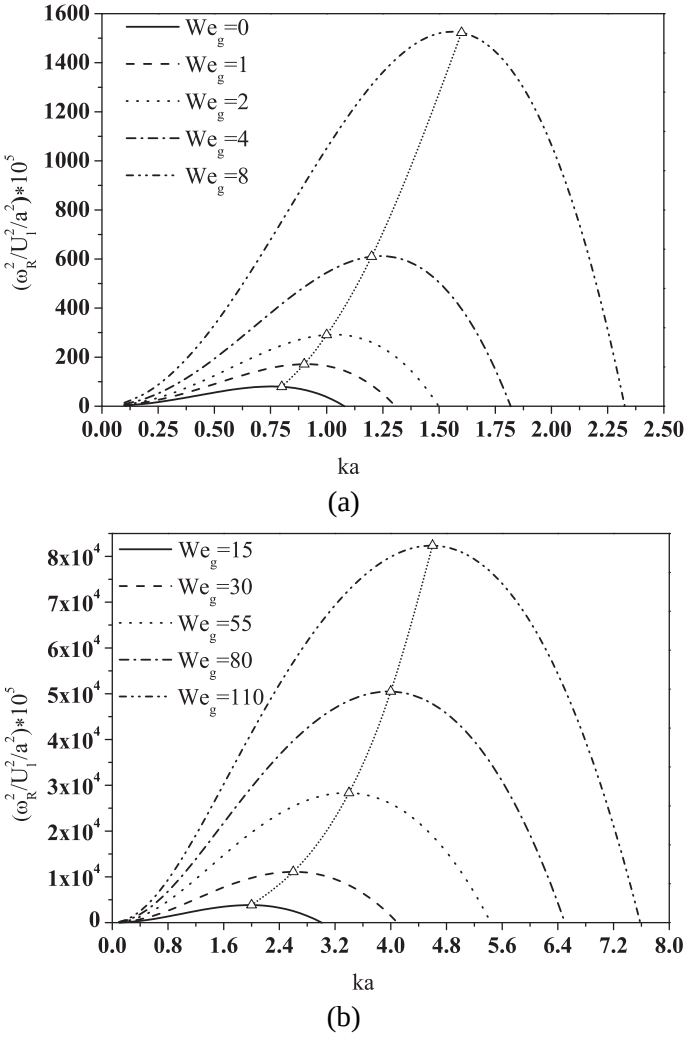

FIG. 3: Variation of growth rate with wave number, We_l = 176; (a) $We_g \leq 8$, (b) $We_g \geq 15$

in the present analysis while it is not included in Rayleigh theory. Obviously, as the gas velocity increases, the range of unstable axial wave number and the corresponding growth rate increase significantly. It can also be observed in Fig. 4 for higher gas Weber number. As We_g varies from 0 to 110, the upper limit of unstable axial wave number increases from 1.3 to 21.1. This denotes that aerodynamic force can increase the jet instability and accelerate the growth of disturbance.

The flow at the wave number with maximum growth rate is most unstable and this wave number is referred to as the optimum wave number. The optimum wavelength is

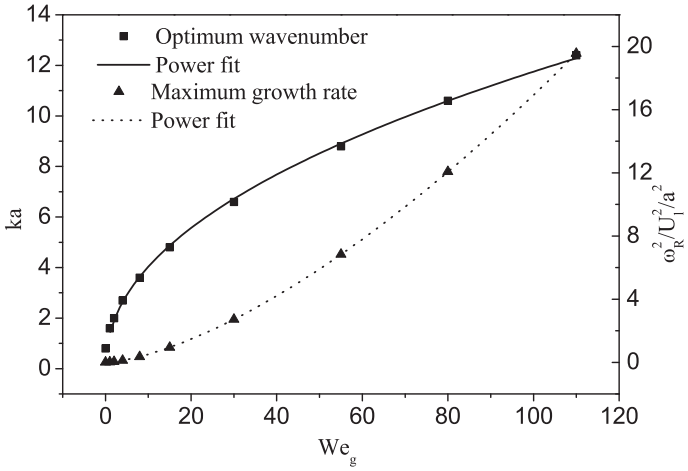

FIG. 4: Variation of optimum wave number and corresponding maximum growth rate with gas Weber number, We_l = 176

the dominant role of the corresponding surface waves and has an important effect on the jet breakup process (Panchagnula et al., 1996; Sallam et al., 2004). The optimum wave number and the corresponding dimensionless maximum growth rate plotted in Fig. 4 progressively increase with increasing the gas Weber number at We_l = 176. It is implied that the larger the air crossflow velocity, the smaller is the wavelength of the dominant surface wave on the liquid column. This result is consistent with experimental observations by Wu et al. (1997), Mazallon et al. (1999), and Sallam et al. (2004). In the range of 0–30 for gas Weber number, the optimum wavelength decreases quickly compared with the rise of the maximum growth rate. Instead, the maximum growth rate increases dramatically for large We_g. Here, the characteristic length in Weber number is the jet radius instead of diameter.

Obviously, the optimum wave number and the maximum growth rate are approximate as power functions of gas Weber number. The best correlations are

$$(ka)_{\text{opt}} = 1.38\text{We}_g^{0.46} \tag{28}$$

$$[\omega_R^2/(U_l/a^2)]_{\max} = 1.56 \times 10^{-2}\text{We}_g^{1.52} \tag{29}$$

The correlation coefficients of the fits are both 0.99.

3.2 The Effect of We_l

The liquid Weber number, i.e., liquid jet velocity seen in Eq. (23) also has an important influence on the wave growth rate. Figure 5 plots the variation of growth rate with

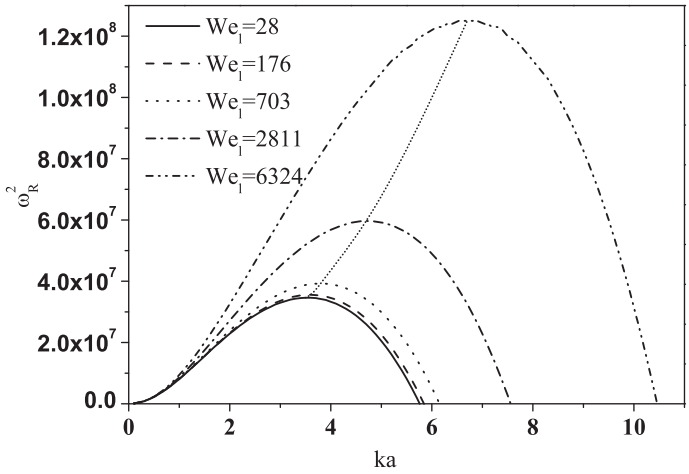

FIG. 5: Variation of growth rate with wave number, We$_g$ = 8

wave number at different liquid Weber numbers. The gas Weber number is set to 8 and the effective thickness is $h/8$ according to the above section. The other parameters are the same as in Table 1 except the jet velocity. Similar to the effect of We$_g$, the ranges of unstable axial wave number and the growth rate increase as liquid Weber number increases. The optimum wavelength which decreases with the increase of liquid Weber number is plotted in Fig. 6, and it decreases slowly at large We$_l$. It means the wavelength will reach the minimum value rather than decrease monotonically as the liquid Weber number increases.

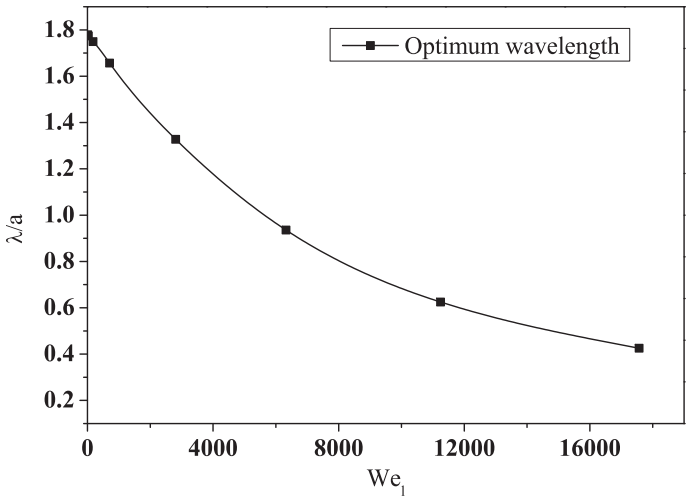

FIG. 6: Variation of the optimum wavelength with liquid Weber number, We$_g$ = 8

To quantify the growth rate separately caused by We_l and We_g, namely by jet velocity and gas velocity, respectively, term $A1$ and term $A3$ in Eq. (23) versus wave number for different gas and liquid Weber numbers are plotted in Fig. 7. The vertical coordinate ω_R^2 represents the quantity of $A1$ and $A3$. Figure 7 shows that $A3$ is the primary contribution to the growth rate of small wave number $(ka < 3)$ and $A1$ principally contributes to the growth rate at large wave number. So the surface wave with large wavelength is under the control of transverse aerodynamic force and liquid surface tension. The optimum wave number characterizes the fastest growing (or most probable) waves on the liquid surface which are thought to be eventually responsible for the breakup as can be seen. When the line of $A1$ intersects the line of $A3$ ($A1$ is equal to $A3$) just at the optimum wavenumber, this is the critical value and can be represented by the ratio We_l/We_g which is as same as the momentum ratio $q = \rho_l U_l^2/\rho_g U_g^2$. When $We_l < 2811$, $A1$ corresponding to the optimum wave numbers are far less than $A3$. This implies that the dominant waves are mainly affected by the aerodynamic force and surface tension in this condition. As the jet velocity increases, the effect of liquid Weber number gradually increases. As can be seen in Fig. 8, when We_l = 4932 and We_g = 6, $A1$ approximately equals $A3$. The largest critical momentum ratio is q_{cr} = 732 at which the contribution of liquid jet velocity to the wave growth rate is the same as the aerodynamic force and the dominant wave is affected by all three terms in Eq. (23). When $q > q_{cr}$, the effect of liquid Weber number is more significant than that of gas Weber number. Only when $q < q_{cr}$, the optimum surface waves can be approximately calculated by Eq. (30). Similar to the critical momentum ratio which divides the regime of column waves and breakup processes in crossflow (Wu et al., 1997), q_{cr} is not a fixed value and it varies with We_g. Figure 9, which displays the variation of critical momentum ratio with the gas Weber number, indicates that the q_{cr} decreases as We_g increases. The best fit correlation of the critical momentum ratio is given by

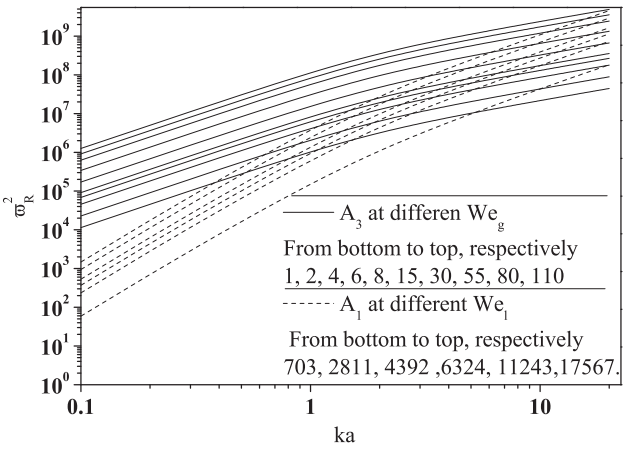

FIG. 7: Comparison of term $A1$ and term $A3$ in Eq. (23) with different We_g and We_l

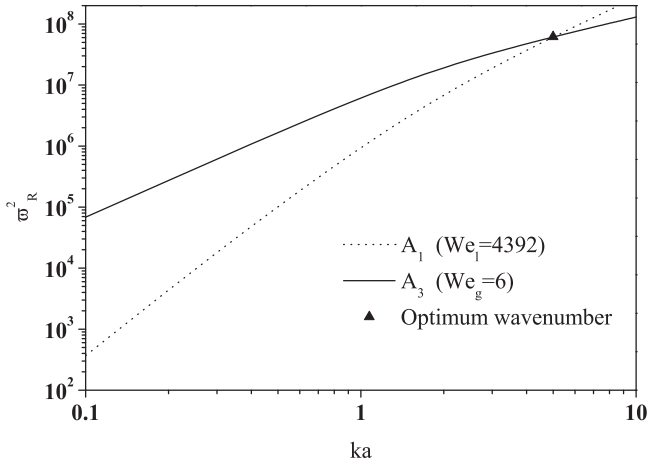

FIG. 8: The largest critical momentum ratio for term $A1$ and term $A3$ in Eq. (23)

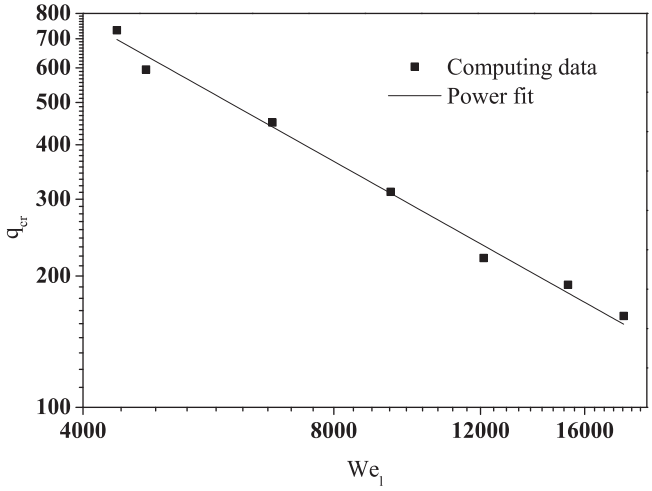

FIG. 9: Variation of critical momentum ratio with the gas Weber number

$$q_{cr} = 1821 \mathrm{We}_g^{-0.52} \tag{30}$$

The correlation coefficient of the fit is 0.99. Actually, q is less than q_{cr} in most of the experiments (Aalburg et al., 2004; Fuller et al., 1997; Mazallon et al., 1999; Sedarsky et al., 2010; Wu et al., 1997), because for high momentum ratio, the penetration of the jet is too large for the experimental test section. So the images of surface waves on the liquid column show R-T waves induced by aerodynamic force.

3.3 The Breakup Length Prediction

The breakup of a liquid jet in crossflow occurs when the dominant wave amplitude is equal to the jet radius at lower jet velocity (low liquid Weber number). This is the breakup length in the liquid flow direction. So the breakup length can be predicted by

$$L = U_l \ln(a/\eta_0)/\omega_R \tag{31}$$

Combining Eqs. (28) and (29), and setting effective thickness to $a/8$,

$$\begin{aligned} \frac{L}{a} &= \ln(a/\eta_0)\left(\frac{\sqrt[4]{27}}{4}\right)\left(\frac{\rho_l U_l^2}{\rho_g U_g^2}\right)^{0.5}\left(\frac{\sigma}{\rho_g U_g^2 a}\right)^{0.25} \\ &= \ln(a/\eta_0)\left(\frac{\sqrt[4]{27}}{4}\right)\left(\frac{q^{0.5}}{\mathrm{We}_g^{0.25}}\right) \end{aligned} \tag{32}$$

For low-speed jets, the parameter $ln(a/\eta_0)$ has been determined roughly to be 12 from experiments (Lin and Reitz, 1998). Thus,

$$\frac{L}{a} = 6.84\left(\frac{q^{0.5}}{\mathrm{We}_g^{0.25}}\right) \tag{33}$$

Wu et al. (1997) gave the transverse height of the column fracture point as

$$\frac{L}{a} = 6.88q^{0.5} \tag{34}$$

It can be seen that the effect of gas Weber number is taken into consideration in Eq. (33). With lower gas and liquid Weber numbers, Eq. (33) agrees with the correlation (34) well. However, for higher gas and liquid velocities, the prediction (33) may not be accurate because the parameter $ln(a/\eta_0)$ = 12 is only corresponding to the low-speed jets (Fu et al., 2010; Lin and Reitz, 1998). This discrepancy may also be attributed to the breakup regime for high-speed crossflow, like bag and shear breakup. Thus the breakup length does not only depend on the surface waves.

4. CONCLUSION

The linear instability (especially R-T instability) model of a round inviscid liquid jet in a gaseous crossflow was presented. The fluids were assumed to be incompressible and inviscid. The deflection of the liquid column in the streamwise direction of the gaseous crossflow and the cross-section deformation of liquid jet were neglected. The dispersion equation has been derived with the instability analysis and verified. It was found that the instability of a liquid jet in a gaseous crossflow is dominated by three terms which are

separately caused by jet velocity, surface tension, and aerodynamic force. Neglecting the effect of the jet velocity, the axial optimum wavelength on the upwind side is a power function of gas Weber number with the parameter effective thickness and coincides with the experimental results. The effect of liquid Weber number is similar to the gas Weber number. Increasing liquid Weber number will increase the instability and decrease the optimum wavelength. The model predictions also show that the aerodynamic force is the primary contribution to the growth rate of small wave number ($ka < 3$) and jet velocity principally contributes to the growth rate at large wave number. The critical momentum ratio at which the contribution of liquid jet velocity to the maximum growth rate is as large as that of the aerodynamic force decreases with the increase of gas Weber number. The largest critical momentum ratio is q_{cr} = 732. The jet breakup length in the longitudinal direction can be predicted as a function of momentum ratio and gas Weber number, and it agrees well with experimental correlation for lower gas and liquid Weber numbers. Finally, more experiments are needed to verify the model predictions.

REFERENCES

Aalburg, C., Sallam, K. A., and Faeth, G. M., Properties of nonturbulent round liquid jets in uniform crossflows, *AIAA Aerospace Sciences Meeting and Exhibit*, Nevada, 2004.

Ali, M. and Islam, A. K. M. S., Study on main flow and fuel injector configurations for scramjet applications, *Int. J. Heat Mass Transfer*, vol. **49**, pp. 3634–3644, 2006.

Becker, J. and Hassa, C., Breakup and atomization of a kerosene jet in crossflow at elevated pressure, *Atomization Sprays*, vol. **11**, pp. 49–67, 2002.

Boronin, S. A., Healey, J. J., and Sazhin, S. S., Non-modal stability of round viscous jets, *J. Fluid Mech.*, vol. **716**, pp. 96–119, 2013.

Fu, Q. F., Yang, L. J., Qu, Y. Y., and Gu, B., Linear stability analysis of a conical liquid sheet, *J. Propuls. Power*, vol. **26**, pp. 955–968, 2010.

Fuller, R. P., Wu, P. K., Kirkendall, K. A., and Nejad, A. S., Effects of injection angle on column breakup processes of liquid fuel jets in subsonic crossflows, *AIAA Paper 1997-2966*, 1997.

Heister, S. D., Nguyen, T. T., and Karagozian, A. R., Modeling of liquid jets injected transversely into a supersonic crossflow, *AIAA J.*, vol. **27**, pp. 1727–1734, 1988.

Inamura, T., Trajectory of a liquid jet traversing subsonic airstreams, *J. Propuls. Power*, vol. **16**, pp. 155–157, 1999.

Karagozian, A. R., Transverse jets and their control, *Prog. Energy Combust. Sci.*, vol. **36**, pp. 531–553, 2010.

Kolpin, M. A. and Horn, K. P., Study of penetration of a liquid injectant into a supersonic flow, *AIAA J.*, vol. **6**, pp. 853–858, 1968.

Kush, E. A. J. and Schetz, J. A., Liquid jet injection into a supersonic flow, *AIAA Paper 1972-1180*, 1972.

Lin, S. P. and Lian, Z. W., Mechanisms of the breakup of liquid jets, *AIAA J.*, vol. **50**, pp. 120–126, 1988.

Lin, S. P. and Reitz, R. D., Drop and spray formation from a liquid jet, *Annu. Rev. Fluid Mech.*, vol. **30**, pp. 85–105, 1998.

Lovett, J. A., Brogan, T. P., Philippona, D. S., Keil, B. V., and Thompson, T. V., Development needs for advanced afterburner designs, *40th AIAA/ASME/SAE/ASEE Joint Propulsion Conference and Exhibit*, Florida, 2004.

Mashayek, A., Jafari, A., and Ashgriz, N., Improved model for the penetration of liquid jets in subsonic crossflows, *AIAA J.*, vol. **46**, pp. 2674–2685, 2008.

Mazallon, J., Dai, Z., and Faeth, G. M., Aerodynamic primary breakup at the surface of nonturbulent round liquid jets in crossflow, *Atomization Sprays*, vol. **9**, pp. 291–311, 1999.

Nejad, A. S., Schetz, J. A., and Jakubowski, A. K., Mean droplet diameter resulting from atomization of a transverse liquid jet in a supersonic airstream, *AIAA Paper 1980-0899*, 1980.

Ng, C. L., Sankarakrishinan, R., and Sallam, K. A., Bag breakup of nonturbulent liquid jets in crossflow, *Int. J. Multiphase Flow*, vol. **34**, pp. 241–259, 2008.

Panchagnula, M. V., Sojka, P. E., and Santanglo, P. J., On the three-dimensional instability of a swirling, annular, inviscid liquid sheet subject to unequal gas velocities, *Phys. Fluids*, vol. **8**, pp. 3300–3312, 1996.

Pandey, K. M. and Sivasakthivel, T., Recent advances in scramjet fuel injection c A review, *Int. J. Chem. Eng. Appl.*, vol. **1**, pp. 294–301, 2010.

Rayleigh, L., On the instability of jets, *Proc. of the London Math. Soc.*, vol. **10**, pp. 4–13, 1878.

Reichenbach, R. E. and Horn, K. A., Investigation of injectant properties on jet penetration in a supersonic stream, *AIAA J.*, vol. **9**, pp. 469–472, 1971.

Reitz, R. D. and Bracco, F. V., Mechanism of atomization of a liquid jet, *Phys. Fluids*, vol. **25**, pp. 1730–1742, 1982.

Sallam, K. A., Aalburg, C., and Faeth, G. M., Breakup of round nonturbulent liquid jets in gaseous crossflow, *AIAA J.*, vol. **42**, pp. 2529–2540, 2004.

Schetz, J. A., Kush, E. A., and Joshi, P. B., Wave phenomena in liquid jet breakup in a supersonic crossflow, *AIAA J.*, vol. **18**, pp. 774–778, 1980.

Sedarsky, D., Paciaroni, M., Berrocal, E., Petterson, P., Zelina, J., Gord, J., and Linne, M., Model validation image data for breakup of a liquid jet in crossflow: Part I, *Exp. Fluids*, vol. **49**, pp. 391–408, 2010.

Shen, J. and Li, X., Instability of an annular viscous liquid jet, *Acta Mechanica*, vol. **114**, pp. 167–183, 1996.

Stenzler, J. N., Lee, J. G., and Santavicca, D. A., Penetration of liquid jets in a cross-flow, *Atomization Sprays*, vol. **11**, pp. 887–906, 2006.

Sterling, A. M. and Sleicher, C. A., The instability of capillary jets, *J. Fluid Mech.*, vol. **68**, pp. 477–495, 1975.

Wang, Q., Mondragon, U. M., Browm, C. T., and McDonell, V. G., Characterization of trajectory, break point, and break point dynamics of a plain liquid jet in a crossflow, *Atomization Sprays*, vol. **21**, pp. 203–219, 2011.

Wang, X. H., Huang, Y., Wang, S. L., and Liu, Z. L., Bag breakup of turbulent liquid jets in crossflow, *AIAA J.*, vol. **50**, pp. 1360–1366, 2012.

Wu, P. K., Kirkendall, K. A., Fuller, R. P., Gruber, M. R., and Nejad, A. S., Spray trajectories of liquid fuel jets in subsonic crossflows, *Int. J. Fluid Mech. Res.*, vol. **24**, pp. 128–137, 1997.

Wu, P. K., Kirkendall, K. A., Fuller, R. P., and Nejad, A. S., Spray structures of liquid jets atomization subsonic crossflows, *J. Propuls. Power*, vol. **14**, pp. 173–182, 1998.

Yang, H. Q., Asymmetric instability of a liquid jet, *Phys. Fluids*, vol. **4**, pp. 681–689, 1992.

Yang, L. J., Liu, Y. X., and Fu, Q. F., Linear stability analysis of an electrified viscoelastic liquid jet, *J. Fluids Eng.*, vol. **134**, paper 071303, 2012.

Young, D. F., Munson, B. R., and Okiishi, T. H., *A Brief Introduction to Fluid Mechanics*, New York: John Wiley Sons, 2001.

Zheng, Y. H. and Marshall, A. W., Characterization of the initial spray from low-weber-number jets in crossflow, *Atomization Sprays*, vol. **21**, pp. 575–589, 2011.

Zhu, Y., Huang, Y., Wang, F., and Wang, X. H., Experiment on breakup processes and surface waves of round liquid jets in crossflows, In *Proc. of ASME Turbo Expo*, Glasgow, 2010.

Atomization and Sprays, 24 (1): 41–80 (2014)

DEVELOPMENT OF A NEW SPRAY/WALL INTERACTION MODEL FOR DIESEL SPRAY UNDER PCCI-ENGINE RELEVANT CONDITIONS

Yanzhi Zhang,[1] Ming Jia,[1,*] Hong Liu,[1] Maozhao Xie,[1] Tianyou Wang,[2] & Lei Zhou[3]

[1] *School of Energy and Power Engineering, Dalian University of Technology, P. R. China*

[2] *State Key Laboratory of Engines, Tianjin University, P. R. China*

[3] *Center for Combustion Energy, Tsinghua University, P. R. China*

[*] Address all correspondence to Ming Jia E-mail: jiaming@dlut.edu.cn

Original Manuscript Submitted: 07/24/2013; Final Draft Received: 09/30/2013

A new spray/wall interaction model was developed with special emphasis on the premixed charge compression ignition (PCCI) engine-relevant conditions, i.e., high injection pressure and intermediate-to-high backpressure. The new model distinguishes between dry wall and wetted wall for a description of the complicated spray/wall interaction process. The dry wall impingement regimes include deposition and splash, whereas the wetted wall regimes consist of stick, rebound, spread, and splash. The regime transition thresholds of splash are determined based on recent experimental observations, which can account for the wide ranges of conditions related to engines. By using an updated log-normal distribution function, the sizes of the secondary droplets are determined in the improved model, which is more suitable to describe the atomization process of the secondary droplets formed by splash. Moreover, the velocities of the secondary droplets are determined by a Nukiyama-Tanasawa distribution function derived from the experimental measurements, and the ejection angle of the secondary droplet is assumed to be in the interval (2°, 30°) uniformly, which is reasonable for high injection pressure. In order to validate the new spray/wall interaction model, comparisons of the predictions from the present model with the experimental measurements and predictions from a previous spray/wall interaction model were conducted. The results indicate that the numerical predictions from the new model illustrate better agreements with the experimental data than those of the previous model, especially in the case with high injection pressure under PCCI-engine relevant conditions.

KEY WORDS: *spray/wall interaction model, diesel spray, injection timing, PCCI engines*

1. INTRODUCTION

Diesel engines have been widely used in commercial vehicles all around the world due to their low fuel consumption, high efficiency, and good reliability. However, as more and more stringent regulations are being put forward, the conventional diesel engines suffer from high nitrogen oxides (NO_x) and particulate matter (PM) emissions. The combustion mode of premixed charge compression ignition (PCCI) engines has been focused on considerably with regard to diesel engines in recent years due to its capability of keeping relatively high efficiency and low emissions of NO_x and PM (Kokjohn et al., 2011; Yao et al., 2009).

In diesel PCCI engines, the fuel/air charge is well mixed prior to combustion. Early fuel injection is commonly used for achieving the premixed fuel/air mixture in the combustion chamber (Fang et al., 2007; Lee and Reitz, 2006; Okude et al., 2004). However, significant spray/wall impingement was produced in PCCI engines when an injector with a narrow spray cone and early-injection timing were employed (Kong et al., 2005) Diwakar and Singh (2009) investigated the importance of spray/bowl interaction in a direct-injection diesel engine with early-injection PCCI combustion mode. It was indicated that spray/bowl interaction in PCCI engines with early injection is extremely important, and start of injection (SOI) timing, spray cone angle, and piston bowl shape have significant influences on the emissions of PCCI engines. The spray/wall impingement promotes the mixture of fuel and air, but also leads to the formation of a wall fuel film on the piston. This results in a region where the fuel/air mixture is too rich for complete combustion, and consequently produces high levels of unburned hydrocarbons and PM emissions (Drake et al., 2003; Stevens and Steeper, 2001; Sandquist et al., 2000). The experiments from Siewert (2007) demonstrated that the fuel spray that misses the piston bowl surface has a close connection with the increases in smoke, HC and CO emissions, and a reduction of the engine's thermal efficiency. Therefore, a better understanding of the spray/wall interaction process, which includes the characteristics of the secondary droplets formed by splash and the wall film resulting from the spray/wall impingement, will be helpful in the design of injection and combustion systems to improve engine performance and reduce engine emissions.

The phenomena of spray/wall interaction under conditions of real engines are difficult to describe due to the complicated in-cylinder flow, injection, and combustion processes. Thus fundamental studies were usually performed at simplified flow configurations to qualitatively investigate the spray/wall interaction process. For example, Katsura et al. (1989) experimentally observed the influences of the injection pressure, the distance between the injector and wall, the ambient gas pressure, and temperature on the characteristics of the impinged spray in a constant volume combustion chamber. In general, it is difficult to measure the characteristics of the secondary droplets near the wall region, such as the sizes and velocities of the secondary droplets resulting from splash. Alternatively, computational modeling offers a promising approach to obtain detailed

information about the spray/wall interaction, especially under the complicated engine-relevant conditions.

A few spray/wall interaction models have been developed in the last 30 years, which mostly used the impingement of individual droplets to describe the behavior of the impinged spray, despite the fact that a summation of individual droplets could not represent a spray exactly (Roisman et al., 2002; Roisman et al., 2006). Moreira et al. (2010) offered an important review of the experimental and numerical investigations of the spray/wall interaction under engine-relevant conditions recently, giving a systematic summarization of the current investigation of the impingement of a single droplet and spray. They indicated that the reason why the impingement of an individual droplet cannot accurately describe the behavior of the impinged spray is mostly due to the complex drop/drop interactions in sprays being neglected. Several issues still need to be solved in further investigations, which include the transition criterion between deposition and splash, the multiple drop interactions, and the effects of the film on the mechanisms and characteristics of secondary droplets resulting from splash, etc. Naber and Reitz (1988) made the first efforts to model the spray/wall interaction by identifying three different regimes, i.e., stick, reflect, and jet. In the stick regime, the impinged droplets stick on the wall; in the rebound regime, the impinged droplets are reflected elastically; and in the jet regime, it is assumed that the impinged droplets move tangentially along the wall surface and the velocity magnitudes are unchanged compared to the impinging droplets. There are several drawbacks existing in the model developed by Naber and Reitz (1988). The first one is the splash regime is ignored, which plays an important role in the atomization and vaporization of the impinged spray. The second one is that the model does not consider the loss of energy and momentum of the impinged droplets. Moreover, the threshold of different regimes in the model is based on observations of the experiment by Wachters and Westerling (1966), by impinging a liquid drop on a hot wall whose temperature is higher than the Leidenfrost temperature of the fuel. Thus the criteria may not be suitable for engine-relevant conditions, with the surface temperature of the bowl being below the boiling temperature of the fuel.

Senda et al. (1994) developed a spray/wall interaction model based on experimental results. The model distinguished between cold wall and hot wall with the consideration of liquid saturation temperature. Furthermore, Senda et al. (1997, 2000) improved the spray/wall interaction model by taking account of the effect of a preformed wall film on the film formation process. The improved model divided the impingement into low-energy impingement and high-energy impingement, and the criterion of the two kinds of impingement is Weber number of the incident droplet. For the case of low-energy impingement (i.e., $We < 300$), the expression describing the characteristics of the secondary droplets formed by splash are based on the dimensionless film thickness and the constraint of the energy conservation. For the case of high-energy impingement (i.e., $We > 300$), the model includes both the regimes of deposition and splash.

O'Rourke and Amsden (2000) proposed a spray/wall interaction model (subsequently referred to as the OA model) based on two experimental studies from Yarin and Weiss (1995) and Mundo et al. (1995) with consideration of energy conservation. Two regimes of deposition and splash are considered in the model, and the threshold of the two regimes accounts for the effect of the film thickness. The direction of the tangential velocities of the secondary droplets is statistically chosen from the distribution according to the work of Naber and Reitz (1988).

Bai et al. (2002) developed another spray/wall interaction model (referred to as the BG model) on the basis of the experimental results and conservation laws for determination of the impingement regimes, transition criteria, and droplet characteristics after impingement. The model considers the wall conditions of dry wall and wetted wall, and uses the Weber number as the transition criterion among the different regimes. In the case of dry wall, there are three regimes including stick, spread, and splash, whereas the regimes of rebound, spread, and splash are considered in the wetted wall case. Based on the experimental observations, the ejection angle of the secondary droplets uniformly distributes in the range of $5 \sim 50^{\circ}$. Nevertheless, Allocca et al. (2006) indicated that the OA model produced an unrealistic spray shape, and the BG model overestimated the height of the impinged spray for the cases of high injection pressures, which are typical operating conditions for diesel engines.

The aim of this paper is to develop a new spray/wall interaction model for impinged spray on a wall whose temperature is below the boiling temperature of the fuel under PCCI-engine relevant conditions, characterizing high injection pressure and intermediate-to-high backpressure. First, numerical simulations were performed to validate the new model, and the predictions simulated with the new model are compared with the experimental measurements and the calculated results using the OA model. Then multidimensional simulation coupled with the new spray/wall interaction model was applied to predict the combustion and emissions characteristics of PCCI engines with various injection timings. The influence of injection timing on the mixture preparation process for the diesel PCCI engine was also investigated.

2. MODEL FORMULATION

Spray impingement is an extremely complicated process which is influenced by many factors, such as the velocity, size, and temperature of the incident droplet; the viscosity and surface tension of the fluid; the temperature and roughness of the impinged wall; as well as the wall film thickness and gas boundary conditions (if present). In order to fully describe the process of spray/wall interaction, some important issues are refined in this study, including the types of impingement regimes, the transition criterion from one regime to another, and the postimpingement characteristics.

2.1 Impingement Regimes and Transition Criteria

The impingement regimes are generally affected by the properties of incident droplets and the impinged wall conditions (wall roughness, temperature, and film thickness). A general description of the impingement regimes for the conditions of a dry heated wall is proposed by Bai and Gosman (1995), which is identified by the Weber number of the impinged droplet and wall temperature as shown in Fig. 1.

In Fig. 1, T_B is the liquid boiling temperature, T_{PA} is the liquid pure adhesion temperature below which adhesion occurs at low impact energy, T_N is the liquid Nakayama temperature at which a droplet reaches its maximum evaporation rate, T_{PR} is the liquid pure rebound temperature above which bounce occurs at low impact energy, T_{Leid} is the Leidenfrost temperature, and T_w is the wall temperature. It can be seen that the Weber number of the droplet and the wall temperature shows the major influences on the outcomes of droplet/wall interaction. Several characteristic temperatures are applied to identify the different regimes with the following relations:

$$T_B < T_{PA} < T_N < T_{PR} < T_{Leid}$$

According to Kong (2007), under diesel-engine conditions, where the in-cylinder pressure already exceeds the critical pressure of the fuel droplet, it is unlikely that the surface temperature will exceed either the Leidenfrost temperature or the critical temperature. In

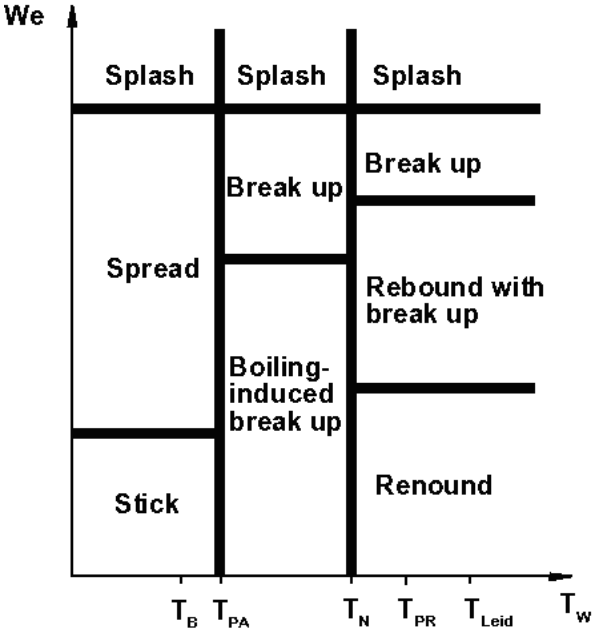

FIG. 1: Overall droplet impingement regimes and transition conditions for a dry heated wall from Bai and Gosman (1995).

other words, the wall surface temperature is less than the liquid boiling temperature and a wall film will be formed on the piston surface under diesel-engine relevant conditions. Thus the corresponding regimes of the impinged droplets are stick, rebound, spread, and splash. In consideration of dry wall and wetted wall, the following impingement regimes are used for the new spray/wall interaction model: deposition and splash for dry wall; stick, rebound, spread, and splash for wetted wall.

In order to determine which regime will occur in a certain condition, it is necessary to establish the transition criterion from one regime to another. The transition criteria are determined by several nondimensional numbers which include Weber number (We), Reynolds number (Re), Laplace number (La), Ohnesorge number (Oh), and capillary number (Ca), characterizing the relative magnitude of the forces acting to the impinging droplet.

2.1.1 Dry Wall

The transition criteria between the deposition and splash for the dry wall ($K_{dry,splash}$) used in this study is taken from the work of Cossali et al. (1997) for investigation of the impingement of a single droplet on a solid surface. This criterion is based on the curve-fit results which combine several previously published experimental data, which is defined as

$$K_{dry,splash} = 649 + 3.76R_{nd}^{-0.63} \tag{1}$$

where R_{nd} is the dimensionless surface roughness, which is defined as the ratio between the surface mean roughness (R) and the incident droplet diameter (d_b). Thus the criterion can account for the effect of surface roughness on the critical value between deposition and splash. The parameter K_{dry} is a nondimensional number, which is generally defined as the following form:

$$K_{dry} = A\,\mathrm{Oh}^a\mathrm{We}^b \tag{2}$$

where A, a, and b are empirical constants. Stow and Hadfield (1981) first introduced the parameter K_{dry}, which has been widely used in literature as the critical value for the onset of the splash regime. In the present study, $A = 1$, $a = -0.4$, and $b = 1$. Considering that $K_{dry,splash} = \mathrm{Oh}^{-0.4}\mathrm{We}$, Eq. (1) can be rewritten as

$$\mathrm{We}_{dry,splash} = \mathrm{Oh}^{0.4}(649 + 3.76R_{nd}^{-0.63}) \tag{3}$$

2.1.2 Wetted Wall

The transition criteria between stick to rebound and rebound to spread are taken from the work of Stanton and Rutland (1996), which is proposed based on the experimental investigations of Jayaratne and Mason (1964) and Rodriguez and Mesler (1985):

$$\begin{aligned} \mathrm{We}_{wet,stick} &= 5 \\ \mathrm{We}_{wet,rebound} &= 10 \end{aligned} \tag{4}$$

When the Weber number of an incident droplet exceeds the transition value between stick and rebound (i.e., $\mathrm{We}_n > \mathrm{We}_{wet,stick}$), the incident droplet will bounce off the film which was formed due to pre-existing impingement. Otherwise, the impinged droplet will stick on the wall in nearly a spherical form. When the Weber number of an incident droplet exceeds the transition value between rebound and spread (i.e., $\mathrm{We}_n > \mathrm{We}_{wet,rebound}$), the impinged droplet will merge with the liquid film upon impact; otherwise the incident droplet will rebound from the wall.

This criterion for spread to splash is proposed by Wang et al. (2002), who conducted systematic experiments using a single droplet to impact upon the wetted wall surface covering with different film thickness. The criterion is

$$\mathrm{We}_{wet,splash} = \begin{cases} 450 & \delta \le 0.1 \\ 1375.7\delta + 340 & 0.1 < \delta < 1.0 \\ 1043.8 + 232.6\delta^{-1} - 1094.4\delta^{-2} + 1576.4\delta^{-3} & \delta > 1.0 \end{cases} \quad (5)$$

where δ is the dimensionless film thickness, which is defined as the ratio between the mean film thickness (h) and the incident droplet diameter (d_b). It is assumed that when the droplets impact on the wetted wall, only film thickness affects the transition criteria and the effects of surface roughness are neglected.

2.2 Postimpingement Characteristics

After identifying the regimes of impingement, it is necessary to determine the postimpingement characteristics for the regimes. The following assumptions are employed in this study:

1. For stick regime, the impinged droplets adhere to the surface of the film in nearly a spherical form.

2. For deposition/spread, the impinged droplets are assumed to merge with the liquid film upon impact.

3. For rebound regime, the impinged droplets bounce off the film when the energy of incident droplet is low. The magnitude and direction of the rebound droplet velocity need to be determined in the rebound regime. The velocity of the droplet which bounces off the film is determined using Eq. (6) , which was obtained from the work of Bai and Gosman (1995) as

$$\begin{aligned} V_{at} &= \frac{5}{7} V_{bt} \\ V_{an} &= -e V_{bn} \end{aligned} \quad (6)$$

where V_{tb} and V_{bn} are the tangential velocity and normal velocity of the incident droplet, respectively, and V_{at} and V_{an} are the tangential velocity and normal velocity of the rebounded droplet, respectively. The quantity e is the coefficient of restitution, which is described by the following equation:

$$e = 0.993 - 1.76\alpha + 1.56\alpha^2 - 0.490\alpha^3 \tag{7}$$

where α is the incident angle of the impinged droplet and is measured from the wall surface.

4. For the splash regime, several important quantities need to be determined, including the mass ratio, which is defined as the ratio between the total ejected mass and the total injected mass (i.e., m_a/m_b), the diameter, ejection angle, and velocity of the secondary droplets. The secondary droplets are small droplets from the impingement site produced by splash. These quantities determined in the new spray/wall interaction model are given in the following sections in detail.

2.2.1 Mass Ratio for Splash Regime

Theoretical analysis and experimental results show that when splash occurs, a fraction of the impinged droplets will be ejected as secondary droplets and others will remain on the surface. When the incident droplet impacts on a wetted wall, it has been proved that the splashing droplets may entrain the liquid film, so the mass ratio will be larger than 1. However, detailed experimental information about the mass ratio is insufficient, despite that the mass ratio is believed to be affected by many factors, such as wall roughness and film thickness. Bai and Gosman (1995) proposed a correlation for the mass ratio under dry wall and wetted wall conditions in which the mass ratio distributes uniformly in its range according to the observations of the related experiments. Experimental data were also reported by Yarin and Weiss (1995), who studied the impingement of a train of droplets upon a solid surface. The experimental results from Yarin and Weiss (1995) are shown in Fig. 2.

According to the experimental observations from Yarin and Weiss (1995), the splash criterion is determined by $u = 18$, where u is the nondimensional impact velocity, which is expressed by $u = V_{bn}\,(\sigma/\rho)^{-1/4}\,(\mu/\rho)^{-1/8}\,f^{-3/8}$, and f is the impingement frequency. By substituting the impingement frequency $f = V_{bn}/d_d$ into $K = \mathrm{Oh}^{-0.4}\mathrm{We}$, the relation between K_{cr} and u could be obtained as $K_{cr} = u^{3.2}$. So the splash criterion of Yarin and Weiss can be converted to $K_{cr} = 10,396$. By fitting the experimental data from Yarin and Weiss (1995), a new correlation used to determine the mass ratio when the incident droplets impact upon a dry wall is constructed in the present study as

$$\gamma_m = \frac{m_a}{m_b} = 0.80\left\{1 - \exp\left[-3.17 \times 10^{-4}(K - K_{cr})\right]\right\}, \tag{8}$$

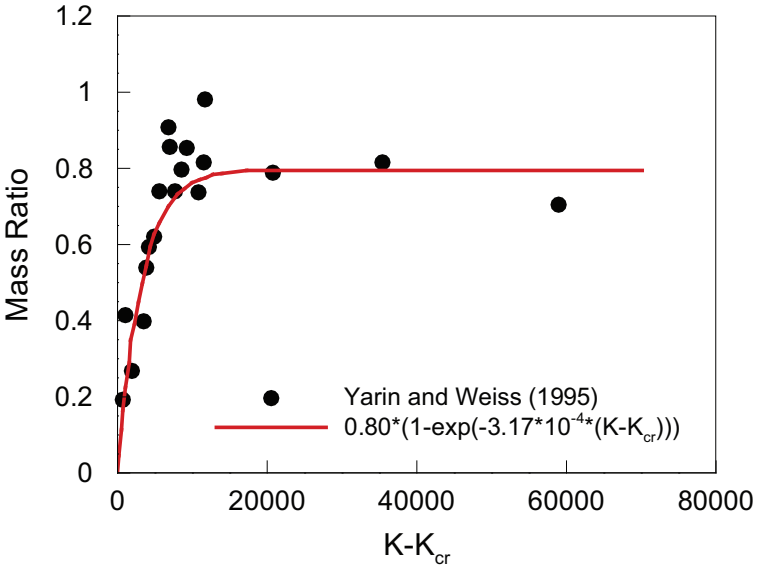

FIG. 2: Mass ratio of the secondary droplet.

where γ_m is the mass ratio; m_a and m_b are the mass of the incident droplet and the secondary droplet, respectively; and K is the criterion defined in Eq. (2). It can be seen from Fig. 2 that with the increase of $K - K_{cr}$, the mass ratio between the total secondary droplets and the incident droplets increases from zero to a value of about 0.80 rapidly and remains nearly constant from then on.

When the incident droplets impact upon a wetted wall, the mass ratio may be larger than 1, as mentioned previously. The mass ratio for a wetted wall used in this study can be determined by the work from Bai and Gosman (1995) as

$$\gamma_m = \frac{m_a}{m_b} = 0.2 + 0.9\varepsilon, \tag{9}$$

where ε is a random number distributed uniformly in the interval (0, 1). Thus, considering the wall conditions, the mass ratio can be summarized as

$$\gamma_m = \frac{m_a}{m_b} = \begin{cases} 0.80\left\{1 - \exp\left[-3.17 \times 10^{-4}(K - K_{cr})\right]\right\} & \text{for dry wall} \\ 0.2 + 0.9\varepsilon & \text{for wetted wall} \end{cases} \tag{10}$$

2.2.2 Secondary Droplet Diameter for Splash Regime

The experimental observations (Cossali et al., 1997; Mundo et al., 1995; Stow and Hadfield, 1981; Yarin and Weiss, 1995) indicated that when the wall is rough or wet, crown

splashing happens, with a crownlike sheet forming and propagating out of the impingement site. The droplet is transformed to a crown first and then the sheet disintegrates to form jets at the top of the crown, which further breaks up to produce much smaller secondary droplets. Experiments have found that the crown splashing produces the secondary droplets with various sizes, which can be well described by the log-normal distribution function (Levin and Hobbs, 1971; Samenfink et al., 1999; Stow and Stainer, 1977). This is because of the multiplicative nature of the log-normal distribution function, which may be similar to the characteristics of the atomization of the secondary droplets formed by splash. The general expression of the log-normal distribution function is

$$f(d_a) = \frac{1}{d_a \sigma \sqrt{2\pi}} \exp\left(-\frac{[\ln(d_a) - \ln(d_m)]^2}{2\sigma^2}\right) \tag{11}$$

where σ and d_m are the geometric standard deviation and the geometric mean diameter, respectively, which need to be determined. Wu (2003) determined the geometric mean diameter of the secondary droplets through a simplified physical analysis by relating to the dimensionless parameter K' as

$$\frac{d_m}{d_b} = 19.86K'^{-0.5} \tag{12}$$

where $K' = \mathrm{WeRe}^{0.5}$. The geometric standard deviation σ is determined by Wu (2003) using the principle of maximum rate of entropy production, which yields the geometric standard deviation with a constant with a value of $\sqrt{6}/6$. According to the work from Moreira et al. (2010), if there is only one mechanism of atomization of secondary droplets in the computation model, it is more likely that the variations of the geometric standard deviation become negligible. So it is believed that the constant geometric standard deviation used in this study is reliable. The log-normal distribution function of the secondary droplets according to Wu (2003) can be written as

$$f(d_a/d_b) = \frac{\sqrt{3}}{\sqrt{\pi}\,(d_a/d_b)} \exp\left\{-3\left[\ln\left(\frac{d_a}{d_b}\right) - \frac{1}{6} - \ln\left(\frac{d_m}{d_b}\right)\right]\right\} \tag{13}$$

By comparing the predictions from Eq. (13) with the existed experimental results (Mundo et al., 1995; Samenfink et al., 1999; Stow and Stainer, 1977), Wu (2003) found Eq. (13) predicts the sizes of secondary droplets quite well. However, when Eq. (12) is applied to the cases with high-energy impingement (i.e., diesel spray), which largely exceed the range of validity of Eq. (12), very small sizes of the secondary droplets are produced. Thus Eq. (12) is updated in this study as

$$\frac{d_m}{d_b} = \max\left(19.86K'^{-0.5}, 0.05\right) \tag{14}$$

The second argument in Eq. (14) is referenced from the experimental work of Yarin and Weiss (1995) and Mundo et al. (1995), who observed that the maximum d_a/d_b is not likely less than 0.06. In this study, it is reasonable to slightly lower this value to 0.05, which could better reproduce the sizes of the secondary droplets for the cases of high-energy impingement.

2.2.3 Secondary Droplet Velocities for Splash Regime

The information about the velocities of the secondary droplets is very limited. Mundo et al. (1995) reported a distribution for the secondary droplet velocities, which has been adopted in many models (O'Rourke and Amsden, 2000; Han et al., 2000; Stanton and Rutland, 1996). In order to develop a practical velocity model for the secondary droplets after splashing, several simplified assumptions are introduced in this study. According to Bai et al. (2002), a fundamental assumption is that the velocity fields of the secondary droplets, as the results of the oblique impingement, can be described as a superposition of those arising from a tangential splashing and a normal splashing. Tangential splashing only originates a tangential splashed velocity $\vec{V}_{at}$, which is related to the incident tangential velocity $\vec{V}_{bt}$, whereas normal splashing produces a splashed velocity $\vec{V}_{an}$, which is neither normal nor tangential. The total splashed velocity can be obtained by adding the two parts, yielding

$$\vec{V}_a = \vec{V}_{at} + \vec{V}_{an}. \tag{15}$$

Figure 3 gives a schematic diagram of the simplification of the velocity of the splashed droplet.

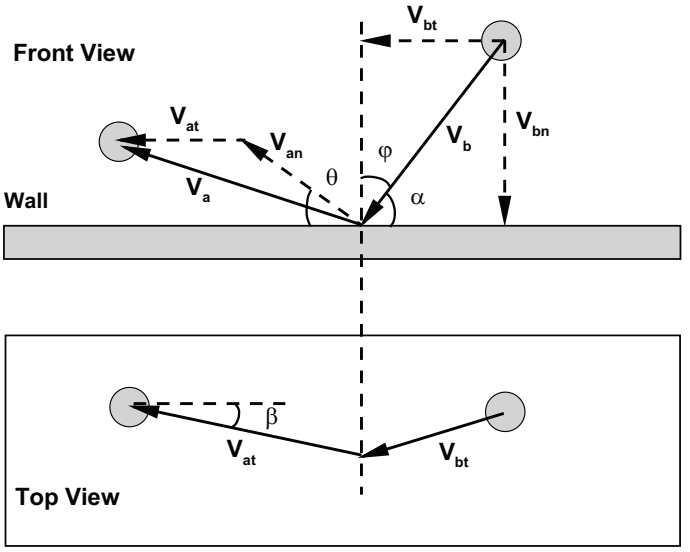

FIG. 3: Schematic diagram of the velocity of the splashed droplet.

After a normal splash, the magnitude of the vector $\vec{V}_{an}$ can be determined by a Nukiyama-Tanasawa distribution function as

$$f(V_{an}) = \frac{4}{\sqrt{\pi}} \frac{V_{an}^2}{V_{a,\max}^3} \exp\left[-\left(\frac{V_{an}}{V_{a,\max}} \right)^2 \right] \tag{16}$$

where V_{bn} is the normal velocity of the incident droplet and $V_{a,\max} = 0.3V_{bn}$. Equation (16) is derived from the experiment of Mundo et al. (1995), which provides detailed information on the velocity distribution of the secondary droplets.

The next quantity that needs to be determined is the orientation of the vector $\vec{V}_{an}$, including the ejection angle θ and the azimuth angle β of the secondary droplet. The ejection angle of the secondary droplet θ is measured from the wall, which is affected by many factors, such as wall conditions (surface roughness and film thickness) Allen (1988) indicated that when droplets impact upon a deep water, the ejection angle of the secondary droplet lies at 30 $\sim$ 70° with a larger possibility, while Gahdiri (1978) found that the ejection angle of the secondary droplet is more likely in the range of 20 $\sim$ 60° when droplets impact on a rough soil surface. Bai et al. (2002) assumed that the ejection angle of the secondary droplet is in the interval (5°, 50°) uniformly. In this study, the ejection angle of the secondary droplet is taken in the interval (2°, 30°) uniformly, according to the suggestion from Allocca et al. (2006), and the reason will be explained later.

The azimuth angle β of the secondary droplet is defined as the angle that the tangential velocity makes with the vector $\vec{e}_t$ in the plane of the wall (see Fig. 3), which is in the interval (0, π). The azimuth angle is statistically calculated by the distribution suggested by Naber and Reitz (1988) in this study as

$$\beta = -\frac{\pi}{\chi} \ln\left[1 - k(1 - e^{-\chi})\right] \tag{17}$$

where k is another random number distributed uniformly in the interval (0, 1), and χ is a quantity related to the incident droplet angle ϕ, which is measured from the normal direction.

$$\sin\varphi = \frac{e^{\chi} + 1}{e^{\chi} - 1} \frac{\chi^2}{\chi^2 + \pi^2} \tag{18}$$

In this study, it is assumed that tangential splashing has no influence on the normal velocity of the splashed droplet and only transfers a portion of its tangential momentum to the secondary droplet. The tangential velocity of the secondary droplet resulting from the tangential splashing is

$$\vec{V}_{at} = \xi \vec{V}_{bt}, \tag{19}$$

where ξ is the friction coefficient. In this study, the friction coefficient is 0.95. Bai et al. (2002) adopts ξ in the range of $0.6 \sim 0.8$. However, Allocca et al. (2006) indicated that BG model underestimated the wall spray radius and overestimated the splash height, especially under the conditions of high injection pressure. It was suggested that the ejection angle should be in the interval $(2^\circ, 30^\circ)$ and the friction coefficient should be set at 0.95 (Allocca et al., 2006). It is well known that the injection pressure under the conditions of modern direct-injection diesel engines is very high, so it is reasonable to adopt the suggestions from Allocca et al. (2006).

Overall, the new spray/wall interaction model proposed in this study considers both a dry wall and wetted wall from the view that the spray will impinge onto the dry piston surface at the first stage of cold starting, and then impinge onto the film produced by the preimpingement. The impingement regimes for the dry wall are deposition and splash, and the regimes in the conditions of wetted wall consist of stick, rebound, spread, and splash. The regime transition threshold between the deposition and splash for the dry wall case is based on the experimental results of Cossali et al. (1997), which accounts for a wide range of surface roughness of the typical piston surface of engines. And for the case of a wetted wall, the transition threshold between spread and splash is determined by the experimental studies of Wang et al. (2002), who conducted systematic experiments by causing a single droplet to impact upon the wetted wall surface covering with different film thickness, and could fully explain the effects of film thickness on the transition threshold when the surface is wet. The mass ratio between the secondary droplets and the incident droplets is determined by a formula based on curve-fitting experimental results according to Yarin and Weiss (1995) for a dry wall. For wetted wall, the mass ratio can be determined by the work of Bai and Gosman (1995) from the viewpoint that the mass ratio may be larger than 1 because splashing droplets may entrain liquid film from the surface film. The size distribution of the secondary droplets is adopted by an updated log-normal distribution function from the work of Wu (2003), which may be more suitable to describe the process of the atomization of the secondary droplets formed by splash. The velocities of secondary droplets are determined by a Nukiyama-Tanasawa distribution function, which is derived from the experimental measurements of Mundo et al. (1995), and the ejection angle of the secondary droplets of the new model is taken in the range of $2 \sim 30^\circ$ uniformly, which is suitable for the case of high injection pressure according to the work from Allocca et al. (2006).

The necessity of improvements of the spray/wall interaction model in this study can be summarized in two aspects. First, a few spray/wall interaction models have been validated against experimental results under the PCCI-engine relevant conditions, i.e., high injection pressure and intermediate-to-high backpressure. Second, many well-developed spray/wall interaction models could not accurately predict the penetrations of the impinged spray and the characteristics of the secondary droplets produced by splash under the conditions of high-injection-pressure practical diesel engines.

3. NUMERICAL METHOD

The computational fluid dynamics (CFD) code used in this study is KIVA-3V (Amsden, 1997), which solves the three-dimensional equations of reactive flows with sprays using a structured grid. The particle method is employed in KIVA-3V to represent the spray, in which each computational particle represents a parcel of real droplets with similar thermodynamic and kinematic properties. Several enhanced submodels are introduced in the code to accurately account for spray breakup, collision, atomization, and evaporation processes, which are listed in Table 1.

The fuel model used in this study is the diesel fuel model DF2. The standard k-ε turbulence model was employed for the simulation of diesel injection in the constant volume combustion chamber with quiescent ambient gas. The droplet breakup process was described by the Kelvin-Helmholtz Rayleigh-Taylor (KH-RT) breakup model (Ricart et al., 2000), which is based on a linear stability analysis of liquid jets (Reitz and Bracco, 1986; Reitz, 1987). Our previous study (Jia et al., 2008a) indicated that the KH-RT model predicted the atomization and evaporation characteristics well under PCCI-engine relevant conditions, including the spray penetration, vapor distribution, and the diameter and velocity of the droplets. The constants of the KH-RT breakup model used in this study are summarized in Table 2. Furthermore, the collision model developed by Nordin (2001) with the improvement of grid independence was employed to the KIVA-3V code. The dynamics of the wall film was simulated by the model developed by O'Rourke and Amsden (1996), which considers the effects of the motion due to film inertia, splash of impinging spray, and film spreading resulting from the impingement forces on liquid film evolution. The droplet drag force and single-component evaporation model provided by KIVA-3V were also adopted in the simulations. For simplicity,

TABLE 1: Improved models

Turbulent model	Standard k-ε model (Amsden, 1997)
Breakup model	KH-RT model (Ricart et al., 2000)
Collision model	Nordin model (Nordin, 2001)
Wall film model	O'Rourke and Amsden model (O'Rourke and Amsden, 1996)

TABLE 2: Constants used in the KH-RT breakup model

Constant	Explanation	Value
C_b	Jet breakup length	30
B_1	Time scale for KH	18
B_0	Product droplet radius for KH	0.61
C_t	Time scale for RT	1.0
C_{3rt}	Product droplet radius for RT	2.5

the present paper did not consider the cavitation and turbulence effect inside the nozzle, and all the initial diameters are assumed to be the same as the nozzle orifice diameter.

4. RESULTS AND DISCUSSION

In an attempt to validate the new spray/wall interaction model, the model was integrated into the KIVA-3V code to compare with both the experimental results and the predictions of the OA model in this section. The main reason for using the OA splash model (O'Rourke and Amsden, 2000) for comparison is that the OA splash model and the OA particle wall film model were integrated into KIVA model as the default models, and have been widely applied in engine simulations. According to the investigation of Kong (2007), the OA splash model and the OA particle wall film model can be treated as the baseline to develop another more accurate droplet/wall interaction model. The validations presented in this study primarily focus on the penetrations of the impinged spray, including the spray radius, spray height, and the local parameters of the impinged spray, including the velocities and sizes of the secondary droplets at a given position.

All the simulations in constant volume combustion chambers were calculated in a cylindrical domain where grid size varies from 0.6 to 3 mm, as shown in Fig. 4. The sensitivity of the time step, the grid size, and the number of liquid parcels on the predictions were performed and evaluated for each case tested in this study in order to get converged and reliable solutions. The mesh was refined using a geometric distribution in both radial and azimuthal directions near the nozzle with a minimum grid size of 0.6 mm. It was found that the spray penetration and the spray/wall interaction behavior were not significantly affected by the grid size with further grid refinement. Throughout the duration time of injection, a total of 30,000 droplet parcels were introduced to represent the spray for most cases according to the injected fuel mass, and it was found that further increasing the droplet parcels did not obviously affect the spray penetration and the

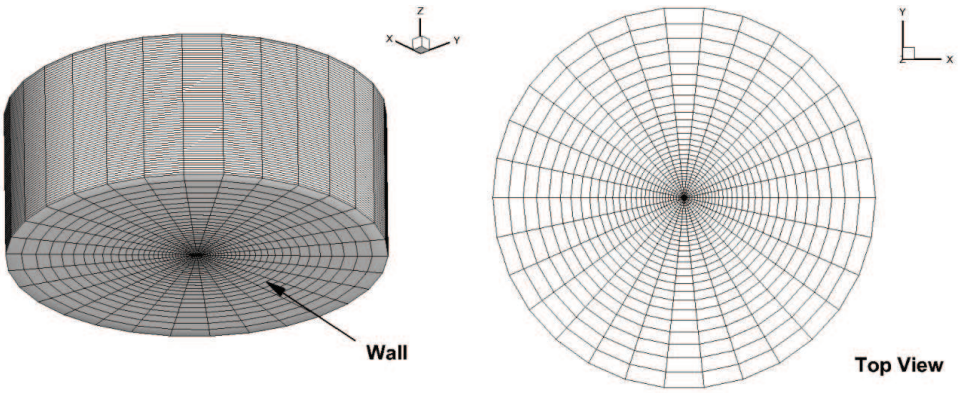

FIG. 4: Grid used in the present study.

behavior of the impinged spray. The time step used in this study is in the range of 0.1–1 μs with the variation of injection pressure, which is capable of achieving satisfactory convergence for the numerical solutions. Moreover, the injection velocity is determined using the square wave injection pulse according to the injected fuel mass, injection duration, injection pressure, and the parameters of the nozzle. The nozzle center was placed 1 mm below the center of the top edge.

In predicting the spray/wall interaction process, the characteristics of the spray before impingement dramatically affect the behavior of the impinged spray. Therefore, it is necessary to validate the spray behavior before impinging on the wall. Figure 5 shows comparisons of spray penetration between the predictions using the KH-RT breakup model and the experimental measurements of Hiroyasu and Kadota (1974). In the predictions, the ambient pressure is 3 and 5 MPa, and more detailed experimental conditions can be found in Hiroyasu and Kadota (1974). It can be seen from Fig. 5 that the KH-RT breakup model reproduces the spray penetration quite well at both ambient pressures. More about the validations of the spray and atomization characteristics of the spray before impingement can be found in our previous work (Jia et al., 2008a).

4.1 Validations for the Experiments of Fujimoto et al. (1990)

Fujimoto et al. (1990) experimentally investigated the phenomenon of spray/wall interaction by injecting diesel to a flat wall at high ambient pressure and room temperature with various inclination angles. The laser light extinction method was used to measure the spatial and temporal distributions of the droplet density. Some sets of the

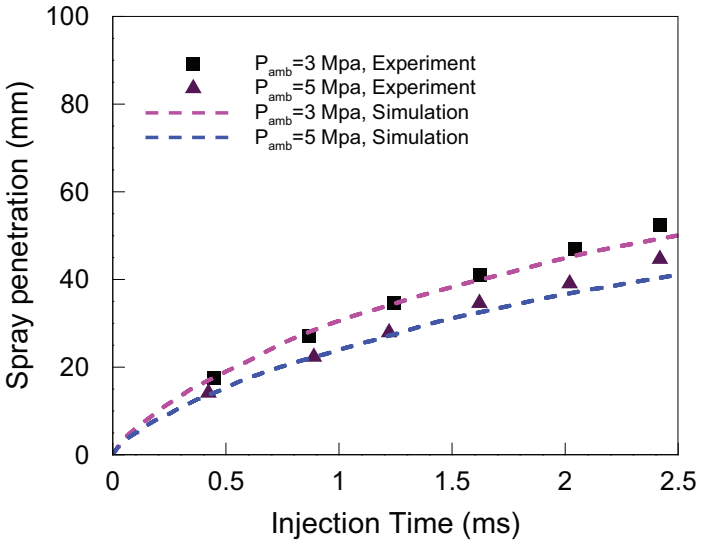

FIG. 5: Comparisons of the spray penetrations between the results predicted by the KH-RT breakup model and the experimental measurements of Hiroyasu and Kadota (1974).

experimental data which measured the radius and the height of the impinged spray under conditions of normal impingement and inclined impingement are used to test the new model in this section. The test conditions of the experiment are listed in Table 3.

As shown in Fig. 6(a), the radius of the impinged spray (R_w) is defined as the distance from the axis to a domain in which 99% mass of the total secondary droplets is contained. The height of the impinged spray (H_w) is defined as the distance between the wall and the domain above which less than 1% mass of the secondary droplets lies.

The radius and the height of the impinged spray using the new model and the OA model versus time are compared with the experimental data under conditions of normal impingement, as shown in Figs. 7(a) and 7(b). It can be seen from Fig. 7(a) that both the new model and the OA model predict the radius of the impinged spray well. However, the OA model slightly overestimates the radius at the late stage of the injection, while the new model predicts the radius very well. Concerning the height of the impinged spray shown in Fig. 7(b), both the new model and the OA model underestimate the height of the impinged spray at the start of the impingement and overestimate the height at the end of the injection. The OA model reproduces the height better than the new model, which

TABLE 3: Specifications of the experiments from Fujimoto et al. (1990)

Wall distance (mm)	24
Gas pressure (MPa)	1.5
Gas temperature (K)	293
Nozzle diameter (mm)	0.2
Injection angle (°)	90
Fuel injected (mm^3)	8.3
Injection duration (ms)	1.3
Injection pressure (MPa)	13.8
Fuel	Diesel

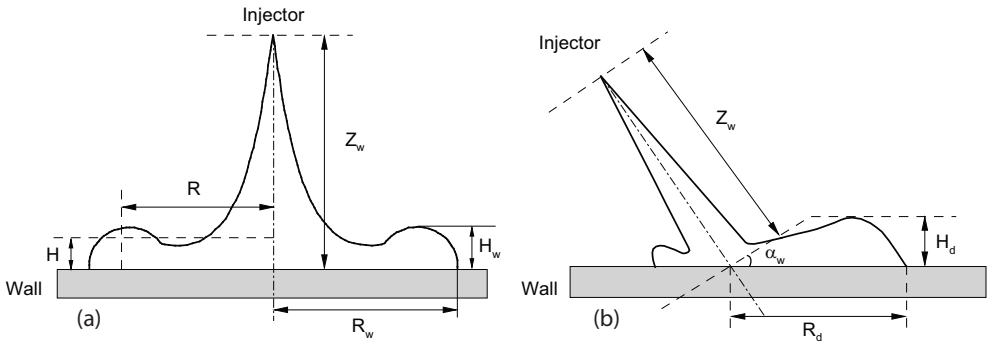

FIG. 6: Structure of the impinged spray.

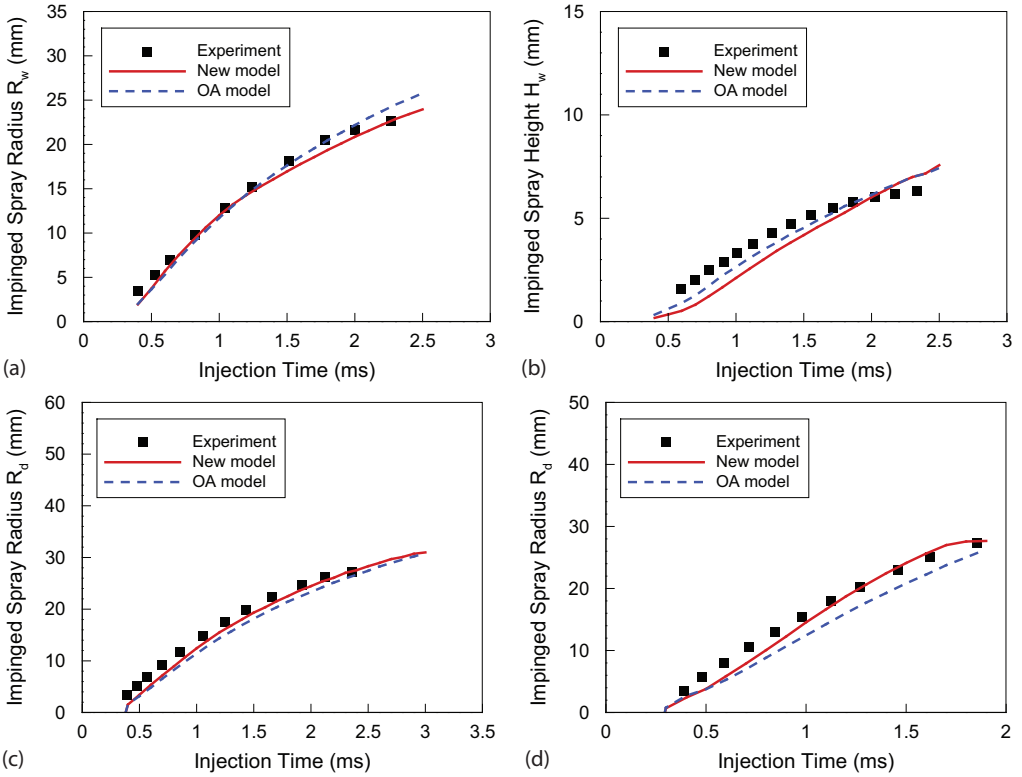

FIG. 7: Comparisons of the predictions and measurements Fujimoto et al. 1990) for (a,c,d) impinged spray radius and (b) impinged spray height. (a) $\alpha_w = 0°$, (b) $\alpha_w = 0°$, (c) $\alpha_w = 15°$, and (d) $\alpha_w = 30°$.

slightly underpredicts the height compared to the OA model. This may be explained by the ejection angle of the new model, which lies at $2 \sim 30°$ uniformly. As a matter of fact, the ejection angle could be affected by many factors, such as the energy of the impinged droplet and the wall conditions. Andreassi et al. (2007) concluded that the range of ejection angle is a function of the normal Weber number of the impinged droplet in terms of injection pressure and backpressure, whereas, more experimental data for the ejection angle of the secondary droplet are required in order to better describe its characteristics. Figures 7(c) and 7(d) show comparisons of the radius of the impinged spray (R_d) [defined in Fig. 6(b)] in the downstream area of the impingement site for the cases of inclined impingement. It can be clearly seen that the new model gives better agreement with the experimental data. Nevertheless, the OA model slightly underestimates the radius of the impinged spray, especially under the conditions of the inclined angle (α_w) of 30° [see Fig. 7(d)].

Figure 8 shows the images of the spray and gas velocity fields predicted by the new model at three different times after the start of injection. It can be seen that there

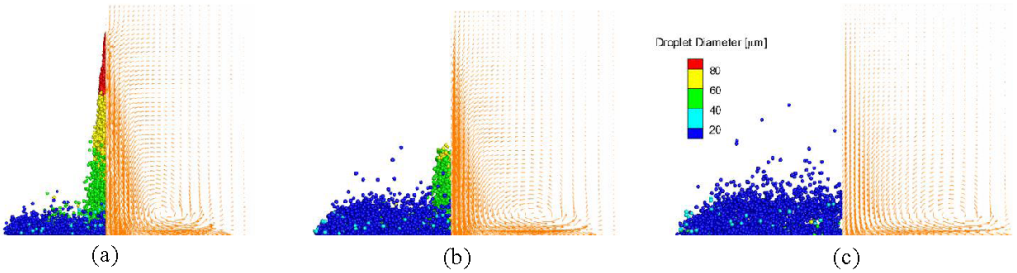

FIG. 8: Spray images (left side) and gas velocity fields (right side) from the new model at (a) t = 1.0 ms, (b) t = 1.4 ms, and (c) t = 1.8 ms.

is a dense region near the wall in the spray tip which contains many small secondary droplets that penetrate radially and axially outward from the impingement site. From the spray images, it also can be observed that some larger droplets are developed in the late period of the impingement. From the gas velocity distributions shown in Fig. 8, it is evident that a wall jet moves radially outward from the impingement site. Near the tip of the wall jet, there is a wall-guided vortex which moves in the radial direction rapidly and influences the movement of the droplets. Thus the small secondary droplets resulting from splashing have more opportunities to coalesce and form larger droplets.

In general, both the new model and the OA model predict the radius and height of the impinged spray quite well under the low injection pressure tested in this section. However, it is known that in the conditions of modern direct-injection engines, the injection pressure is very high, which will produce different behaviors compared to cases with low injection pressure. Therefore, it is necessary to test the capability of the spray/wall interaction model under conditions of high-injection-pressure-related practical diesel engines.

4.2 Validations for the Experiments of Park and Lee (2004)

Park and Lee (2004) investigated the characteristics of a diesel spray impinged on a wall at various impinging and ambient conditions. The spray visualization system, which was composed of a Nd:YAG laser and an intensified charge-coupled device (ICCD) camera was used to visualize the spray-impinged processes. One series of the experimental data for the radius and height of the impinged spray as well as the Sauter mean diameter (SMD) distributions of the secondary droplets formed by splash under conditions of high injection pressure was adopted in this section to evaluate the capability of the new model under high injection pressure. The related parameters of the experiment are summarized in Table 4.

Figure 9 shows the patterns of the impinged spray 0.5 ms after the start of injection. It is evident that the OA model shows a remarkably different trend compared with the new model. The OA model produces an unrealistic spray profile, including the

TABLE 4: Specifications of the experiments of Park and Lee (2004)

Wall distance (mm)	50
Wall temperature (K)	293
Gas pressure (MPa)	0.1
Gas temperature (K)	293
Nozzle diameter (mm)	0.3
Injection angle (°)	90
Fuel injected (mg)	16.8
Injection duration (ms)	1.0
Injection pressure (MPa)	80
Fuel	Diesel

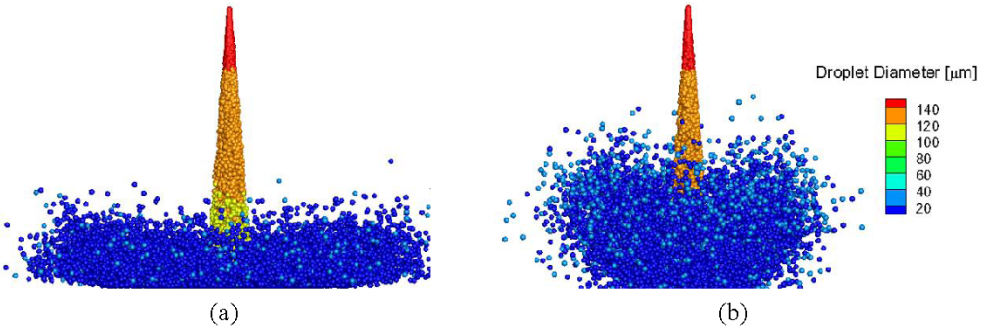

FIG. 9: Spray profiles at 0.5 ms for (a) the new model and (b) the OA model.

underestimation of the radius of the impinged spray and overestimation of the height of the impinged spray. In an attempt to show a quantitative comparison of the two models with the experimental data, the time evolution of the radius and height of the impinged spray from the computed results and experimental data are shown in Fig. 10. It is confirmed that the new model simulates the radius and height of the impinged spray rather well, while the OA model dramatically underestimates the radius and overestimates the height of the impinged spray. The discrepancy between the predictions from the OA model and the measurement may be explained by the fact that the velocity distribution of the secondary droplet produced by splash in the OA model yields a much larger normal component and lower tangential component of the secondary droplet velocity than the measurement for the case of high injection pressure. Therefore, the secondary droplet predicted by the OA model penetrates longer distances in the normal direction compared to the measurement, at the same time leading to shorter radial penetration.

Figure 11 gives comparisons of the SMD between the predictions and the corresponding measurements, including the overall SMD evolution and the radial distribution of the local SMD at H_w = 10 mm, after the start of injection at 3.0 ms for the

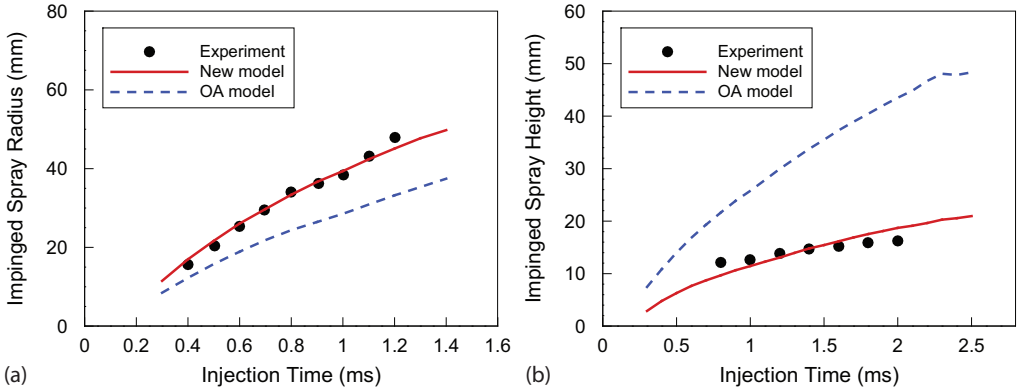

FIG. 10: Comparison between the computed results and experimental data (Park and Lee, 2004) for (a) the radius of the impinged spray and (b) the height of the impinged spray.

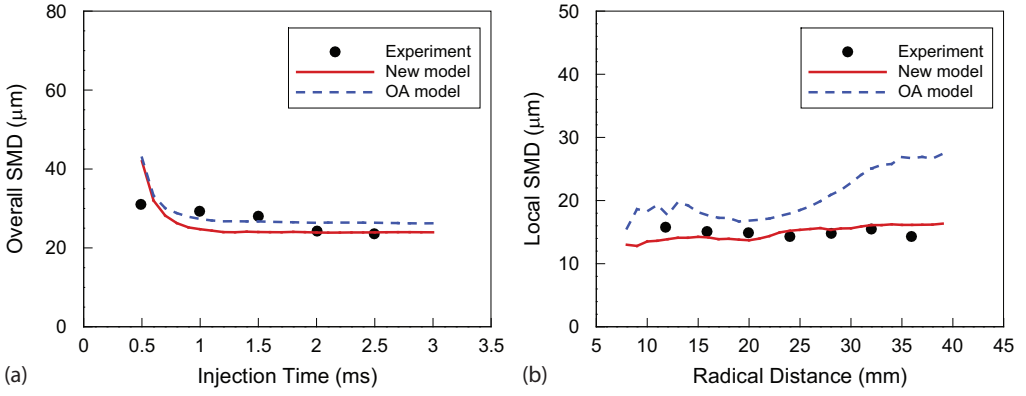

FIG. 11: Comparison between the calculated SMD results and the experimental results of Park and Lee (2004) for (a) the overall SMD of the impinged spray and (b) the local SMD of the impinged spray at H_w = 10 mm after the start of injection at 3.0 ms.

impinged spray. It can be seen from Fig. 11(a) that both the new model and the OA model reproduce the evolution of the overall SMD reasonably well, in which the SMD decreases before 1.0 ms and then remains nearly constant. From Fig. 11(b) it is evident that the new model predicts the local SMD more accurately than the OA model, which significantly overestimates the local SMD, especially at locations with longer radial distance. This could be explained by the following two aspects. One reason is that the new model uses a log-normal distribution function to describe the variations of the sizes of the secondary droplets, which may be more suitable for the atomization process of the secondary droplets formed by splash. And the other reason is that the new model adopts $d_m/d_b = \max(19.86K'^{-0.5}, 0.05)$ to determine the mean sizes of the secondary

droplets, while the OA model uses $d_m/d_b = \max(K'_{crit}/K', 6.4/\mathrm{We}, 0.06)$. Thus the SMD predicted by the new model is lower than that of the OA model for the case of high-energy impingement and agrees better with the experimental data.

For diesel PCCI engines, the fuel vapor distribution during and the period of the spray/wall interaction are very important, because it significantly influences the combustion and emission characteristics. Mohammadi et al. (2002) investigated the effect of spray/wall interaction on the gas entrainment process in diesel sprays and indicted that the gas entrained into the spray area, typically at the impinging area due to the gas vortex around the spray. Figure 12 shows the predicted equivalence ratio distributions and gas velocity fields by the new model at three different times. It can be clearly seen that the ambient air entrains into the region between the spray axis and the wall-jet vortex, so that richer fuel/air mixtures primarily exist in the vortex front and the spray cone regions. Thus it can be said that the structure of the vortex has an important role in the fuel/air mixing processes. Since the vortex structure is significantly affected by the impinged droplets (see Fig. 8), it confirms the importance of the spray/wall interaction in enhancing the equivalence ratio distributions, which is consistent with the experimental results of Mohammadi et al. (2002).

4.3 Validations for the Experiments of Allocca et al. (2006) and Andreassi et al. (2007)

Allocca et al. (2006) and Andreassi et al. (2007) studied the characteristics of the normal impingement of a diesel spray under the conditions of high injection pressures (up to 120 MPa) and various backpressures both numerically and experimentally. In the experiments, a common rail injection system was employed to inject diesel fuel into a flat stainless steel wall. A pulsed laser sheet was used to light the impinged spray, and the images of the impinged spray were photographed by a CCD camera at different times after the start of injection. The specifications of the experiments are listed in Table 5.

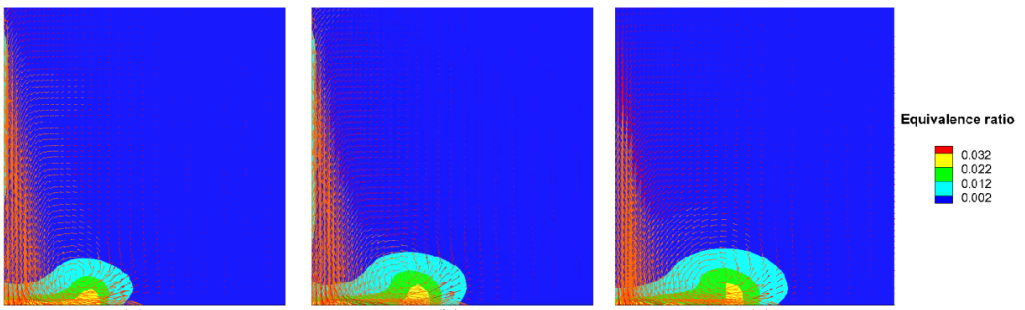

FIG. 12: Predicted equivalence ratio distribution and gas velocity field from the new model at (a) t = 0.8 ms, (b) t = 1.0 ms, and (c) t = 1.2 ms.

TABLE 5: Specification of experiments from Allocca et al. (2006) and Andreassi et al. (2007)

Wall distance (mm)	22
Wall temperature (K)	298
Gas pressure (MPa)	0.1, 3.0
Gas temperature (K)	293
Nozzle diameter (mm)	0.18
Injection angle (°)	90
Fuel injected (mg)	8.44 (80 MPa), 9.67 (120 MPa)
Injection duration (ms)	1.0
Injection pressure (MPa)	80, 120
Fuel	Diesel

The images of the impinged spray simulated by the new and the OA model are compared with the experimental measurements at t = 300 μs in Figs. 13 and 14. As can be seen, the increase of injection pressure from 80 to 120 MPa leads to the increased height and radius of the impinged spray, which are accurately reproduced by the new model. Similar to the results shown in Section 4.2, it is also found that the new model reproduces the shapes of the impinged spray much better than the OA model. Therefore it can be concluded that the OA model may be inadequate to represent the physical phenomenon of splash, which is consistent with the numerical results from Allocca et al. (2006).

The quantitative comparison of the radius and the height of the impinged spray among the predictions and the measurement at the injection pressure of 80 MPa and the backpressure of 0.1 MPa is shown in Fig. 15. It is obvious that the new spray/wall

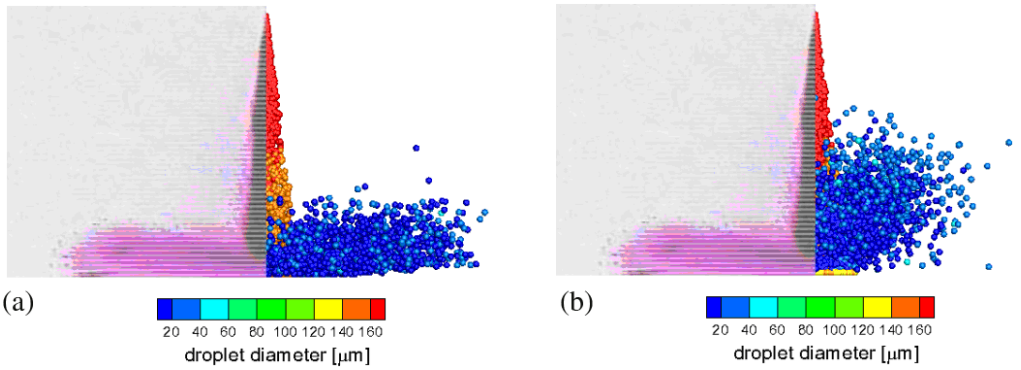

FIG. 13: Comparisons of the images of the spray between the numerical results (right) and the measurements (left) (Allocca et al., 2006) at t = 300 μs for (a) the new model and (b) the OA model (P_{inj} = 80 MPa, P_{amb} = 0.1 MPa).

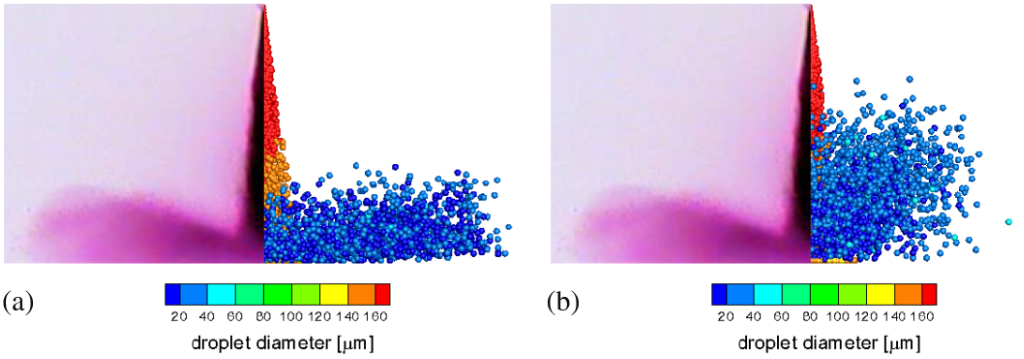

FIG. 14: Comparisons of the images of the spray between the numerical results (right) and the measurements (left) Allocca et al., 2006) at t = 300 μs for (a) the new model and (b) the OA model (P_{inj} = 120 MPa, P_{amb} = 0.1 MPa).

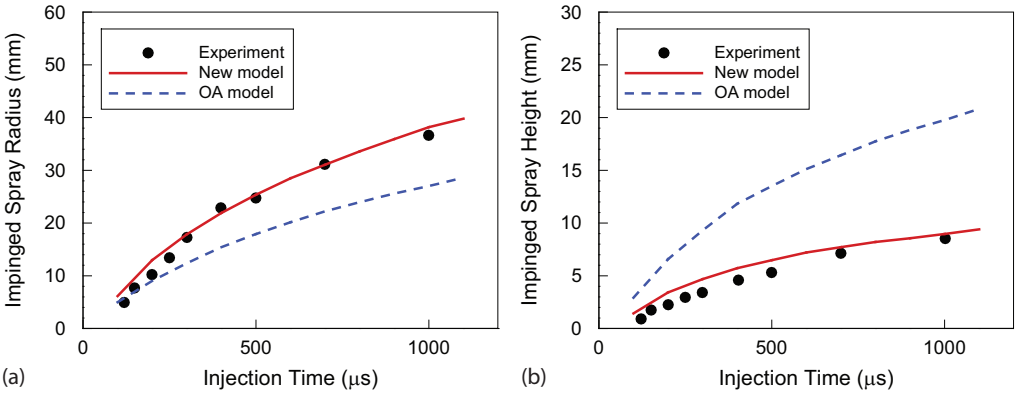

FIG. 15: Comparisons of the predicted results and experimental data (Andreassi et al., 2007) versus time (P_{inj} = 80 MPa, P_{amb} = 0.1 MPa). (a) The radius and (b) the height of the impinged spray.

interaction model predicts the radius and the height of the impinged spray quite well, while the OA model underestimates the radius and overestimates the height with large discrepancy relative to the measurement, which is consistent with the results shown in Fig. 10. The profiles of the impinged spray at injection pressures of 80 and 120 MPa are shown in Figs. 16 and 17, respectively. In general, the new model is capable of accurately reproducing the evolution of the impinged spray at both injection pressures. In the case of 80 MPa injection pressure, the predicted radius of the impinged spray from the new model is in good agreement with the measured data, whereas the height of the impinged spray is slightly overpredicted by the new model. Meanwhile, for the case of 120 MPa injection pressure, the new model reproduces both the radius and the height of the impinged spray reasonably well.

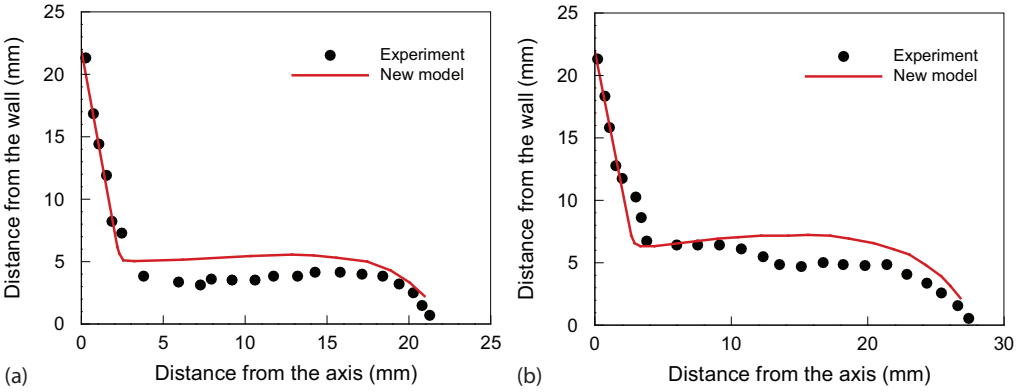

FIG. 16: Comparisons of the profiles of the spray between the new model and the experiments (Allocca et al., 2006) at (a) t = 400 μs and (b) t = 700 μs (P_{inj} = 80 MPa, P_{amb} = 0.1 MPa).

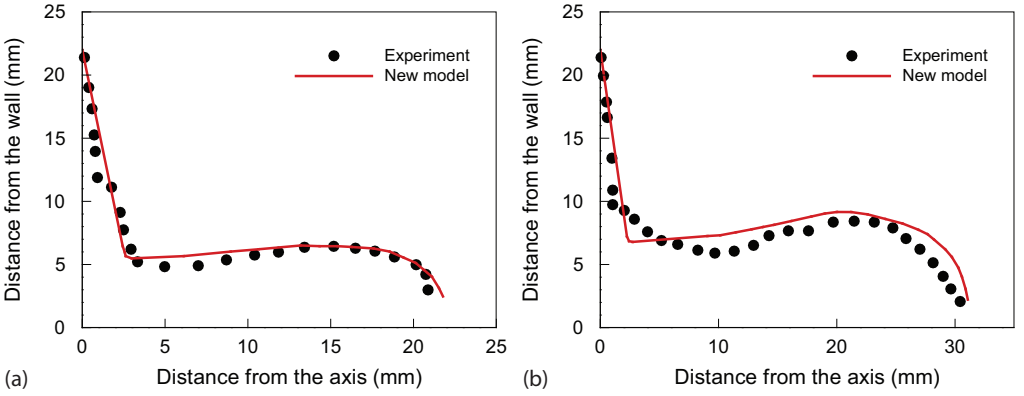

FIG. 17: Comparisons of the profiles of the spray between the new model and the experiments (Allocca et al., 2006) at (a) t = 400 μs and (b) t = 700 μs (P_{inj} = 120 MPa, P_{amb} = 0.1 MPa).

Furthermore, Fig. 18 shows comparisons of the profiles of the impinged spray between the new model and the experimental measurements at a backpressure of 3 MPa and injection pressure of 80 and 120 MPa. As can be seen, good agreements between the numerical and the experimental results are obtained. It is found that the new model satisfactorily reproduces the experimental observation that the radius and height of the impinged spray decrease with the increase of backpressure. This can be explained by the fact that as the surrounding pressure increases, the spray penetration decreases due to the increased density of the surrounding air. With the spray penetration decreasing, the gas velocity setup over the wall decreases due to the low spray inertia. Thus the tangential

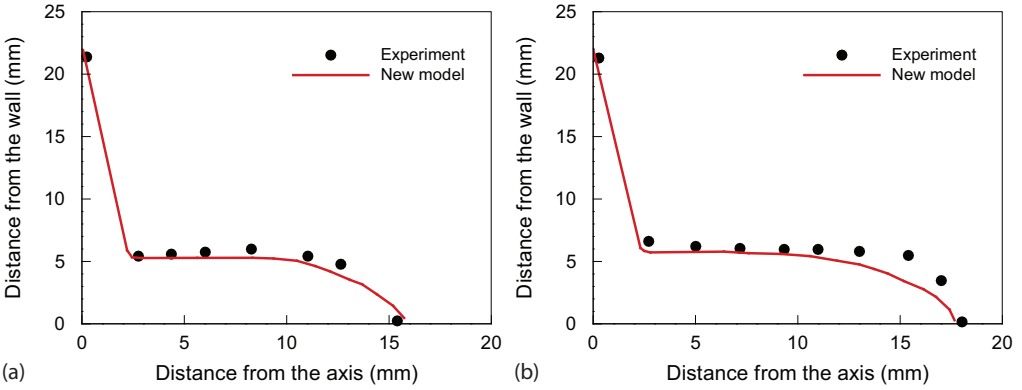

FIG. 18: Comparisons of the profiles of the spray between the new model and the experiments (Andreassi et al., 2007) with P_{amb} = 3 MPa at t = 1000 μs for (a) P_{inj} = 80 MPa and (b) P_{inj} = 120 MPa.

velocities of the secondary droplets also decrease, which results in the low penetration of the impinged spray.

4.4 Validations for the Experiments of Arcoumanis and Chang (1994)

Arcoumanis and Chang (1994) conducted the experiments under atmospheric conditions to investigate the spatial and temporal characteristics of the transient diesel spray impinging normally onto unheated walls. Phase Doppler anemometry was employed to measure the sizes and tangential velocities of the secondary droplets produced by splashing. A summary of the related parameters used in the investigation is given in Table 6.

In the experiments, the measurement points were located at radial distances of R = 6 mm, 10 mm, and 15 mm from the spray axis, and at vertical distances of H = 0.5 mm,

TABLE 6: Specifications of the experiment from Arcoumanis and Chang (1994)

Wall distance (mm)	30
Gas pressure (MPa)	1
Gas temperature (K)	293
Nozzle diameter (mm)	0.22
Injection angle (degree)	90
Fuel injected (mm^3)	4.0
Injection duration (ms)	1.0
Injection pressure (MPa)	26
Fuel	Diesel

1.5 mm, 3 mm, and 5 mm away from the wall. Only the experimental results at heights of 0.5 mm and 5 mm away from the wall are discussed in this section, which are related to the representative regions of the two-phase wall jet—the main wall-jet region, the stagnation region, and the downstream region (Arcoumanis and Chang, 1994), as shown in Fig. 19.

Figure 20 shows comparisons of the computed droplet tangential velocities and the corresponding experimental measurements in the main wall-jet region (H = 0.5 mm, R = 6 mm) and in the stagnation region (H = 5 mm, R = 6 mm). It is depicted that at the position of H = 0.5 mm and R = 6 mm, both the new model and the OA model underpredict the tangential velocities of the secondary droplets. However, the results predicted by

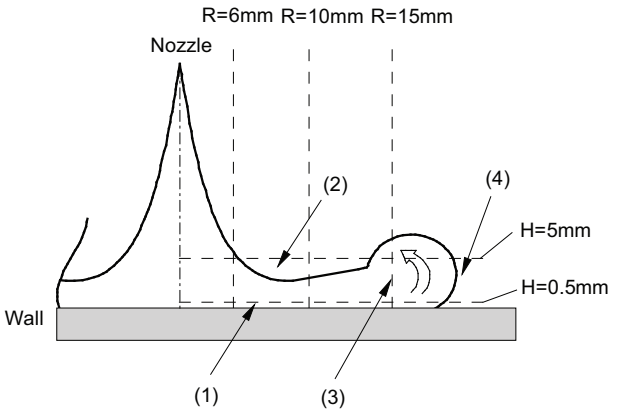

FIG. 19: Measurement locations and the representative regions of the two-phase wall jet: (1) main wall-jet region, (2) stagnation region, (3) wall-jet vortex, and (4) leading edge from the experiment of Arcoumanis and Chang (1994).

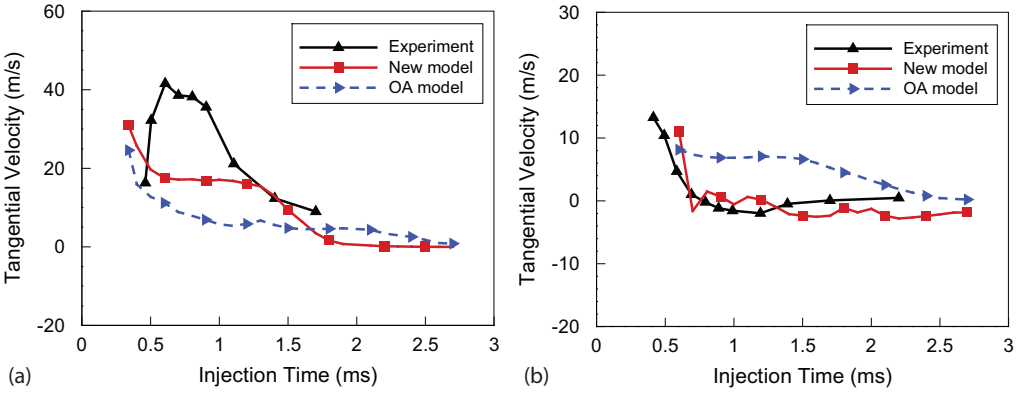

FIG. 20: Comparison of the computed tangential velocity of the secondary droplet with the experimental data from Arcoumanis and Chang (1994) at (a) H = 0.5 mm, R = 6 mm and (b) H = 5 mm, R = 6 mm.

the new model show better agreement with the experimental data than those of the OA model, especially near 1.5 ms after the start of injection. At H = 5 mm and R = 6 mm, the new model predicts the tangential velocities quite well and shows almost the same trend with the experimental measurement, while the OA model significantly overestimates the measured data. It also can be observed from Fig. 20 that with the increased distance from the wall, the mean tangential velocity decreases in general, indicating the tangential momentum of the impinged droplets is relatively large in the near-wall region. This trend is captured by both the new model and the OA model, although some discrepancies exist between these two models.

Comparisons of the computed tangential velocities and the experimental data in the main wall-jet region and near the stagnation region at H = 0.5 mm, R = 10 mm and H = 5 mm, R = 10 mm are shown in Fig. 21. The results simulated by the new model are better than those from the OA model, especially near the stagnation region at H = 5 mm, R = 10 mm. Figure 22 further depicts comparisons of the tangential velocities of the secondary droplets near the downstream region at H = 0.5 mm, R = 15 mm and H = 5 mm, R = 15 mm. It is evident that both the new model and the OA model underestimate the experimental data in the wall-jet region (H = 0.5 mm and R = 15 mm), which is similar to the conditions at H = 0.5 mm, R = 6 mm (see Fig. 20). At the position of H = 5 mm and R = 15 mm corresponding to the region of the wall-jet vortex, the new model gives better agreement with the experimental results than the OA model, which obviously overpredicts the experimental data. In particular, the new spray/wall interaction model accurately predicts the negative tangential velocities of secondary droplets after 2.0 ms, despite that the magnitudes of the negative tangential velocities are very small and close to zero. This indicates that there is a wall vortex existing in this region (Lee and Ryou 2000). However, the simulation with the OA model cannot efficiently reproduce the vortex in this region. This is primarily because the OA model

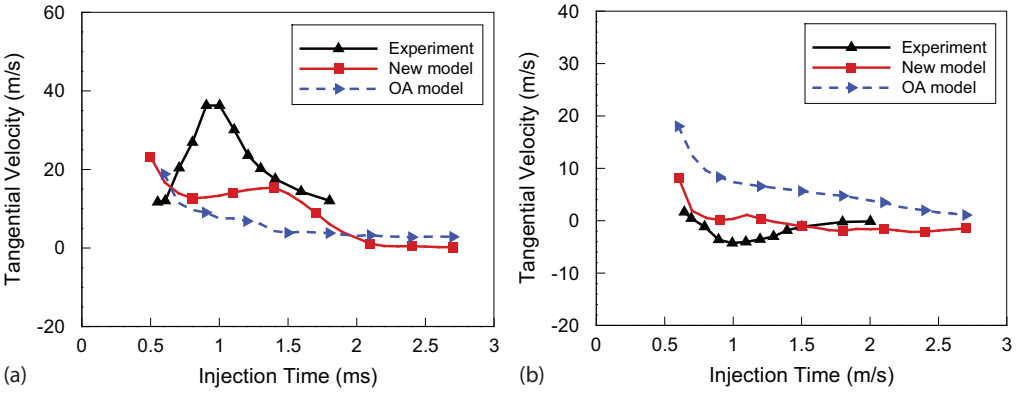

FIG. 21: Comparison of the computed tangential velocity of the secondary droplet with the experimental data from Arcoumanis and Chang (1994) at (a) H = 0.5 mm, R = 10 mm and (b) H = 5 mm, R = 10 mm.

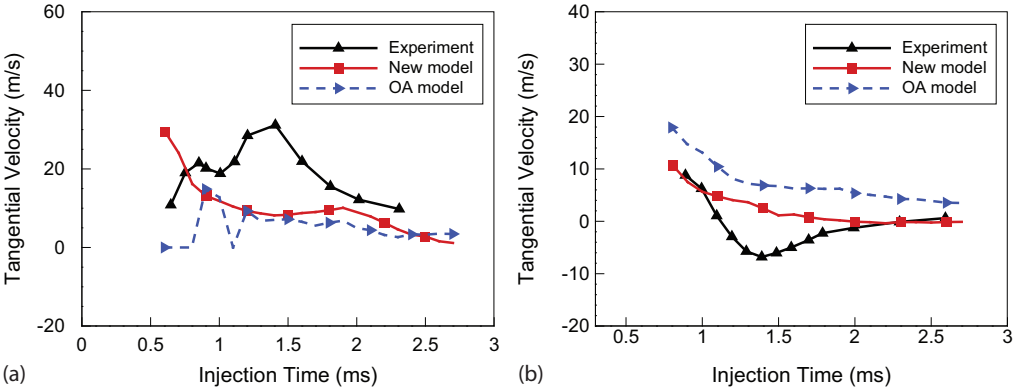

FIG. 22: Comparison of the computed tangential velocity of secondary droplet with the experimental data from Arcoumanis and Chang (1994) at (a) H = 0.5 mm, R = 15 mm and (b) H = 5 mm, R = 15 mm.

underpredicts the radial penetration of the impinged spray. Therefore, the radial distance between the vortex and the impingement site predicted by the OA model is less than that of the measurement, which means that the OA model cannot efficiently predict the vortex in the region of the wall-jet vortex.

Figures 23–25 give comparisons of the predicted SMD with the measurements at different locations. It is clearly observed that predictions from the new model agree with the experimental results much better than those from the OA model. The OA model overpredicts the SMD in most of the locations, which is consistent with the investigations of Jia et al. (2008b) and Lindgren and Denbratt (2004). Note that the new model uses a log-normal distribution function, which is updated from the work of Wu (2003), to

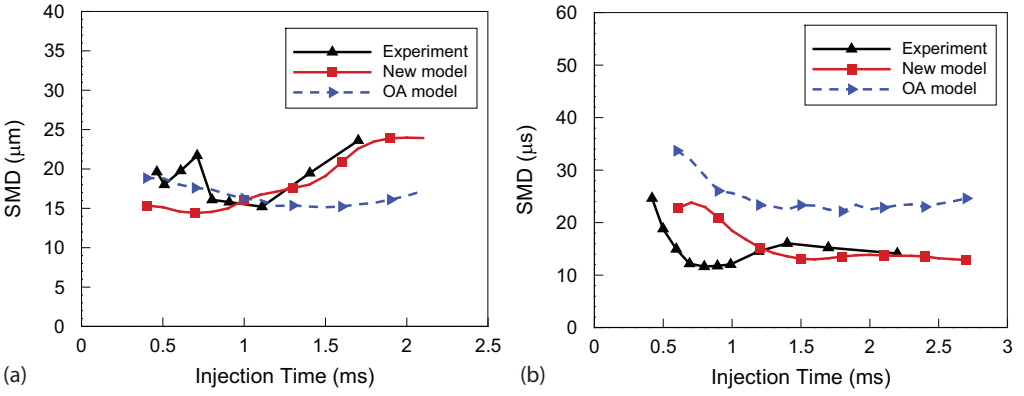

FIG. 23: Comparison of the predicted SMD with the experimental data from Arcoumanis and Chang (1994) at (a) H = 0.5 mm, R = 6 mm and (b) H = 5 mm, R = 6 mm.

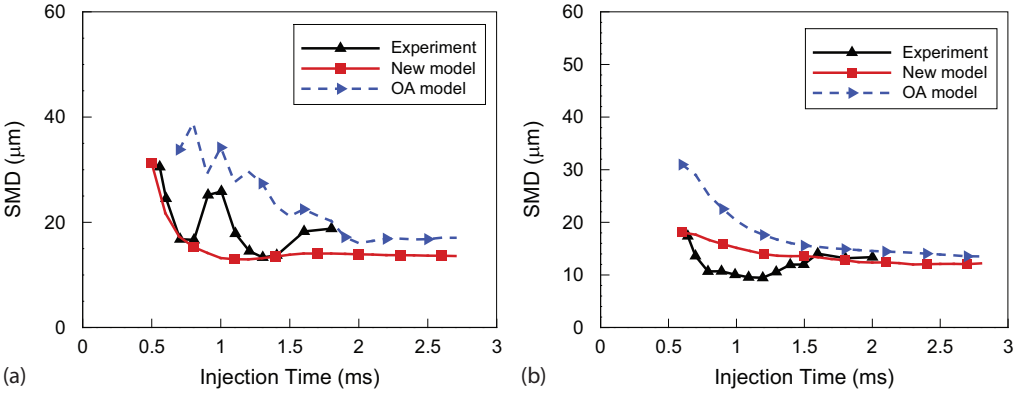

FIG. 24: Comparison of the predicted SMD with the experimental data from Arcoumanis and Chang (1994) at (a) H = 0.5 mm, R = 10 mm and (b) H = 5 mm, R = 10 mm.

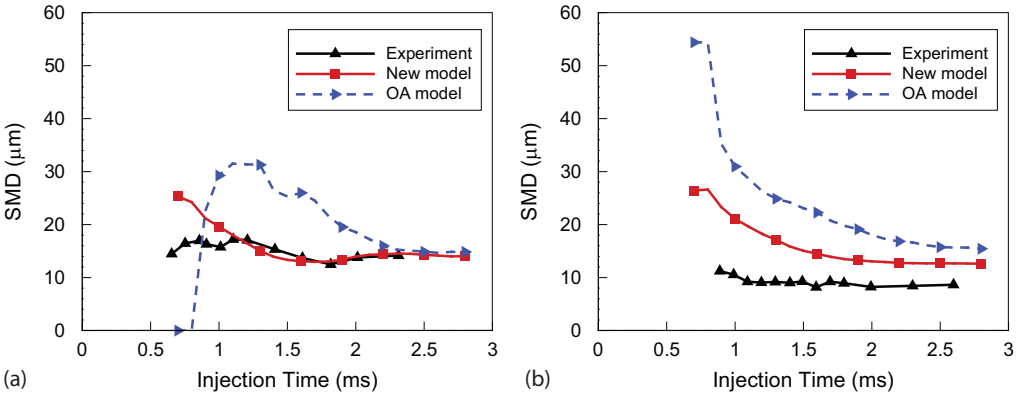

FIG. 25: Comparison of the predicted SMD with the experimental data from Arcoumanis and Chang (1994) at (a) H = 0.5 mm, R = 15 mm and (b) H = 5 mm, R = 15 mm.

determine the sizes of the secondary droplets. Thus it is believed that the log-normal distribution function can effectively describe the sizes of the secondary droplets due to its multiplicative nature, which may be similar to the practical process of the atomization of the secondary droplets after impingement.

It should be noted that the simulation results may also be affected by the submodels, including the droplet breakup model, droplet collision model, turbulence model, the interaction model between gas flow and spray, as well as the cavitation and turbulence inside the nozzle. Specifically, since the characteristics of the spray before the impingement significantly affect the behavior of the impinged spray, the employment of a reliable

spray breakup model and collision model is important for the simulation. Moreover, the turbulence model also strongly affects the motions of the secondary droplets formed by splash; thus accurate descriptions of the turbulent flow and the interaction between the gas flow and droplet is crucial for prediction of the penetration of the impinged spray. Additionally, the assumption of neglecting the nozzle cavitation and turbulence effect inside the nozzle may impact the outcomes of the impinged spray. Therefore further improvement of the related submodels and validation of the new spray/wall interaction model under wide operating conditions still needs to be performed in future work. However, it is found that the results predicted by the OA model in this study are consistent with the investigations of Jia et al. (2008b) and Allocca et al. (2006) with the KIVA-3V code. Therefore it is believed that the predictions presented in this study are reliable, and the overall trends of the impinged spray can be more accurately captured by the new model.

4.5 Validations for the PCCI Engine

Finally, the simulations in a diesel PCCI engine were conducted in order to demonstrate the capabilities of the new model to predict the effects of injection timings on the combustion and emission characteristics, and to investigate the effect of the injection timing on the mixture preparation process in practical PCCI engines. In this section the new spray/wall interaction model was integrated into the KIVA-3V code, which was then applied for the simulations of PCCI engine. For the engine simulations, the turbulent model is the renormalization (RNG) k-ε turbulent model (Han and Reitz, 1995), which can deal well with the variable-density engine flow within the combustion chamber. The wall heat-transfer model of Han and Reitz (1997) was also adopted, which considers the turbulent Prandtl number and the variations in the gas density in the boundary layer. A skeletal *n*-heptane mechanism using a decoupling methodology (Liu et al., 2012) was employed to predict the chemical reaction processes of the diesel fuel due to the similar ignition and heat release characteristics between *n*-heptane and diesel fuel. The skeletal *n*-heptane mechanism was extensively validated against corresponding experimental results under wide operating conditions and shows good agreement with the measurements. Therefore, the *n*-heptane mechanism is suitable for simulating the combustion process of PCCI engines in this section. In addition, the extended Zeldovich mechanism was used to simulate the formulation of NO_x and the complex processes of the formation and oxidation of soot were modeled by an improved phenomenological soot model (Jia et al., 2009).

The experimental data from Lee (2007) in a diesel PCCI engine were employed to validate the predicted combustion and emissions characteristics. A 45° (1/8 of cylinder) mesh with 18,706 cells at the top dead center (TDC), which is shown in Fig. 26, was adopted in the simulations. Detailed engine specifications and operating conditions are summarized in Table 7.

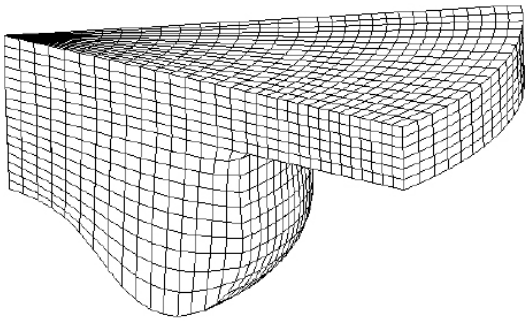

FIG. 26: Computational grids for the simulation of the PCCI engine.

TABLE 7: Engine specifications and operating conditions from the experiment of Lee (2007)

Displacement	0.477 L
Bore×stroke (mm×mm)	82 × 90.4
Compression ratio	16.0:1
Piston geometry	Open-crater-type bowl
Nozzle hole number	8
Nozzle hole diameter (mm)	0.133
Start of injection (° CA BTDC)	22.5∼40
Spray include angle (°)	130
Engine speed (rpm)	2000
Injection pressure (MPa)	150
Injection quantity (mg/cyc)	15.0
Fuel	Diesel

As shown in Fig. 27, the calculated in-cylinder pressure and heat release rate profiles show good agreement with the experimental measurements for the cases with various injection times. The simulated CO, HC, NO_x, and soot emissions are compared with the experimental results in Fig. 28. It also can be found that the predictions agree reasonably well with the measurements, although NO_x emission is underpredicted for all the injection times. It should be noted that the input parameters and the submodels still show some uncertainties for the multidimensional simulation. Specifically, a relatively simple NO_x emission model was employed in this study for the reduction of the computational time, which could also significantly affect the final predicted NO_x emissions. Overall, the computational model with the new spray/wall interaction submodel is capable of well reproducing the experimental data of the in-cylinder pressure, heat release, and emission characteristics for diesel PCCI combustion.

Jia et al. (2011) investigated the effects of injection timing and intake valve closing timing on the performance and emission characteristics of a diesel PCCI engine by

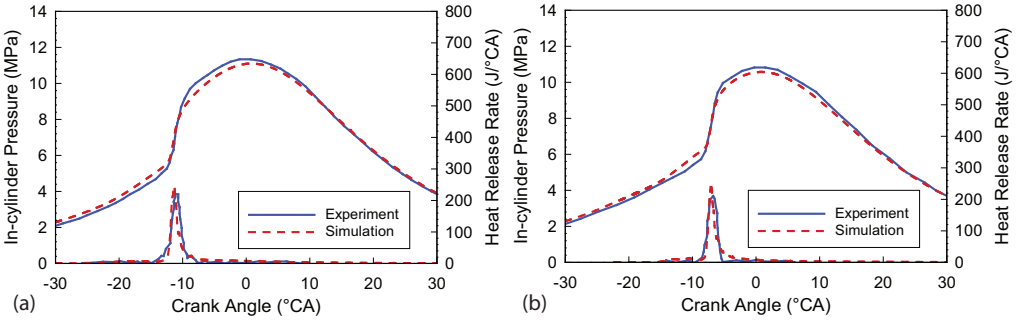

FIG. 27: Comparison of the predicted in-cylinder pressure and heat release rate with the experimental results (Lee, 2007) at (a) SOI = –35° CA ATDC and (b) SOI = –22.5° CA ATDC.

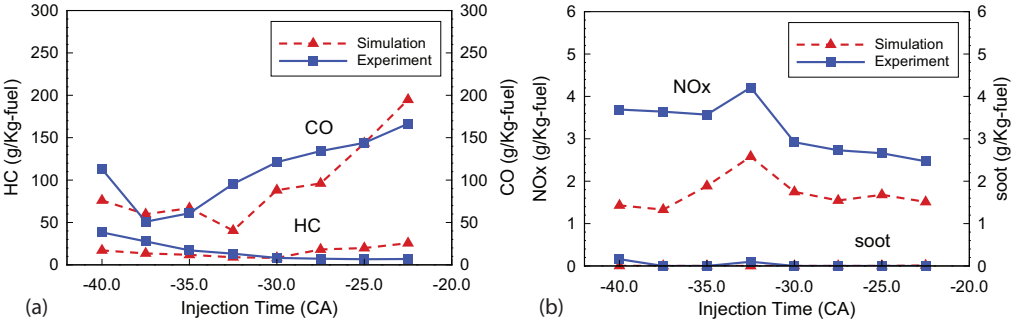

FIG. 28: Comparisons of emission characteristics between simulations and measurements (Lee, 2007) for (a) CO, HC and (b) NO_x, soot (injection timing, °CA ATDC).

conducting a full-engine-cycle CFD simulation, and found the injection timing has an important influence on the emissions of the engine. In order to reduce the emissions, the injection timing should be controlled within a limited range. Thus the effects of injection timing on the mixture preparation process for the diesel PCCI engine using the KIVA-3V with the new spray/wall interaction model are further discussed in this study.

Figure 29 shows the equivalence ratio, diesel vapor, and liquid distributions at the time of 5° CA after different injection timings from –60 to –30° CA ATDC. It can be seen from Fig. 29 that the fuel unavoidably impinges the wall for all the injection timings. For different injection timings, the impingement distance between the nozzle and the impingement site is obviously different. A large amount of fuel impinges on the cylinder wall for the case with the injection timing of –60° CA ATDC, which will lead to the problem of lubricating oil dilution. For the case with –50° CA ATDC injection timing, much fuel impinges on the piston surface. With further retarding the injection

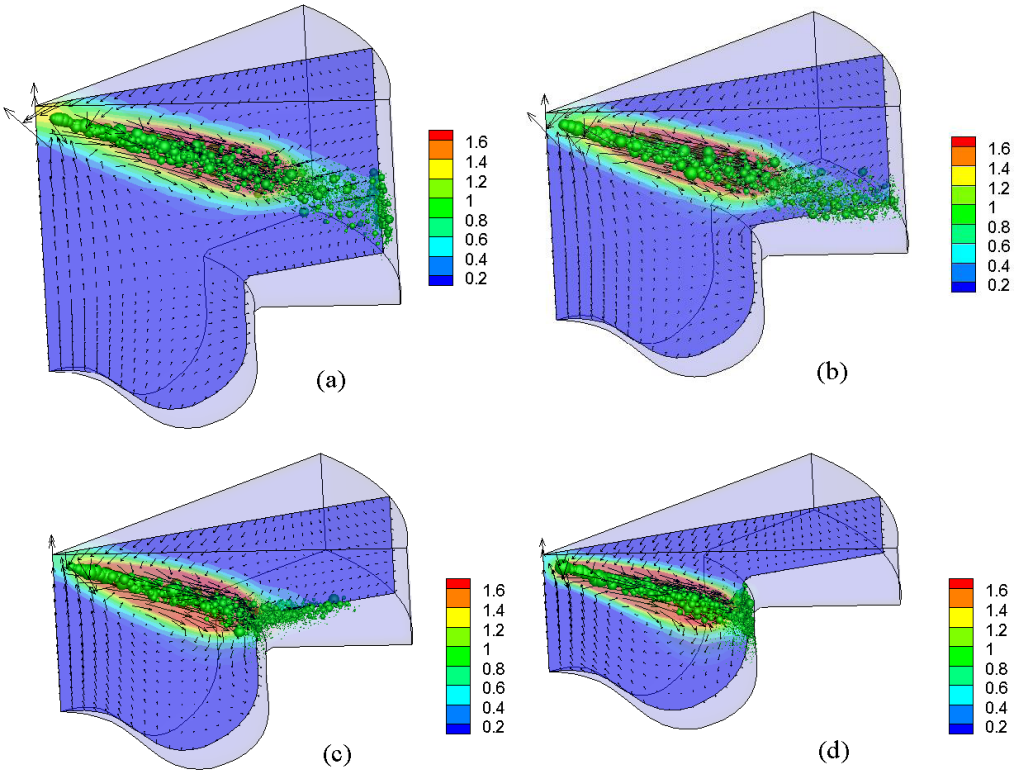

FIG. 29: Equivalence ratio, diesel vapor, and liquid distributions at the time of 5° CA after start of injection timing for (a) SOI = –60° CA ATDC, (b) SOI = –50° CA ATDC, (c) SOI = –40° CA ATDC, and (d) SOI = –30° CA ATD.

timing closing to TDC, the fuel impinges on the inner part of the bowl surface, leading to a tumble motion of the gas in the piston bowl. The equivalence ratio, diesel vapor, and liquid distributions at –20° CA ATDC for different injection timings are illustrated in Fig. 30. It can be clearly observed that the mixture of the fuel/air becomes leaner compared to those shown in Fig. 29 due to the motion of the in-cylinder air/fuel mixture. And there is a region where the fuel/air mixture is rich near the impingement site for all the cases, which can be partially explained by the evaporation of the secondary droplets with small sizes produced by the spray/wall interaction. It has been widely recognized that the wall film formed by the impinged droplets with relatively large sizes is the major source of unburned hydrocarbon, carbon monoxide, and particulate matter emissions (Koci et al., 2009; Dec, 2009). This further confirms the importance of the spray/wall interaction for the diesel PCCI combustion with early-injection timing.

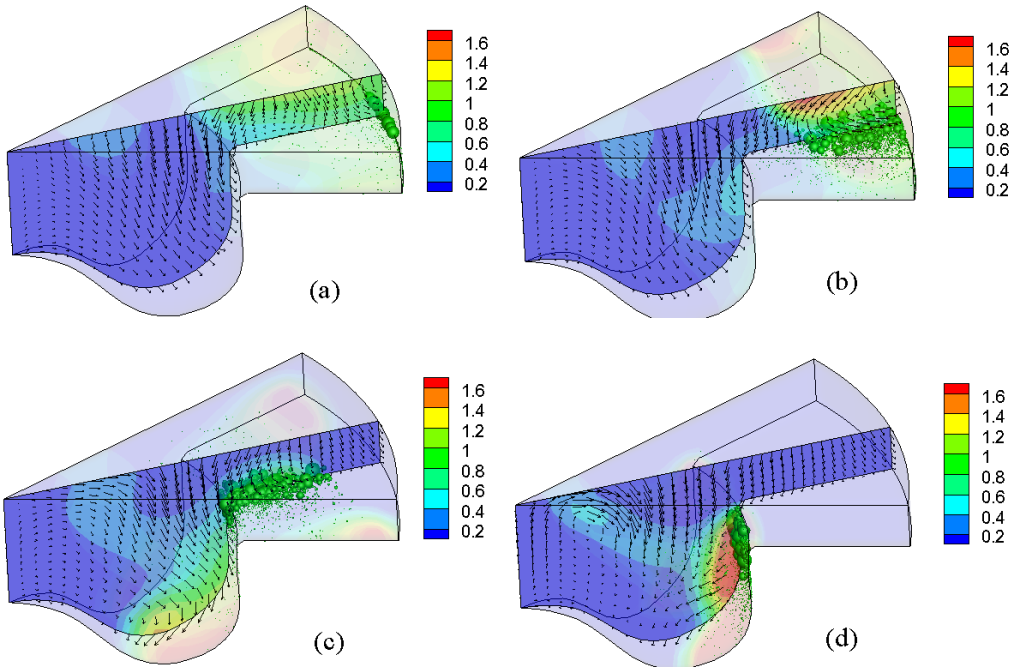

FIG. 30: Fuel equivalence ratio, diesel vapor, and liquid distributions at –20°CA ATDC for (a) SOI = –60° CA ATDC, (b) SOI = –50° CA ATDC, (c) SOI = –40° CA ATDC, and (d) SOI = –30° CA ATDC.

5. CONCLUSIONS

A new spray/wall interaction model was developed in this study based on the experimental results in the literature with special emphasis on the PCCI-engine relevant conditions, i.e., high injection pressure and intermediate-to-high backpressure. Extensive validations of the new spray/wall interaction model were performed by comparing with the experimental data found in the literature and the results predicted by the OA model. The validation data cover the penetrations of the impinged spray, including the radius and height of the impinged spray, and the local parameters of the impinged spray, including the velocity and size distributions of the secondary droplets. The results indicate that the new model shows better agreement with the experimental results than the OA model, especially for cases with high injection pressure, which is the typical engine-relevant condition. Thus the new spray/wall interaction model is more suitable than the OA model for predicting the outcomes of the impinged spray under PCCI engines with early in-cylinder injection.

Furthermore, the KIVA-3V code using the new spray/wall interaction model was applied to investigate the effects of injection timing on the combustion and emission characteristics of a diesel PCCI engine. It is found that the combustion and emissions

of the PCCI engine can be reasonably predicted by the computational model with the new spray/wall interaction model. The predictions indicate that injection timing plays an important role in the fuel/air mixing process, and a large amount of fuel deposits on the piston surface, forming the wall film due to the spray impingement onto the piston. Therefore both the spray/wall interaction and the dynamics of the wall film formed by spray impingement significantly affect the combustion and emission characteristics of PCCI engines. Further investigation of the wall film model will be conducted in our next work.

ACKNOWLEDGMENTS

This work is supported by the National Natural Science Foundation of China (Grant No. 51176020) and the National Basic Research Project of China (Grant No. 2013CB228400).

REFERENCES

Allen, R. F., The mechanics of splashing, *J. Coll. Interface Sci.*, vol. **124**, no. 1, pp. 309–316, 1988.

Allocca, L., Andreassi, L., and Ubertini, S., Evaluation of splash models with high-pressure diesel spray, SAE Paper no. 2006-01-1117, 2006.

Amsden, A., A block-structured KIVA program for engines with vertical or canted values, Los Alamos National Laboratory, Technical Report no. LA-13313-MS, 1997.

Andreassi, L., Ubertini, S., and Allocca, L., Experimental and numerical analysis of high pressure diesel spray–Wall interaction, *Int. J. Multiphase Flow*, vol. **33**, no. 7, pp. 742–765, 2007.

Arcoumanis, C. and Chang, J.-C., Flow and heat transfer characteristics of impinging transient diesel sprays, SAE Paper no. 940678, 1994.

Bai, C. and Gosman, A., Development of methodology for spray impingement simulation, SAE Paper no. 950283, 1995.

Bai, C. X., Rusche, H., and Gosman, A. D., Modelling of gasoline spray impingement, *Atomization Sprays*, vol. **12**, no. 1-3, pp. 1–27, 2002.

Cossali, G., Coghe, A., and Marengo, M., The impact of a single drop on a wetted solid surface, *Exp. Fluids*, vol. **22**, no. 6, pp. 463–472, 1997.

Dec, J. E., Advanced compression-ignition engines—Understanding the in-cylinder processes, *Proc. Combust. Inst.*, vol. **32**, no. 2, pp. 2727–2742, 2009.

Diwakar, R. and Singh, S., Importance of spray-bowl interaction in a DI diesel engine operating under PCCI combustion mode, SAE Paper no. 2009-01-0711, 2009.

Drake, M. C., Fansler, T. D., Solomon, A. S., and Szekely, G., Piston fuel films as a source of smoke and hydrocarbon emissions from a wall-controlled spark-ignited direct-injection engine, SAE Paper no. 2003-01-0547, 2003.

Fang, T., Coverdill, R., Lee, C., and White, R., Smokeless combustion within a small-bore HSDI diesel engine using a narrow angle injector, SAE Paper no. 2007-01-0203, 2007.

Fujimoto, H., Senda, J., Nagae, M., Hashimoto, A., Saito, M., and Katsura, N., Characteristics of a diesel spray impinging on a flat wall, Symp. on Diagnostics and Modeling of Combustion, in *I.C. Engines*, Kyoto, Japan, in Proc. COMODIA 90 Int., pp. 193–198, 1990.

Gahdiri, H., *Raindrop Impact, Soil Splashing and Catering*, PhD Thesis, University of Reading, England, UK, 1978.

Han, Z. and Reitz, R. D., Turbulence modeling of internal combustion engines using RNG $\kappa - \varepsilon$ models, *Combust. Sci. Technol.*, vol. **106**, no. 4-6, pp. 267–295, 1995.

Han, Z. and Reitz, R. D., A temperature wall function formulation for variable-density turbulent flows with application to engine convective heat transfer modeling, *Int. J. Heat Mass Transfer*, vol. **40**, no. 3, pp. 613–625, 1997.

Han, Z., Xu, Z., and Trigui, N., Spray/wall interaction models for multidimensional engine simulation, *Int. J. Engine Res.*, vol. **1**, no. 1, pp. 127–146, 2000.

Hiroyasu, H. and Kadota, T., Fuel droplet size distribution in diesel combustion chamber, SAE Paper no. 740715, 1974.

Jayaratne, O. and Mason, B., The coalescence and bouncing of water drops at an air/water interface, *Proc. R. Soc. London, Ser. A*, vol. **280**, no. 1383, pp. 545–565, 1964.

Jia, M., Peng, Z., and Xie, M., Evaluation of breakup models and application to the mixture preparation process for diesel HCCI engines, SAE Paper no. 2008-01-0023, 2008a.

Jia, M., Peng, Z., Xie, M., and Stobart, R., Evaluation of spray/wall interaction models under the conditions related to diesel HCCI engines, SAE Paper no. 2008-01-1632, 2008b.

Jia, M., Peng, Z., and Xie, M., Numerical investigation of soot reduction potentials with diesel homogeneous charge compression ignition combustion by an improved phenomenological soot model, *Proc. Inst. Mech. Eng., Part D (J. Automob. Eng.)*, vol. **223**, no. 3, pp. 395–412, 2009.

Jia, M., Xie, M., Wang, T., and Peng, Z., The effect of injection timing and intake valve close timing on performance and emissions of diesel PCCI engine with a full engine cycle CFD simulation, *Appl. Energy*, vol. **88**, no. 9, pp. 2967–2975, 2011.

Katsura, N., Saito, M., Senda, J., and Fujimoto, H., Characteristics of a diesel spray impinging on a flat wall, SAE Paper no. 890264, 1989.

Koci, C., Ra, Y., Krieger, R., and Andrie, M., Detailed unburned hydrocarbon investigations in a highly-dilute diesel low temperature combustion regime, SAE Paper no. 2009-01-0928, 2009.

Kokjohn, S., Hanson, R., Splitter, D., and Reitz, R., Fuel reactivity controlled compression ignition (RCCI): A pathway to controlled high-efficiency clean combustion, *Int. J. Engine Res.*, vol. **12**, no. 3, pp. 209–226, 2011.

Kong, S.-C., Drop/wall interaction criteria and their applications in diesel spray modeling, *Atomization Sprays*, vol. **17**, no. 6, pp. 473–499, 2007.

Kong, S., Ra, Y., and Reitz, R., Performance of multi-dimensional models for simulating diesel premixed charge compression ignition engine combustion using low- and high-pressure injectors, *Int. J. Eng. Res.*, vol. **6**, no. 5, pp. 475–486, 2005.

Lee, S.-S., Investigation of two low emissions strategies for diesel engines: Premixed charge

compression ignition (PCCI) and stoichiometric combustion, PhD Thesis, University of Wisconsin-Madison, 2007.

Lee, S. H. and Ryou, H. S., Development of a new spray/wall interaction model, *Int. J. Multiphase Flow*, vol. **26**, no. 7, pp. 1209–1234, 2000.

Lee, S. and Reitz, R., Spray targeting to minimize soot and CO formation in premixed charge compression ignition (PCCI) combustion with a HSDI diesel engine, SAE Paper no. 2006-01-0918, 2006.

Levin, Z. and Hobbs, P. V., Splashing of water drops on solid and wetted surfaces: Hydrodynamics and charge separation, *Philos. Trans. R. Soc. London, Ser. A*, vol. **269**, no. 1200, pp. 555–585, 1971.

Lindgren, R. and Denbratt, I., Influence of wall properties on the characteristics of a gasoline spray after wall impingement, SAE Paper no. 2004-01-1951, 2004.

Liu, Y.-D., Jia, M., Xie, M.-Z., and Pang, B., Enhancement on a skeletal kinetic model for primary reference fuel oxidation by using a semidecoupling methodology, *Energy Fuels*, vol. **26**, no. 12, pp. 7069–7083, 2012.

Mohammadi, A., Kidoguchi, Y., and Miwa, K., Effect of injection parameters and wall-impingement on atomization and gas entrainment processes in diesel sprays, SAE Paper no. 2002-01-0497, 2002.

Moreira, A. L. N., Moita, A. S., and Panão, M. R., Advances and challenges in explaining fuel spray impingement: How much of single droplet impact research is useful?, *Prog. Energy Combust. Sci.*, vol. **36**, no. 5, pp. 554–580, 2010.

Mundo, C., Sommerfeld, M., and Tropea, C., Droplet-wall collisions: Experimental studies of the deformation and breakup process, *Int. J. Multiphase Flow*, vol. **21**, no. 2, pp. 151–173, 1995.

Naber, J. and Reitz, R., Modeling engine spray/wall impingement, SAE Paper no. 880107, 1988.

Nordin, N., Complex Chemistry Modeling of Diesel Spray Combustion, PhD Thesis, Chalmers University of Technology, Gothenburg, Sweden, 2001.

O'Rourke, P. and Amsden, A., A particle numerical model for wall film dynamics in port-injected engines, SAE Paper no. 961961, 1996.

O'Rourke, P. and Amsden, A., A spray/wall interaction submodel for the KIVA-3 wall film model, SAE Paper no. 2000-01-0271, 2000.

Okude, K., Mori, K., Shiino, S., and Moriya, T., Premixed compression ignition (PCI) combustion for simultaneous reduction of NOx and soot in diesel engine, SAE Paper no. 2004-01-1907, 2004.

Park, S. W. and Lee, C. S., Macroscopic and microscopic characteristics of a fuel spray impinged on the wall, *Exp. Fluids*, vol. **37**, no. 5, pp. 745–762, 2004.

Reitz, R. D., Modeling atomization processes in high-pressure vaporizing sprays, *Atomization and Spray Technology*, vol. **3**, pp. 309–337, 1987.

Reitz, R. and Bracco, F., Mechanisms of breakup of round liquid jets, *Encycl. Fluid Mech.*, vol. **3**, pp. 233–249, 1986.

Ricart, L. M., Reltz, R. D., and Dec, J. E., Comparisons of diesel spray liquid penetration and vapor fuel distributions with in-cylinder optical measurements, *J. Eng. Gas Turbines Power*, vol. **122**, no. 4, pp. 588–595, 2000.

Rodriguez, F. and Mesler, R., Some drops don't splash, *J. Coll. Interface Sci.*, vol. **106**, no. 2, pp. 347–352, 1985.

Roisman, I., Prunet-Foch, B. Tropea, C., and Vignes-Adler, M., Multiple drop impact onto a dry solid substrate, *J. Coll. Interface Sci.*, vol. **256**, no. 2, pp. 396–410, 2002.

Roisman, I. V., Horvat, K., and Tropea, C., Spray impact: Rim transverse instability initiating fingering and splash, and description of a secondary spray, *Phys. Fluids*, vol. **18**, p. 102104, 2006.

Samenfink, W., Elsäßer, A., Dullenkopf, K., and Wittig, S., Droplet interaction with shear-driven liquid films: Analysis of deposition and secondary droplet characteristics, *Int. J. Heat Fluid Flow*, vol. **20**, no. 5, pp. 462–469, 1999.

Sandquist, H., Lindgren, R., and Denbratt, I., Sources of hydrocarbon emissions from a direct injection stratified charge spark ignition engine, SAE Paper no. 2000-01-1906, 2000.

Senda, D. J., Iwashita, S., and Fujimoto, H., Modeling of diesel spray impingement on a flat wall, SAE Paper no. 941894, 1994.

Senda, J., Kanda, T., Al-Roub, M., Farrell, P. V., Fukami, T., and Fujimoto, H., Modeling spray impingement considering fuel film formation on the wall, SAE Paper no. 970047, 1997.

Senda, D. J., Higaki, T., Sagane, Y., and Fujimoto, H., Modeling and measurement on evaporation process of multicomponent fuels, SAE Paper no. 2000-01-0280, 2000.

Siewert, R., Spray angle and rail pressure study for low NOx diesel combustion, SAE Paper no. 2007-01-0122, 2007.

Stanton, D. and Rutland, C., Modeling fuel film formation and wall interaction in diesel engines, SAE Paper no. 960628, 1996.

Stevens, E. and Steeper, R., Piston wetting in an optical DISI engine: Fuel films, pool fires, and soot generation, SAE Paper no. 2001-01-1203, 2001.

Stow, C. and Stainer, R., The physical products of a splashing water drop, *J. Meteorol. Soc. Jpn.*, vol. **55**, pp. 518–532, 1977.

Stow, C. and Hadfield, M., An experimental investigation of fluid flow resulting from the impact of a water drop with an unyielding dry surface, *Proc. R. Soc. London, Ser. A*, vol. **373**, no. 1755, pp. 419–441, 1981.

Wachters, L. and Westerling, N., The heat transfer from a hot wall to impinging water drops in the spheroidal state, *Chem. Eng. Sci.*, vol. **21**, no. 11, pp. 1047–1056, 1966.

Wang, A.-B., Chen, C.-C., and Hwang, W.-C., On some new aspects of splashing impact of drop-liquid surface interactions, in Rein, M., Ed., *Drop-Surface Interactions*, Heidelberg: Springer, pp. 303–306, 2002.

Wu, Z.-N., Prediction of the size distribution of secondary ejected droplets by crown splashing of droplets impinging on a solid wall, *Probab. Eng. Mech.*, vol. **18**, no. 3, pp. 241–249, 2003.

Yao, M., Zheng, Z., and Liu, H., Progress and recent trends in homogeneous charge compression

ignition (HCCI) engines, *Prog. Energy Combust. Sci.*, vol. **35**, no. 5, pp. 398–437, 2009.

Yarin, A. and Weiss, D., Impact of drops on solid surfaces: Self-similar capillary waves, and splashing as a new type of kinematic discontinuity, *J. Fluid Mech.*, vol. **283**, no. 1, pp. 141–173, 1995.

Atomization and Sprays, 24 (1): 81–96 (2014)

EFFECT OF THE LIQUID INJECTION ANGLE ON THE ATOMIZATION OF LIQUID JETS IN SUBSONIC CROSSFLOWS

H. Almeida, J. M. M. Sousa, & M. Costa*

Mechanical Engineering Department, Instituto Superior Técnico, University of Lisbon, Avenida Rovisco Pais, 1049-001 Lisbon, Portugal

*Address all correspondence to M. Costa E-mail: mcosta@ist.utl.pt

Original Manuscript Submitted: 7/27/2013; Final Draft Received: 10/28/2013

This work is focused on the study of sprays produced by pressure atomizers of single-hole type when subjected to air crossflows at atmospheric pressure. The study was carried out in a wind tunnel. Prior to spray characterization, the air flow inside the wind tunnel was evaluated with the aid of laser Doppler anemometry. The sprays were first characterized using a shadowgraphy technique, which allowed for a qualitative evaluation of the overall quality of the atomization. Subsequently, the use of phase Doppler anemometry allowed performing detailed measurements of the spray droplet diameters and velocities, as a function of the injection angle, for various nondimensional atomizer distances. The main findings of this study are as follows: (i) The liquid column disintegration process is significantly affected by the liquid injection angle and, less considerably, by the liquid-to-air momentum flux ratio; (ii) the Sauter mean diameter decreases noticeably as the injection angle of the liquid increases; and (iii) the characteristics of droplet diameter and velocity distributions vary significantly as the distance to the injector increases.

KEY WORDS: *pressure atomizer, liquid spray, angled injection, air crossflow*

1. INTRODUCTION

The atomization of liquids in air crossflows is an important topic in the areas of combustion, agriculture, and the pharmaceutical industry. For example, in the case of combustion, some combustors for gas turbines use the fuel injection (gas or liquid) in a recirculation region of combustion products (e.g., Roquemore et al., 2001; Melo et al., 2009, 2011). In practical terms, this requires the fuel to be injected by pressure atomizers (in the case of liquid fuels) from the combustion chamber walls, thus forming an angle with the main flow inside. It is therefore important to study the spray characteristics produced by this type of atomizer in air crossflows. There are, however, very few studies available in the literature concerning this area of atomization, and the vast majority only considers cases where the liquid is injected at an angle of 90° with respect to the crossflow. Furthermore, the use of liquid angled injection (i.e., where the liquid is injected

1044–5110/14/$35.00

NOMENCLATURE

d	nozzle diameter	V_{liq}	liquid injection velocity
H	wind tunnel height	W	wind tunnel width
k	air turbulent kinetic energy	$\mathrm{We}_{\mathrm{rel-air}}$	relative air Weber number, $\rho_{\mathrm{air}} d \left(U_{\mathrm{air}} - u_{\mathrm{liq}}\right)^2 / \sigma$
L	breakup length		
Oh	Ohnesorge number, $\mu_{liq}/(\rho_{\mathrm{liq}} d \sigma_{\mathrm{liq}})^{1/2}$	$\mathrm{We}_{\mathrm{liq}}$	liquid Weber number, $\rho_{\mathrm{liq}} d V_{\mathrm{liq}}^2 / \sigma_{\mathrm{liq}}$
q	liquid-to-air momentum flux ratio, $\rho_{\mathrm{liq}} V_{\mathrm{liq}}^2 / \left(\rho_{\mathrm{air}} U_{\mathrm{air}}^2\right)$	x, y, z	coordinates
$\mathrm{Re}_{\mathrm{air}}$	freestream Reynolds number, $\rho_{\mathrm{air}} U_{\mathrm{air}} d / \mu_{\mathrm{air}}$	**Greek Symbols**	
$\mathrm{Re}_{\mathrm{liq}}$	liquid jet Reynolds number, $\rho_{\mathrm{liq}} V_{\mathrm{liq}} d / \mu_{\mathrm{liq}}$	α	liquid injection angle
		μ	dynamic viscosity
		ρ	density
SMD	Sauter mean diameter	σ	liquid surface tension
u	velocity in x-direction		
u_{rel}	relative air velocity, $\left(U_{\mathrm{air}} - u_{\mathrm{liq}}\right) / U_{\mathrm{air}}$	**Subscripts**	
		air	air property
U_{air}	air velocity of the crossflow	liq	jet exit liquid property
v	velocity in y-direction	p	particle/droplet

at angles smaller than 90° with respect to the gas phase crossflow) is very common in combustion, agriculture, and pharmaceutical application areas. Hence, this paper aims at extending the present knowledge in this area of liquid jets atomization.

Relevant previous related studies of round liquid jets in gaseous subsonic crossflows include those of Inamura and Nagai (1997), Wu et al. (1997, 1998), Fuller et al. (2000), Becker and Hassa (2002), Cavaliere et al. (2003), Sallam et al. (2004), Costa et al. (2006), Bellofiore et al. (2007), and Kim et al. (2010), among others. These authors have determined liquid column trajectories, column fracture locations, and near-field spray characteristics as a function of the liquid injection angle. An important conclusion was that the liquid column trajectories correlate well with the liquid injection angle, α, and liquid-to-air momentum flux ratio, q.

With the exception of Fuller et al. (2000), Costa et al. (2006), Bellofiore et al. (2007), and Kim et al. (2010), the available studies in the literature only consider the case where the liquid is injected at an angle of 90° with respect to the air crossflow. Additionally, only Costa et al. (2006) have made use of phase Doppler anemometry to carry out a

detailed characterization of the sprays as a function of the injection angle, although this study has been conducted for relatively low crossflow velocities. In this context, it is important to enhance the knowledge regarding angled injection of liquid sprays in crossflows at higher velocities.

The main objective of this work consists of the characterization of sprays produced by single-hole pressure atomizers, when subjected to subsonic air crossflows at atmospheric pressure conditions. The study was conducted in a wind tunnel, where the air flow was previously characterized with the aid of laser Doppler anemometry (LDA). Subsequently, the spray characterization was carried out using shadowgraphy and phase Doppler anemometry (PDA). Special emphasis was given to the effect of the liquid flow injection angle on the atomization characteristics.

2. EXPERIMENTAL APPARATUS AND PROCEDURE

Figure 1 shows schematically the test section, including details of the atomizer geometry, and of the diagnostics. The wind tunnel used was built in glass with the following

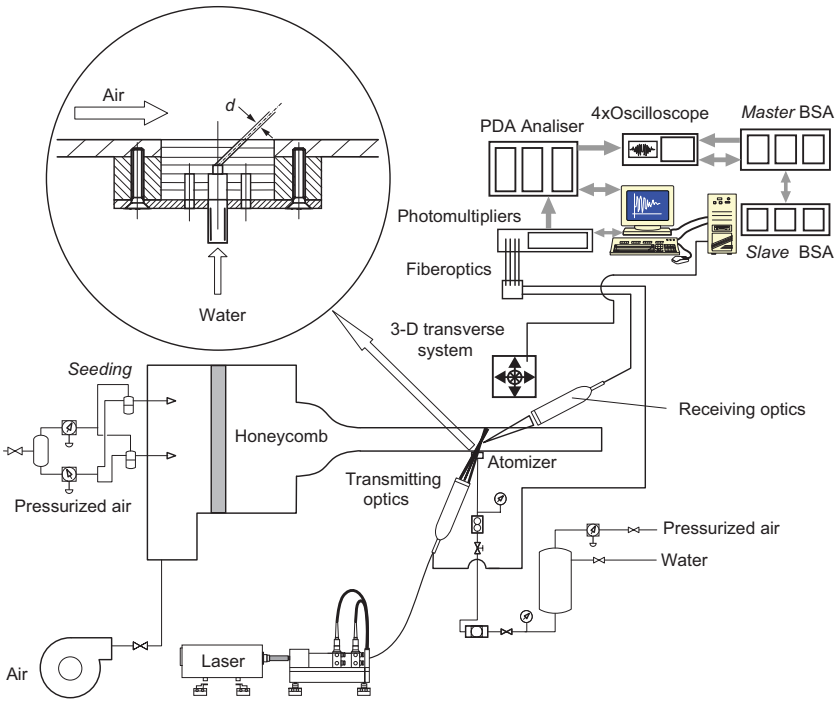

FIG. 1: Schematics of the test section, including details of the atomizer geometry, and of the diagnostics.

dimensions: length L = 0.5 m, height H = 0.075 m, and width W = 0.05 m. A honeycomb was installed in the plenum, upstream of a 24:1 contraction, in order to eliminate large-scale vortices. The contraction was designed according to the methodology proposed by Tulapurkara and Bhalla (1988) aiming to minimize both nonuniformities in the mean flow and turbulence intensity in the test section.

In this study, four single-hole pressure atomizers were used, corresponding to injection angles α of 30°, 45°, 60°, and 90°. The atomizer internal diameter, d, was constant and equal to 0.15 mm. The ratio between the length of the discharge hole and the inner diameter of the atomizer was, in all cases, larger than 100, which ensures that the liquid flow is fully developed at the discharge. For security reasons, the liquid used in the tests was distilled water, which was fed from a pressurized tank at 15 bar using nitrogen bottles. The setup allowed characterizing the sprays produced by the four atomizers as a function of the injection angle (α), the liquid injection velocity (V_{liq}), and the air crossflow velocity (U_{air}). Figure 2 shows the coordinate system used in the present study.

A commercial LDA system (Dantec, Denmark) was used to characterize the air flow in the wind tunnel, measuring the two velocity components simultaneously in dual-beam backward scattering operation mode. To generate the seeding particles, four medical nebulizers (Inspiron 002305) were used, employing a mixture of water (20%) and ethylene glycol (80%). The analog signal from the photomultipliers was band-pass filtered and processed by two burst spectrum analyzers (model Dantec 57N20/57N35), using an IEEE interface with a computer. With this configuration it was possible to collect data samples at an average acquisition rate of about 0.5 kHz. Mean velocities and their variances were computed by ensemble averaging from 10,000 samples, using the Dantec BSA Flow Software.

Initially, the characterization of the sprays involved the use of an interferometric technique called shadowgraphy. To that end, an argon-ion laser emitting at a wavelength of 515 nm with a maximum power of 500 mW was employed. The spray zone images were recorded by a high-speed digital camera, model Phantom v4.2 (Vision Research, USA), with a resolution of 512×512 pixels (monochrome sensor with sensitivity 4800

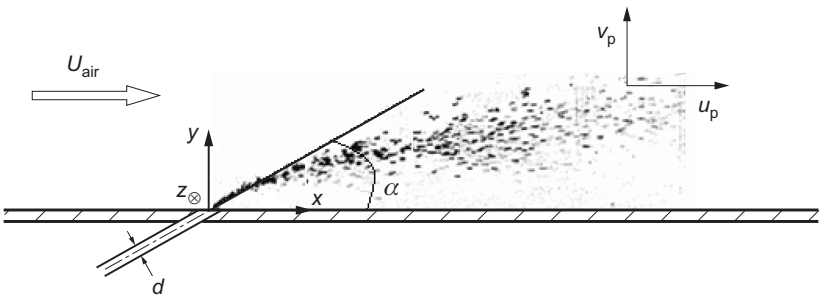

FIG. 2: Coordinate system.

ISO/ASA), using exposure times of 10 μs and average acquisition periods of about 66 μs. The lens used was a model AF Micro-Nikkor 60 mm f/2.8D (NIKON, Japan). As a result of the optical arrangement used during the experiments, the spatial resolution was limited to ∼125 μm/pixel. For the management of final digital images, built-in MATLAB routines were employed.

After the visualization, droplet diameters and velocities in the sprays were quantified by the use of PDA. Similarly to the LDA, a commercial two-component Dantec system was employed (see Fig. 1). In this case, the receiving probe was positioned at an angle with the transmitting optics not very far from Brewster's refraction angle, which corresponded to 73.7°. This allowed taking advantage of the dominance of the first order of refraction of light in the droplets and, at the same time, reducing the influence of higher-order refractions. The optical arrangement produced a measuring volume of approximately 4 mm in length and 2 mm in diameter. The optical receiver was adjusted for "medium-sized particles" (mask B) and positioned at an angle of 59°, allowing to measure droplet diameters up to nearly 400 μm. The analog signals from the photomultipliers produced by the scattered light were processed by a module interface, model Dantec P80.

The determination of the statistical distribution of the droplet diameters and velocities was made using, again, the Dantec BSA Flow Software. In the process of validating the signal, the signal-to-noise ratio and deviations from sphericity were taken into account. The sphericity criterion was always set to 15%. The number of samples in the measurements was generally larger than 5000, though in areas characterized by high acquisition rates this number has reached 10,000. Based on the analysis of these sources of error it is estimated that the overall uncertainty in the measurement of mean velocities is below 2%. In the case of droplet diameters, the overall uncertainty is estimated to be approximately 5%.

3. RESULTS AND DISCUSSION

Table 1 summarizes the operating conditions employed in the present study.

Figure 3 shows the mean velocity and turbulent kinetic energy profiles in the wind tunnel, measured at the section where the discharge hole of the atomizer was located. The profiles were normalized using the potential flow velocity, U_{air}, as a velocity scale, and using the height, H, and the width, W, of the tunnel as length scales. Since measurements of the third velocity component were not performed, the turbulent kinetic energy was calculated via estimation of the third velocity variance as the semi-sum of its counterparts, which is a good approximation in boundary layer flows (Spalart, 1988).

Figure 3(a) shows a typical behavior of a boundary layer flow, displaying high velocity gradients in the near-wall region. It was found that the boundary layer thickness varied little with the operating conditions of the wind tunnel, remaining always close

TABLE 1: Operating conditions. For all test conditions: d = 0.15 mm, Oh = 0.0084, V_{liq} = 8.2 m/s, $\mathrm{Re}_{\mathrm{liq}}$ = 1424, $\mathrm{We}_{\mathrm{liq}}$ = 144, U_{air} = 116.7 m/s, $\mathrm{Re}_{\mathrm{air}}$ = 1064.

Test condition	α (deg)	$\mathrm{We}_{\mathrm{rel-air}}$	u_{rel}	q
1	30	29	0.94	4.37
2	45	30	0.95	4.37
3	60	31	0.96	4.37
4	90	33	1.00	4.37

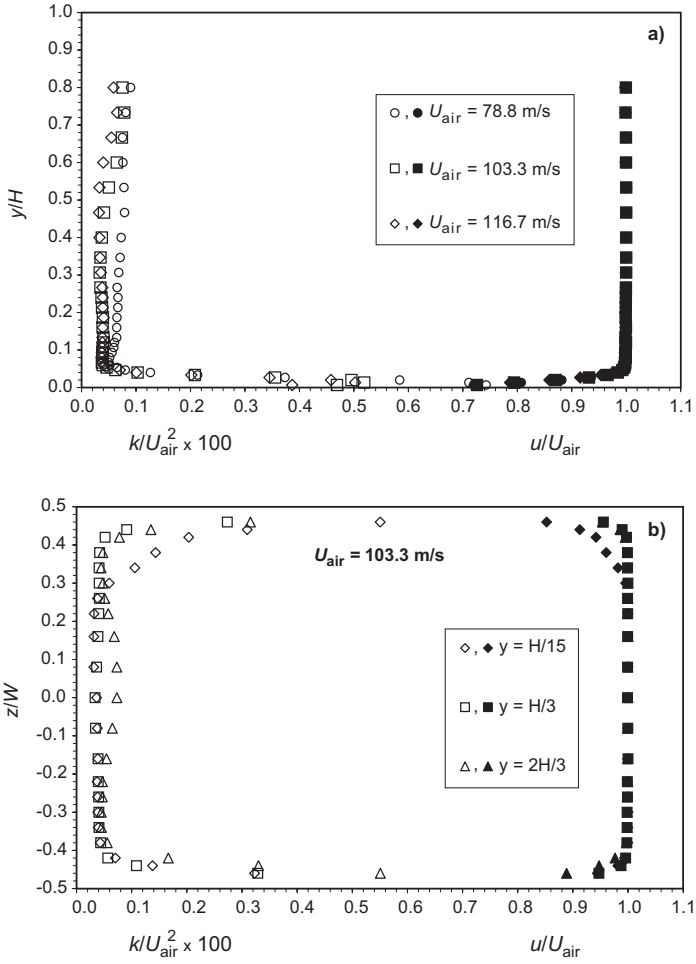

FIG. 3: Mean velocity (filled symbols) and turbulent kinetic energy (open symbols) profiles in the wind tunnel: (a) vertical profiles; (b) transverse profiles.

to 4 mm. The same can be said about the displacement thickness (approximately between 0.36 and 0.40 mm) and momentum thickness (approximately between 0.29 and 0.33 mm), resulting in a nearly constant value of the shape factor, close to 1.2.

The homogeneity of the velocity profiles outside the boundary layer can also be observed, showing that the purpose for which the contraction was projected was achieved. Also, the turbulent kinetic energy exhibit a maximum near the wall, which is associated to the high gradients of the mean velocity, but declined significantly to approximately constant values outside the boundary layer. The turbulence intensity exhibited a nearly negligible dependence of the operating conditions, settling at around 2%. The three-dimensional character of the air flow in the wind tunnel can be judged from the measured transverse profiles, shown in Fig. 3(b) for different distances to the wall (wind tunnel floor). Although the flow in a tunnel of rectangular section will inevitably show some three-dimensional characteristics, these effects are mainly noted at the corners, presumably due to the establishment of Prandtl's secondary flow of the second kind. It appears that the observed gradients of mean velocity and turbulent kinetic energy that occur in the central plane of the tunnel (where the liquid is injected) are very small and, therefore, its influence in the process of atomization is expected to be negligible.

Figure 4 shows instantaneous spray images that reveal the effect of the liquid injection angle on the atomization process. It can be seen that the spray angle increases with the liquid injection angle, α: the larger the injection angle, the greater the droplets' dispersion. This is a consequence of the fact that as the injection angle decreases, the relative velocity, u_{rel}, also decreases; specifically, when α decreases from 90° to 30°, u_{rel} decreases from 1 to 0.94, as shown in Table 1. Consequently, by decreasing the angle α, but maintaining constant the value of q, a reduction of the aerodynamic forces acting on the exposed area of the liquid column is achieved. As shown in Fig. 4, the disintegration process becomes less effective as α decreases. These spray images show a behavior somewhat similar to that described by Fuller et al. (2000), concerning the variation in the quality of the sprays as a function of the liquid injection angle.

Figures 5–8 show normalized velocities and droplet size along the y-direction for test conditions 1, 2, 3, and 4 at x/d = 50, 100, 200, 400, and 800, respectively. The droplet size is here represented by the Sauter mean diameter (SMD), which is the diameter of a droplet whose surface-to-volume ratio is equal to that of the entire spray. A comparison between the evolutions presented in these figures allows assessing the influence of the liquid injection angle in velocities and droplet size. It appears that as α increases, the values of SMD decrease significantly. Again, this behavior may be attributed to the higher u_{rel} values associated to the larger liquid injection angles, hence to the growing aerodynamic forces acting on the liquid surface.

An important observation that emerges from the comparison of these experimental results with those obtained by Costa et al. (2006) is that the experimental conditions used here originated sprays with SMD always below 150 μm (the size of the injector hole),

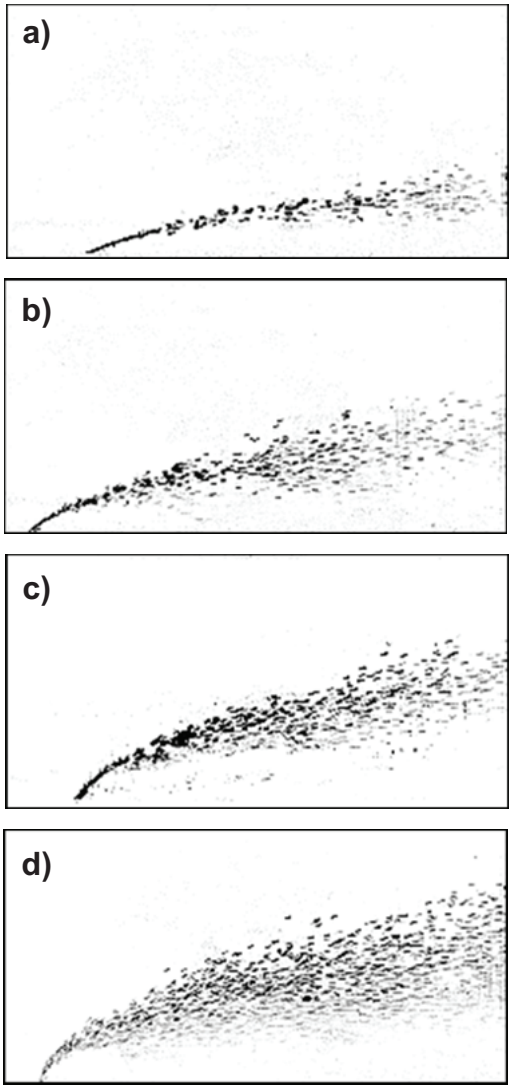

FIG. 4: Instantaneous spray images showing the effect of the liquid injection angle on the atomization process: (a) test condition 1; (b) test condition 2; (c) test condition 3; (d) test condition 4.

while in Costa et al. (2006), the SMD fluctuated between 150 and 350 μm, as a result of the lower crossflow velocities used by these authors.

Figure 9 shows normalized velocities and SMD along the spray centerline (location detected by the maximum mass flux indicated by the PDA) for test conditions 1, 2, 3, and 4. It is observed that the atomization process ends approximately at x/d = 1000 for

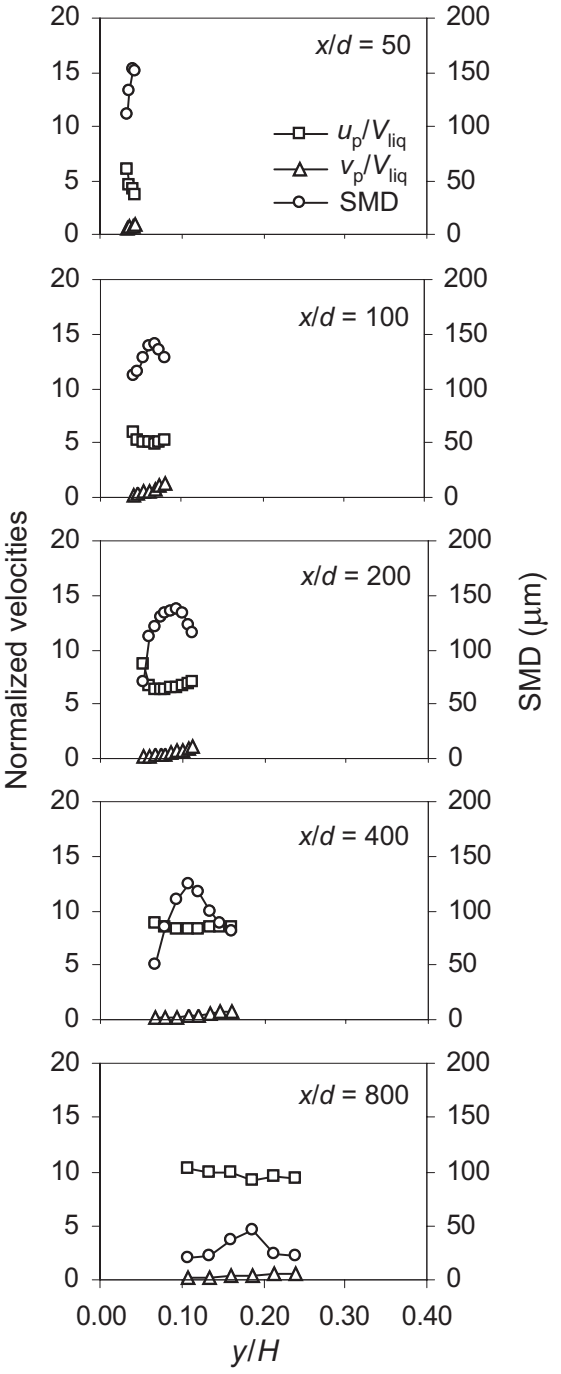

FIG. 5: Normalized velocities and droplet size along the y-direction for test condition 1 (α = 30°) at x/d = 50, 100, 200, 400, and 800.

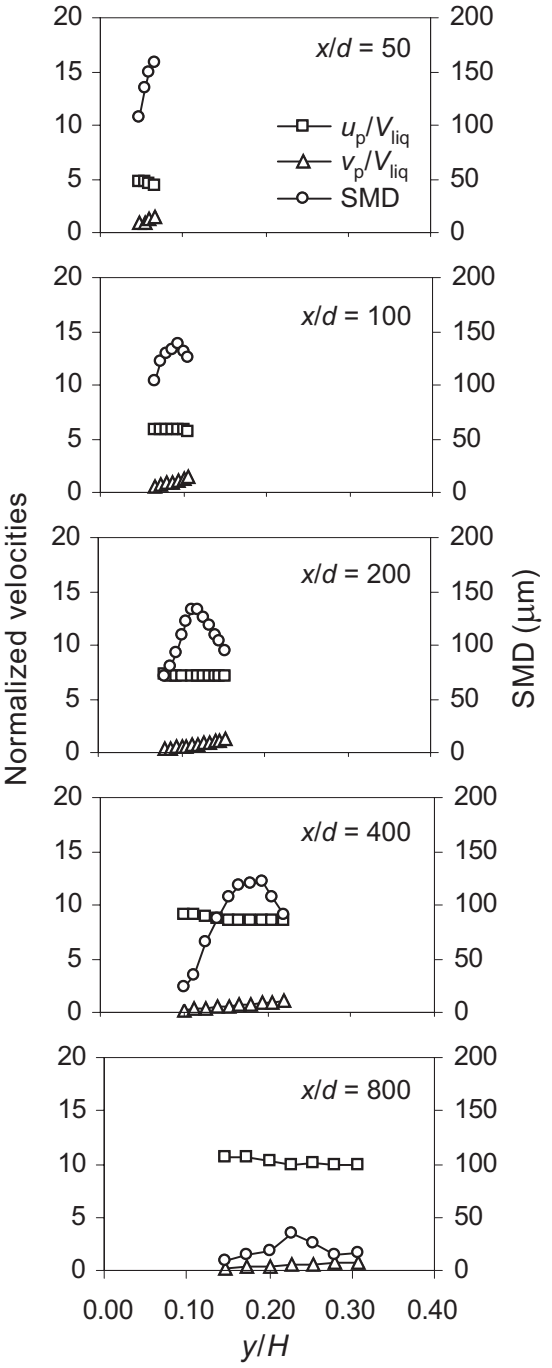

FIG. 6: Normalized velocities and droplet size along the y-direction for test condition 2 (α = 45°) at x/d = 50, 100, 200, 400, and 800.

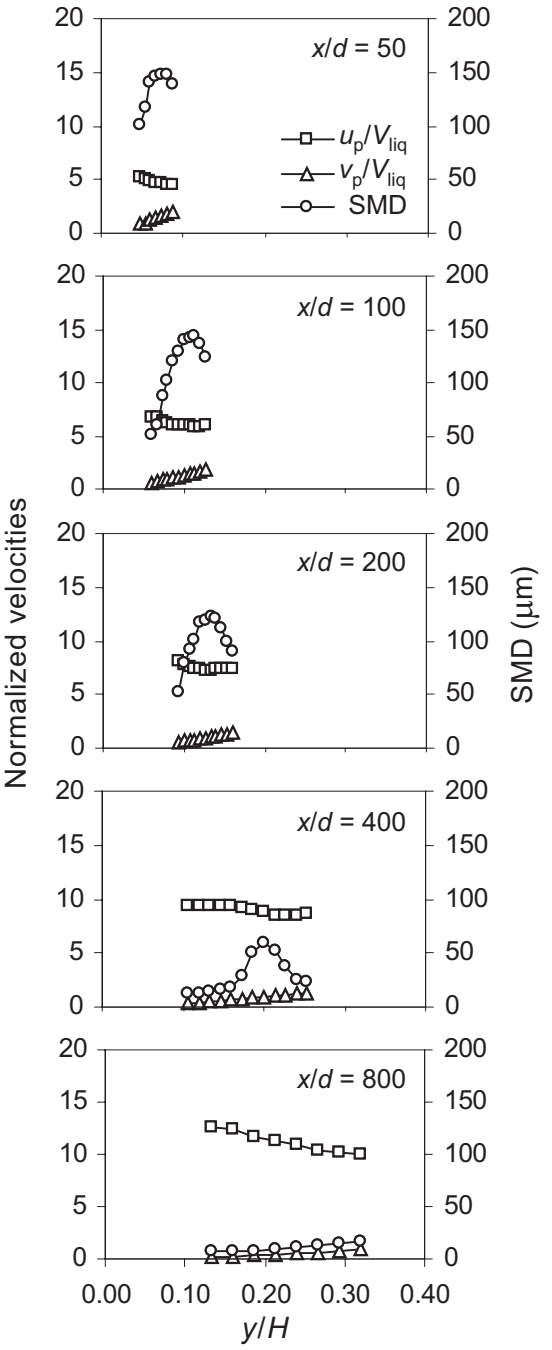

FIG. 7: Normalized velocities and droplet size along the y-direction for test condition 3 (α = 60°) at x/d = 50, 100, 200, 400, and 800.

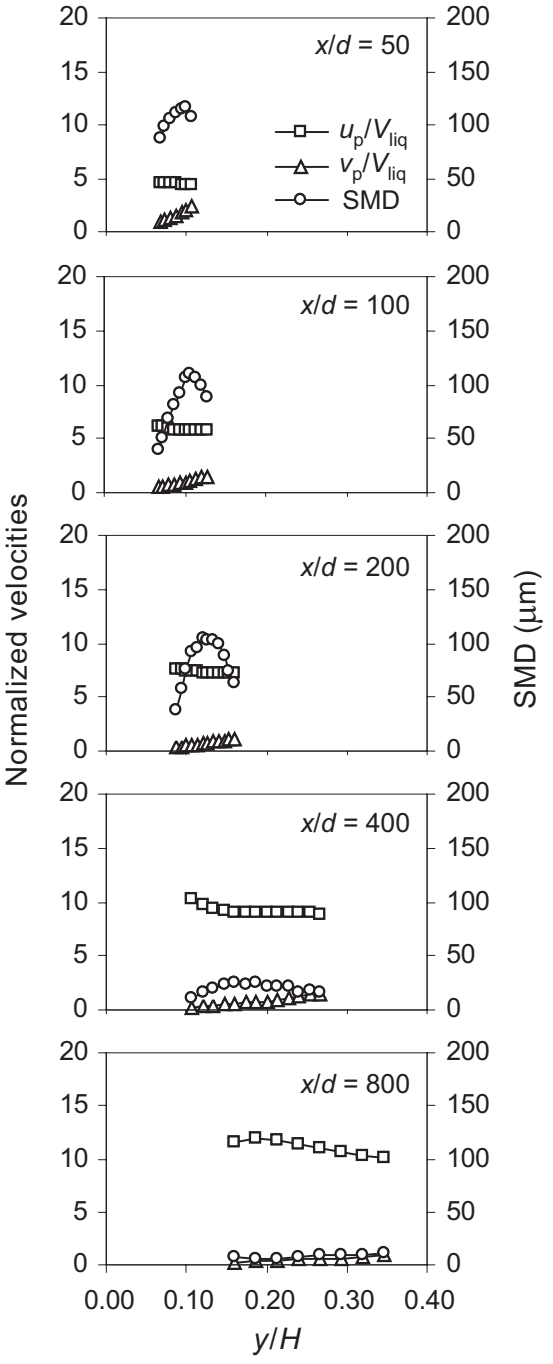

FIG. 8: Normalized velocities and droplet size along the *y*-direction for test condition 4 (α = 90°) at x/d = 50, 100, 200, 400, and 800.

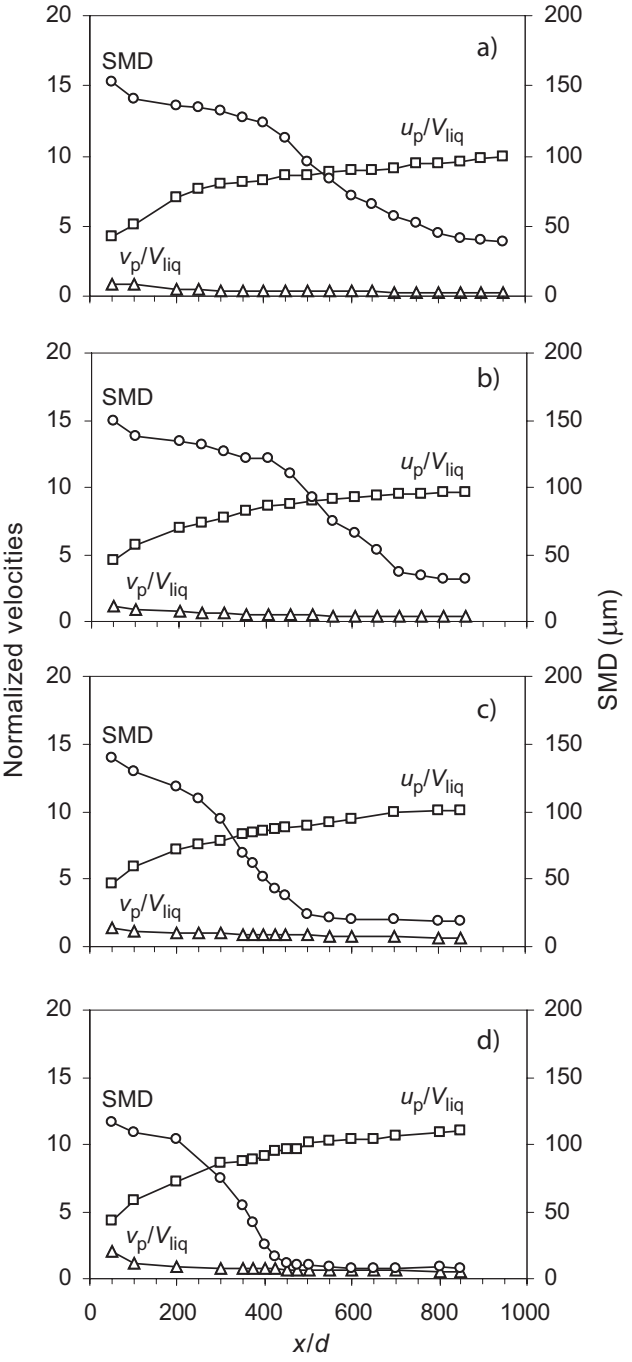

FIG. 9: Normalized velocities and droplet size along the spray centerline: (a) test condition 1; (b) test condition 2; (c) test condition 3; (d) test condition 4.

test condition 1, at x/d = 800 for test condition 2, at x/d = 550 for test condition 3, and at x/d = 450 for test condition 4. On the other hand, droplet velocities seem to be rather unaffected by the variation of the conditions. The normalized y-velocities always stabilize very fast at negligible values, whereas normalized x-velocities take a distance larger than x/d = 800 to approach a nearly constant value close to 10.

Figure 10 shows droplet velocity and droplet size distributions in various spray locations for test condition 2. The figure reveals that there is a significant difference between the droplet distributions obtained in the top regions of the spray for x/d = 50 and those obtained in other locations, both vertical and longitudinal. Corresponding distributions exhibit two distinct populations: the first (dominant), characterized by mean velocities lower than 40 m/s, that is associated to the ligaments and large droplets occurring in these dense spray regions; and the second, characterized by mean velocities close to 60 m/s, associated to small droplets formed at the initial stages of the disintegration of the liquid jet (surface breakup), that are more easily accelerated by the air crossflow. Such characteristic is almost imperceptible at x/d = 100 and further downstream, where the velocity distributions exhibit an essentially symmetrical character and the corresponding mean

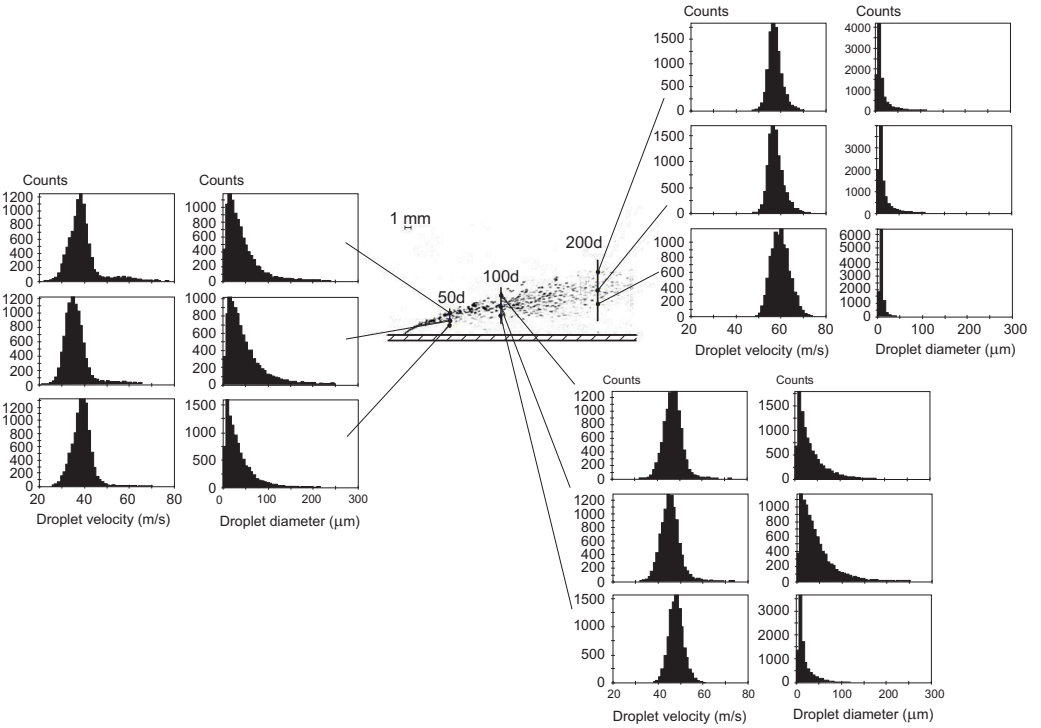

FIG. 10: Droplet velocity and size distributions in various spray locations for test condition 2.

velocities approach the air flow velocity. In regard to the droplet diameters, a significant change in the character of these distributions occurs at x/d = 100. At this station, more uniform droplet size distributions begin to emerge (at the bottom of the spray), showing a significant reduction in the amount of large droplets, which dominated the spray at upstream locations. However, it must be noted that although the counting of the latter droplets may not be very high, their contribution by mass or volume is probably dominant, as a result of the cubic dependence with the droplet diameter, which translates into the large values of SMD already presented in Figs. 5–8. As expected, the above described characteristic becomes stronger with increasing distance from the injector, as a result of the natural evolution of the atomization process.

4. SUMMARY AND CONCLUSIONS

The main findings of this study are as follows:

(1) The disintegration process of the liquid columns is significantly affected by the liquid injection angle and, to a lesser extent, by the liquid-to-air momentum flux ratio. As the liquid injection angle was decreased, the atomization process degraded as a result of a reduction in the aerodynamic forces acting on the exposed surface of the liquid column. A similar effect was obtained by increasing the liquid-to-air momentum flux ratio.

(2) The values of the SMD decreased significantly with the increase of the liquid injection angle as a consequence of the resulting higher values of the relative velocity of the air and, therefore, due to the fact that the aerodynamic forces acting on the liquid surface of the jet increase with the injection angle.

(3) There is a significant difference between the droplet velocity distributions observed in the top regions of the spray for x/d = 50 and those obtained in other locations, both vertical and longitudinal. In the former, the corresponding distributions exhibit two distinct populations: the first, characterized by mean velocities lower than 40 m/s, that is associated to the ligaments and large droplets occurring in these dense spray regions; and the second, characterized by mean velocities close to 60 m/s, associated to small droplets formed at the initial stages of the disintegration of the liquid jet, that are more easily accelerated by the air crossflow.

(4) A significant change in the character of the droplet diameter distributions was observed at x/d = 100. At this station, more uniform droplet size distributions begin to emerge, showing a significant reduction in the amount of large droplets, which dominated the spray at upstream locations. This characteristic becomes stronger with increasing distance from the injector, as a result of the natural evolution of the atomization process.

REFERENCES

Becker, J. and Hassa, C., Breakup and atomization of a kerosene jet in crossflow at elevated pressure, *Atomization Sprays*, vol. **11**, pp. 49–67, 2002.

Bellofiore, A., Cavaliere, A., and Ragucci, R., Air density effect on the atomization of liquid jets in crossflow, *Combust. Sci. Technol.*, vol. **179**, pp. 319–342, 2007.

Cavaliere, A., Ragucci, R., and Noviello, C., Bending and break-up of a liquid jet in a high pressure airflow, *Exp. Therm. Fluid Sci.*, vol. **27**, pp. 449–454, 2003.

Costa, M., Melo, M. J., Sousa, J. M. M., and Levy, Y., Spray characteristics of angled liquid injection into subsonic crossflows, *AIAA J.*, vol. **44**, pp. 646–653, 2006.

Fuller, R. P., Wu, P. K., Kirkendall, K. A., and Nejad, A. S., Effects of injection angle on atomization of liquids jets in transverse airflow, *AIAA J.*, vol. **38**, pp. 64–72, 2000.

Inamura, T. and Nagai, N., Spray characteristics of liquid jet traversing subsonic airstreams, *J. Propul. Power*, vol. **13**, pp. 250–256, 1997.

Kim, M., Song, J., Hwang, J., and Yoon, Y., Effects of canted injection angles on the spray characteristics of liquid jets in subsonic crossflows, *Atomization Sprays*, vol. **20**, pp. 749–762, 2010.

Melo, M. J., Sousa, J. M. M., Costa, M., and Levy, Y., Experimental investigation of a novel combustor model for gas turbines, *J. Propul. Power*, vol. **25**, pp. 609–617, 2009.

Melo, M. J., Sousa, J. M. M., Costa, M., and Levy, Y., Flow and combustion characteristics of a low NO_x combustor model for gas turbines, *J. Propul. Power*, vol. **27**, pp. 1212–1217, 2011.

Roquemore, W. M., Shouse, D., Burrus, D., Johnson, A., Cooper, C., Duncan, B., Hsu, K. Y., Katta, V. R., Sturgess, G. J., and Vihinen, I., Trapped vortex combustor concept for gas turbine engines, *AIAA Paper* 2001-0483, 2001.

Sallam, K. A., Aalburg, C., and Faeth, G. M., Breakup of round nonturbulent liquid jets in gaseous crossflow, *AIAA J.*, vol. **42**, pp. 2529–2540, 2004.

Spalart, P. R., Direct simulation of a turbulent boundary layer up to R_θ = 1410, *J. Fluid Mech.*, vol. **187**, pp. 61–98, 1988.

Tulapurkara, E. G. and Bhalla, V. V. K., Experimental investigation of Morel's method for wind tunnel contractions, *ASME J. Fluids Eng.*, vol. **110**, pp. 45–47, 1988.

Wu, P. K., Kirkendall, K. A., Fuller, R. P., and Nejad, A. S., Breakup processes of liquid jets in subsonic crossflows, *J. Propul. Power*, vol. **13**, pp. 64–73, 1997.

Wu, P. K., Kirkendall, K. A., Fuller, R. P., and Nejad, A. S., Spray structures of liquid jets atomized in subsonic crossflows, *J. Propul. Power*, vol. **14**, pp. 173–181, 1998.

Begell Engineering Research Collection

Over 20 journals, 10 reference works and a new Begell eBook collection provide the latest research, solutions and archives for many engineering disciplines

The Begell Engineering Research Collection is part of the Begell Digital Library (BDL), a growing collection of online content that provides the latest advancements in engineering and biomedical sciences. Distinguished international editorial boards and translated content for many titles provide a global perception of subjects. With its deep roots in thermal and fluid sciences, Begell House offers one of the most innovative, specialized engineering collections available today.

ENGINEERING RESEARCH COLLECTION HIGHLIGHTS

— **Over 20 peer-reviewed journals** — cover atomization and sprays, multiscale computations, uncertainty quantification, composites, energetic materials and chemical propulsions, energy efficiency, clean environment, porous media, radio physics and telecommunications, aero and hydrodynamics, aerospace and other topics covering both theoretical research and applications.

— **The Heat Exchanger Design Handbook** — is the only and most complete source for the design of heat exchangers, exceeding 6,000 pages of peer-reviewed information that is updated regularly.

— **Thermopedia™** — evolving from the International Encyclopedia for Heat and Mass Transfer, this multimedia reference tool enhances teaching and independent learning. Its core content is available open access.

— **ICHMT Digital Library** — International Center for Heat and Mass Transfer: Online Conferences Proceedings

— **IHTC Digital Library** — Assembly for Heat Transfer Conference: Online Conferences Proceedings

— **Begell eBook Collection** — eBooks comprise three collections: Thermal & Fluid Physics and Engineering Collection; Begell eBooks Collection and Begell eBooks Classical Archive Collection

LIBRARY BENEFITS

— Complimentary access to available journal backfiles while subscribing

— Perpetual access and archiving through PORTICO

— COUNTER compliant usage statistics

— Links to full text through CrossRef

— Easy access via Google Scholar

— SERU participant

AFFORDABLE OPTIONS

— Significant discounts are available to the full Engineering Collection.

— Smaller, specialized engineering collections are also available in:

- *Aerospace*
- *Chemistry & Chemical Engineering*
- *Energy & Environment*
- *Industry Research*
- *Mechanical Engineering*
- *Nuclear & Power Engineering*

— Special rates are available to buy the complete journal archives with one-time, discretionary budget money.

Call today for pricing or to set up a 30-day free trial.

ONLY RESOURCE OF ITS KIND!

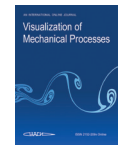

begell

50 Cross Highway
Redding, CT 06896

Tel: +1 (203) 938-1300
Fax: +1 (203) 938-1304

meghan@begellhouse.com
www.dl.begellhouse.com

Begell Engineering Research Collection

Over 20 journals provide the latest research & solutions for many engineering disciplines

Journal Title	ISSN Print, Online	Archive in BDL
Atomization and Sprays™	1045-5110, 1936-2684	1991 (Volume 1)
Composites: Mechanics, Computation, Applications	2152-2057, 2152-2073	2010 (Volume 1)
Computational Thermal Sciences: An International Journal	1940-2503, 1940-2554	2009 (Volume 1)
Heat Pipe Science and Technology	2151-7975, 2151-7991	2010 (Volume 1)
Heat Transfer Research	1064-2285, 2162-6561	1997 (Volume 28)
High Temperature Material Processes: An International Journal	1940-4360	1997 (Volume 1)
Interfacial Phenomena and Heat Transfer	2169-2785, 2167-857X	2013 (Volume 1)
International Journal for Multiscale Computational Engineering	1543-1649, 1940-4352	2003 (Volume 1)
International Journal for Uncertainty Quantification	2152-5080, 2152-5099	2011 (Volume 1)
International Journal of Energetic Materials and Chemical	2150-766X, 2150-7678	1991 (Volume 1)
International Journal of Energy for a Clean Environment	2150-3621, 2150-363X	2003 (Volume 4)
International Journal of Fluid Mechanics Research	1064-2277	1995 (Volume 25)
Journal of Automation and Information Sciences	1064-2315, 2163-9337	1996 (Volume 28)
Journal of Enhanced Heat Transfer	1065-5131	1994 (Volume 1)
Journal of Flow Visualization and Image Processing	1065-3090, 1940-4336	1993 (Volume 1)
Journal of Porous Media	1091-028X, 1934-0508	1998 (Volume 1)
Journal of Radio Electronics	2165-8439	2012 (Volume 1)
Journal of Women and Minorities in Science and Engineering	1072-8325, 1940-431X	1994 (Volume 1)
Multiphase Science and Technology	0276-1459, 1943-6181	1982 (Volume 1)
Nanomechanics Science and Technology: An International Journal	1947-5748, 1947-5756	2010 (Volume 1)
Special Topics and Reviews in Porous Media	2151-4798, 2151-562X	2010 (Volume 1)
Telecommunications and Radio Engineering	0040-2508, 1943-6009	1997 (Volume 51)
TsAGI Science Journal	1948-2590, 1948-2604	2009 (Volume 40)
Visualization of Mechanical Processes	2152-209X	2011 (Volume 1)

DATABASES

Directory of Specialists

Heat Exchanger Design Handbook ONLINE — The web version of the Begell House highly regarded reference work on heat transfer and heat exchangers

The Catalog of Worldwide Nuclear Testing

THERMOPEDIA™ — Interactive gateway to resources on heat & mass transfer, fluid flow and thermodynamics

REFERENCES & PROCEEDINGS

Annual Review of Heat Transfer Online (16 Volumes)

Electrospinning of Micro- and Nano-Fibers: Fundamentals in Separations and Filtration Processes

International Centre for Heat & Mass Transfer, ICHMT Digital Library — Online Conferences Proceedings

International Heat Transfer Conference Digital Library, IHTC Digital Library

eBOOKS

— Series in Thermal & Fluid Physics & Engineering

Begell Digital Library on iPad, iPhone & Android Devices

Available for **FREE** with Institutional Subscription

ibegell | begell house digital library

begell

50 Cross Highway
Redding, CT 06896

Tel: +1 (203) 938-1300
Fax: +1 (203) 938-1304

meghan@begellhouse.com
www.dl.begellhouse.com